Dissertation
submitted to the
Combined Faculties for the Natural Sciences and for Mathematics
of the Ruperto-Carola University of Heidelberg, Germany
for the degree of
Doctor of Natural Sciences

presented by

Wei Jiang, M.Sc. (Medical Physics)
born in: Hebei, China

Oral examination: 1 February 2010

Light Microscopic Precise Measurements of Genome Structure during Tumorigenesis in Transgenic Mice

Referees: Prof. Dr. Dr. Christoph Cremer
Prof. Dr. Stefan Wölfl

Abstract

The higher order and spatial organisation of the genome is closely related to gene's transcriptional activity. With the numerous results reported in this area, little is known about the precise information of specific chromatin structure, especially the dynamic during physiological changes and tumorigenesis, in the well-preserved tissue sections. In this work, thin tissue cryosections (about 200 nm in thickness) from the mammary gland of transgenic mice were used to study the genome organisation during the tumorigenesis process. Stereological methods were used to estimate the three-dimensional genome structure from the two-dimensional nuclear profiles. It was found that the whole genome-wide chromatin condensation state varies significantly during the tumorigenesis process. The existence of the extremely large as well as the highly condensed nuclei in the mammary tumor cryosections indicates the unique situation of malignancy. The relative volume fraction of chromosome 11 in the nucleus becomes smaller in the tumorigenesis process, while the nuclear radial position of the chromosome stays the same in this process. The central position of chromosome 11 is in good agreement with the gene density related chromosome radial positioning theory. Besides, some preliminary studies regarding the nuclear position and the condensation state of the viral oncogene SV40Tag have been demonstrated. In conclusion, this work presents the first effort to investigate genome organisation during the tumorigenesis process combining fluorescent *in situ* hybridisation and tissue cryosections. The parameters of specific genome structure measured in this work are the most precise values one can get from tissue sections so far.

Zusammenfassung

Die höhere Ordnung und die räumliche Organisation des Genoms steht eng mit der Transkriptions-Aktivität des Gens in Zusammenhang. Trotz der zahlreichen Ergebnissen in diesem Bereich gibt es wenige genaue Informationen über die spezifische Chromatin-Struktur und insbesondere über die Dynamik dieser Struktur während der physiologischen Veränderungen und Tumorentstehung in gut erhaltenen Gewebeschnitten. In dieser Arbeit wurden dünne Gewebe-Kryoschnitte (ca. 200 nm Dicke) von Brustdrüsen transgener Mäuse verwendet, um die Genom-Organisation während der Tumorentstehung zu studieren. Stereologische Methoden wurden eingesetzt, um die dreidimensionale Genom-Struktur aus den zweidimensionalen nuklearen Profilen zu schätzen. Es wurde festgestellt, dass die Chromatinkondensation des gesamten Genoms erheblich während der Tumorentstehung variiert. Die Existenz der extrem großen und der stark verdichteten Kernen in den mammakarzinomalen Kryoschnitten zeigt den Status der Bösartigkeit an. Der relative Volumenanteil von Chromosom 11 im Kern wird kleiner in der Tumorentstehung, obwohl die nukleare radiale Position des Chromosoms in diesem Prozess gleich bleibt. Die zentrale Position des Chromosoms 11 ist in guter Übereinstimmung mit der Theorie zur Gendichte bezogenen chromosomalen radialen Positionierung. Außerdem wurden einige vorbereitende Studien über die nukleare Position und den Zustand der Kondensation des viralen Onkogens SV40Tag demonstriert. Diese Arbeit stellt einen ersten Beitrag dar, um die Genom-Organisation während der Tumorentstehung zu untersuchen mit einer Kombination aus Fluoreszenz in situ Hybridisierung und der Verwendung von Gewebe-Kryoschnitten. Die in dieser Arbeit gemessenen Parameter der spezifischen Genom - Struktur sind die genauesten Werte, die bisher aus Untersuchungen von Gewebeschnitten erhalten wurden.

Contents

Chapter 1. Introduction 1
  1.1. The nucleus 1
  1.2. Genome Organisation 4
    1.2.1. The Higher-order Chromatin Organisation 4
    1.2.2. The Spatial Genome Organisation 5
      Non-random Nuclear Radial Positioning - Gene-density Theory 5
      Non-random Nuclear Radial Positioning - Chromosome Size Theory 5
      Gene Activity in Relation to The Nuclear Periphery and the Nuclear Pore Complex 8
      Cancer and Genome Organisation 8

I. Methods

Chapter 2. The Mouse Model and Mouse Cell Lines 11
  2.1. The Simian Virus 40 (SV40) 11
  2.2. The Mouse Model 11
  2.3. The Mouse Cell Lines 12
Chapter 3. Cryosections 15
Chapter 4. Molecular Cytogenetic Procedures 17
  4.1. Plasmid Preparation 17
  4.2. Nick Translation 18
  4.3. Repetitive Sequences Blocking 20
  4.4. Fluorescent *in situ* Hybridisation using Fixed Cells 21
  4.5. Fluorescent *in situ* Hybridisation using Cryosections (Cryo-FISH) 23
  4.6. MAA Fixation 24
Chapter 5. Fluorescence Microscopy 27
  5.1. Epifluorescence Microscopy 27
  5.2. Image Formation, PSF and Resolution 28
  5.3. Confocal Laser Scanning Microscopy 30
  5.4. Spatially Modulated Illumination Microscopy 31
Chapter 6. Stereology Methods 35
  6.1. Introduction to Stereology Methods 35
  6.2. Fundamental Equations of Stereology 35
  6.3. Ground Rules for Sample Design 37
  6.4. Why the Fundamental Equations Work 38
  6.5. The Sequential Subtraction Method 39
Chapter 7. Statistics 41

7.1. The Mean, Median and Standard Deviation . . . 41
7.2. Student's t-test and ANOVA Test . . . 42
7.3. Kolmogorov-Smirnov Test . . . 43

II. Results and Discussion

Chapter 8. Mouse Mammary Tissue Cryosections . . . 47

Chapter 9. Nuclear Volume Measurements . . . 49
9.1. Measuring the Nuclear Radii Distributions using the Sequential Subtraction Method . . . 49
9.2. The Nuclear Volumes Vary at Different Physiological States of the Cells . . . 51
9.3. The Precision of the Measurements . . . 56

Chapter 10. The Whole Chromosome Painting Results using Cryosections . . . 59

Chapter 11. Chromosome 11 Volume Measurements . . . 61
11.1. Converting the Grey Scale Image to Binary Image . . . 61
11.2. Chromosome 11 Volume Fraction Determination and Comparison . 64
11.3. The Changes of Relative Chromosome Volume Possibly Indicate Different Transcriptional Activities . . . 69

Chapter 12. 3D Nuclear Radial Positions of Chromosome 11 . . . 71
12.1. Analysing the Chromosome Nuclear Radial Position with the Concentric Shell Model . . . 71
12.2. The Comparison of the 3D Nuclear Radial Positions of Chromosome 11 . . . 71
12.3. Chromosome 11 Radial Positions Consist with the Gene-density Theory of Chromosome Non-random Positioning . . . 73

Chapter 13. The Preliminary Co-hybridisation Experiments . . . 77

Chapter 14. SV40Tag Gene Size Measurements using SMI Microscopy . . . 81
14.1. Standard SMI Evaluation Procedures . . . 81
14.2. Using Virtual SMI Microscopy to Estimate the Gene Size . . . 82
14.3. Size Measurements using SMI Microscopy . . . 85
14.4. Size Measurements using CLSM . . . 88
14.5. The Comparison between the Theoretical Gene Size and Different Measurements . . . 92

III. Conclusion and Outlook

Cryo-FISH and Stereological Methods Ensure the High Measuring Precision 98
The Genome-wide Chromatin Condensation State Changes during Tumorigenesis . . . 99
Chromosome Volume and Nuclear Radial Position Changes are not Correlated . . . 99
The Preliminary Results Regarding the Viral Oncogene SV40Tag . . . 100
Outlook . . . 101

IV. Appendices

Appendix A. The Measured Nuclear Section Radii of the Cryosections from the "Normal" Mouse . . . 105

Appendix B. The Radius Ratio Distributions of the Three Groups of Nuclear Sections 109
Appendix C. SV40Tag Gene Vector Construction and Sequence 111
Appendix D. Beads Preparation for Calibration Purpose 113
List of Abbreviations 115
List of Figures 117
Acknowledgement 125
Bibliography 127

Chapter 1

Introduction

1.1. The nucleus

The mammalian cell nucleus is a membrane-bound organelle that contains most of the cell's genetic material (named the cell's nuclear genome). The nucleus contains distinct compartments (Figure 1.1), and the spatial and temporal arrangements of these nuclear components are closely associated with the regulation of gene expression. The major nuclear structures together with their established and proposed functions are briefly discussed here.

The nuclear envelope

A double lipid bilayer that encloses the entire eukaryotic cell nucleus and separates its contents from the cytoplasm.

Nuclear pores

Large protein complexes that inserted in the nuclear envelope. The nuclear pore complexes facilitate and regulate the exchange of materials, including RNA, ribosomes, proteins, carbohydrates, single molecules and lipids, between the nucleus and the cytoplasm [2]. The nuclear pore complex is an eightfold-symmetric ring-shaped structure at a position where the inner and outer membranes fuse, with a basket that extends into the nucleoplasm. Recent studies with budding yeast have shown that the regions associated with nuclear pores have the gene-activating character [3].

The nuclear lamina

A meshwork of intermediate filaments on the internal face of the nuclear envelope, which provides mechanical support for the nucleus and anchoring sites for chromosomes and nuclear pores. Additionally, it regulates important cellular events like DNA replication and cell division. The nuclear lamina is mostly composed of lamin proteins (A-type and B-type). Mutations in the human *LMNA* gene lead to various inherited tissue-specific diseases such as Progeria and Emery-Dreifuss muscular dystrophy [4, 5]. Especially in the area of gene regulation, lamins have been reported to tether heterochromatin to the nuclear periphery causing chromatin silencing [6, 7], and also seem to be involved in positioning and repression of a specific set of genes [8, 9].

Chromosomes

organised structures of multiple long linear DNA molecules in complex with DNA-bound proteins such as histones, which contain most of the cell's genetic material. During most of the cell cycle they are organised in a DNA-protein complex known as chromatin, and during cell division the chromatin can be seen to form the well defined chromosomes. Two types of chromatin can be distinguished in interphase: euchromatin that is less compact and contains genes that are frequently transcribed, and heterochromatin that is more compact and consists of mostly transcriptionally inactive, late-replicating genes. Heterochromatin appears as densely staining material clustering around the nucleolus and the nuclear periphery in electron micrographs in differentiated mammalian cells as well as in yeast and flies [10].

The nucleolus

A discrete densely stained and non-membrane bound structure within the nucleus. The nucleolus is composed of proteins and nucleic acids, and is the site of rRNA synthesis, rRNA processing and assembly of ribosomal subunits [11]. The $0.5 - 5.0\,\mu m$ diameter structure consists of three distinguishable regions: the innermost fibrillar centres (FCs), surrounded by the dense fibrillar component (DFC), which is bordered by the granular component (GC). The nucleolus is involved in genome organisation and chromosome positioning in relation to the NOR (nucleolar organiser region) carrying chromosomes [12, 13].

Cajal bodies and Gems

The Cajal body appears as a tangle of coiled fibrillar strands under electron microscope and is a dense foci of distribution for the protein coilin (nucleocytoplasmic-shuttling phosphoprotein) [14]. They typically present as 1 to 10 copies per nucleus with a diameter ranging from $0.2\,\mu m$ to $1.0\,\mu m$. The Cajal bodies are thought to be related to snRNP biogenesis and trafficking of snRNPs and snoRNPs [15].

Gems (gemini of Cajal bodies) are found to be coincident with or adjacent to Cajal bodies with similar size and shape. They contain a protein called survival of motor neurons (SMN) and an associated factor, Gemin2, which is important for the assembly of snRNPs [16].

PML bodies

Promyelocytic leukaemia bodies, also known as nuclear domain 10 (ND10), Kremer bodies, and PML oncogenic domains. They are small spherical domains found scattered throughout the nucleoplasm, typically 10 to 30 copies per nucleus with a size ranging from $0.2 - 1.0\,\mu m$ in diameter [17]. They are often in association with Cajal bodies and cleavage bodies [18]. It has been suggested that they play a role in transcriptional regulation and appear to be targets of viral infection [19].

Splicing speckles

Subnuclear structures that are enriched in pre-mRNA splicing factors [20]. They are located in the interchromatin regions of the nucleoplasm and appear as clusters of interchromatin granules under electron microscope. Speckles are dynamic structures, and their composition and location change in response to mRNA transcription and protein phosphorylation [21].

Besides the above mentioned nuclear components, there are a number of other subnuclear organelles, including OPT (Oct1/PTF/transcription) domains [22], PcG bodies [23], perinucleolar compartment (PNC) and the SAM68 nuclear body [24], which are not discussed here. The studies of these structures have all pointed out that the nucleus is organised into functional subdomains and the arrangements of which is highly related to the multiple nuclear processes.

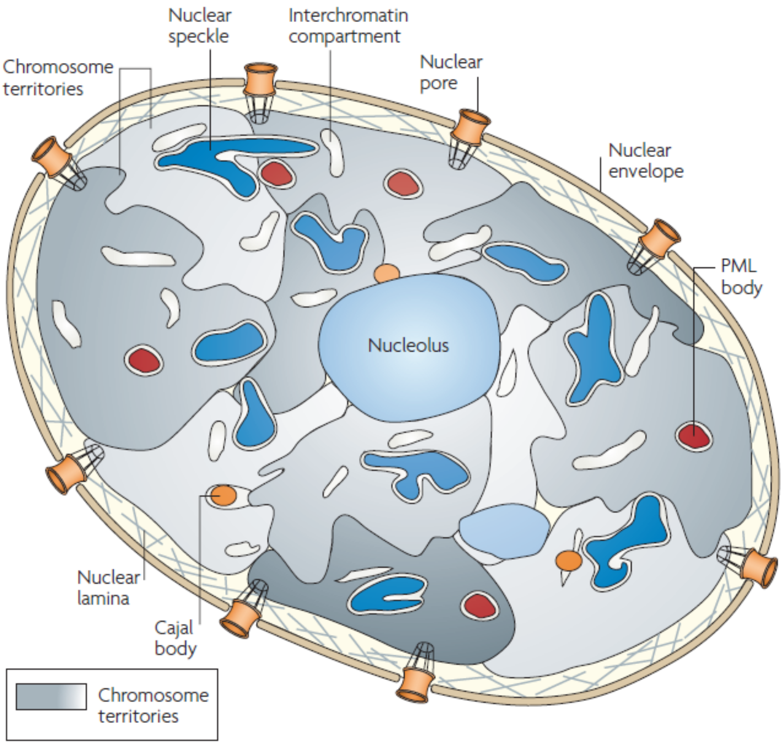

Figure 1.1. **The major nuclear compartments of a mammalian cell nucleus.** The nucleus contains distinct compartments which are functionally organised. The nucleus is enclosed by the nuclear envelope, with nuclear pores inserted in it which serve in the transit of materials between the nucleus and cytoplasm. On the inner face of the nuclear envelope lies a meshwork of intermediate filaments called nuclear lamina. The chromatin in the interphase nucleus is organised into distinct chromosome territories. There are also a number of non-membrane bound compartments, also known as subnuclear bodies, including the nucleolus, Cajal bodies, PML bodies, nuclear speckles and others. The subnuclear bodies have all been reported with distinctive functions, which further proves that the nucleus is not a uniform mixture but organised into functional subdomains.

1.2. Genome Organisation

In this work, the functional higher order and spatial organisation of the genome is of special interest among all the nuclear components. It is already clear that the chromatin in the interphase nucleus is not like tangled threads but arranged in a orderly way. Actually, the first evidence of interphase genome organisation was provided by Cremer and colleagues in 1974, which detected damaged chromosome sites in the metaphase following UV microirradiation of the interphase nucleus of cultured Chinese hamster cells, and showed that the damage sites were restricted in a small number of chromosomes [25, 26]. In the 1980s, with the development of fluorescent *in situ* hybridisation (FISH) with chromosome-specific DNA libraries, it has been widely accepted that interphase chromosomes are compartmentalized with mammalian cell nucleus [27, 28]. Simultaneously whole chromosome painting method has further proved, that chromosomes in the interphase nucleus occupy compact, mutually exclusive and partially intermingled territories (chromosome territories, CTs) which are variable in shape [29, 30] (Figure 1.2 and Figure 1.3). This opinion has been confirmed in live cells more recently using *in vivo* labelling techniques, like tagging arrays of lac operator sequences to individual gene loci, which served as binding sites for lac repressor which was fused with green fluorescent protein (GFP) [32, 33], and incorporation of fluorescent nucleoside analog into the chromatin. In the latter method, the chromatids were labelled randomly during S-phase and segregated to daughter cells in the subsequent mitotic events. Nuclei containing few or even single labelled chromatid territories can be observed after five to ten cell cycles [34, 35].

1.2.1. The Higher-order Chromatin Organisation

The relationship between higher-order chromatin folding and gene's transcriptional activity was noticed by the fact that active genes are often found in less compact euchromatin and silenced genes in condensed heterochromatin [36]. It was suggested that heterochromatin region acted as accessibility barrier which sequestered specific factors [37]. However, this was challenged by the findings in yeast [38]and mammalian cells [39, 40], that heterochromatin proteins were highly dynamic within highly condensed heterochromatin domains and they were in readily exchange among chromatins. Therefore, the accessibility barrier presented by the higher-order chromatin folding probably is not exist and the true barrier lies at the level of the $10\,nm$ nucleosomal fibre or below [41].

Topologically, the transcriptionally active gene region can be significantly more decondensed than the inactive ones, which is reflected in the three- dimensional volume change of the fluorescently labelled gene region, as revealed by *in vivo* [42, 43] and *in vitro* [44] experiments.

Recently a lot studies have pointed out that the regulation of gene expression on higher-order chromatin level is quite likely to be organised by large-scale [45, 46] or local [47, 48] chromatin loops, which are able to place the genome regions in distinct separate nuclear environments to optimize their activity. The formation of chromatin loops can be upon gene activation [49, 50, 51], favor the activation [52] and also contribute to gene silencing [53]. However, how prevalent these effects are remains unknown.

1.2.2. The Spatial Genome Organisation

After the concept of chromosome territory (CT) has been well established, more attention was paid to the nuclear position of the individual chromosomes which was found to be non-random and correlated with gene activity. This was noticed by the fact that in mammalian cells early replicating R-bands which are transcriptionally active are preferentially located in the interior of the nucleus whereas late replicating G/Q bands which are transcriptionally inactive are found predominantly in the nuclear periphery [54, 55]. Recent studies have pointed out that this non-random nuclear radial distribution of chromosomes is related to gene density, chromosome size and the shape of the nucleus.

Non-random Nuclear Radial Positioning - Gene-density Theory

Bickmore and colleagues reported an preferential radial position of human chromosomes HSA18 and HSA19 [56], which demonstrated the chromosome non-random nuclear positioning nature. The two human chromosomes HSA18 and HSA19 are with similar size (85 Mb and 67Mb, which represent 2.6% and 2% of the entire human genome, respectively [57]) but distinct functional characteristics. HSA19 is very gene-rich (28 genes/Mb) and replicates most of its DNA in the early S phase, whereas HSA18 is gene-poor (8 genes/ Mb) and contains a high proportion of late-replicating DNA [58]. It was found in normal human lymphocytes, chromosome 18 localized preferentially at the nuclear periphery and chromosome 19 positioned mostly towards the nuclear interior [56]. Later this finding was extended to all human chromosomes in lymphoblasts and fibroblasts, revealing that most gene-rich chromosomes predominantly localized at the centre of the nucleus, whereas relatively gene-poor chromosomes positioned towards the nuclear periphery [59].

Interestingly, the same gene-density related non-random nuclear radial positioning has been observed in primates [60], Old World monkeys [61] and also in chicken [62], which means this kind of chromosome organisation is probably evolutionary conserved [63].

Non-random Nuclear Radial Positioning - Chromosome Size Theory

It was first proposed by Yokota and colleagues that the the positioning of chromosomes in human G1 interphase nuclei was chromosome size-dependent [64], though preliminary evidence has been reported before [65, 66, 67]. They revealed using telomeric probes that the q-arm telomeres of large chromosomes were more peripherally located than that of small chromosomes. This size-related positioning is possibly due to chromosome volume exclusion or their positions on the metaphase plate. Findings from Cremer and colleagues [68] supported this size-related non-random chromosome positioning theory,

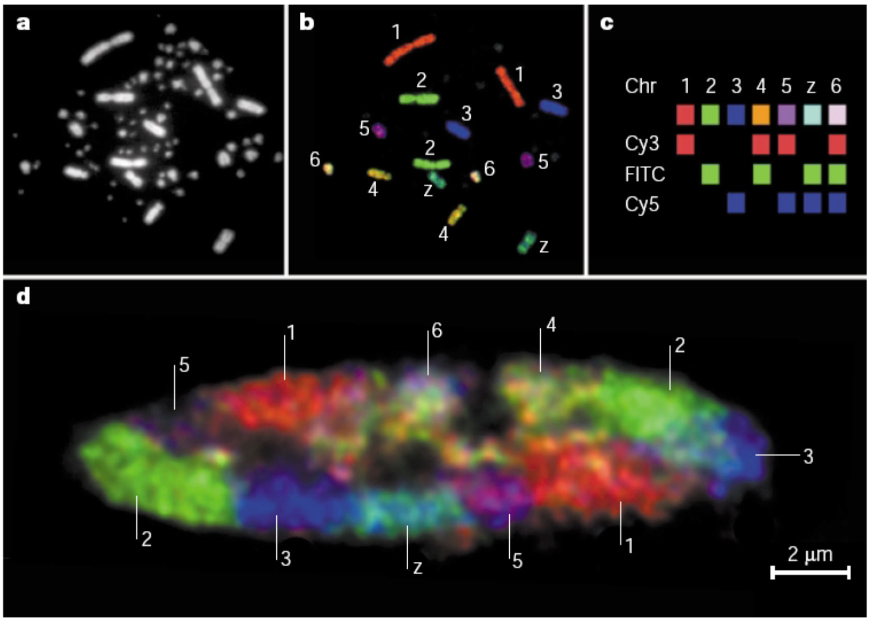

Figure 1.2. **Chromosome territories in the chicken cell nucleus.** a. 4,6-diamidino-2-phenylindole (DAPI)-stained, diploid, chicken metaphase spread with macro- and microchromosomes. b. The same metaphase spread after multicolour fluorescence *in situ* hybridisation with pseudocoloured chromosomes. Chicken chromosome paint probes (image courtesy of Johannes Wienberg) were labelled by a combinatorial scheme with oestradiol (1, 4, 5, 6), digoxigenin (2, 4, 6, Z) and biotin (3, 5, 6, Z). c. Oestradiol- and digoxigenin-labelled probes were detected using secondary antibodies labelled with Cy3 and fluorescein isothiocyanate (FITC); biotinylated probes were detected with Cy5-conjugated streptavidin. d. Mid-plane light optical section through a chicken fibroblast nucleus shows mutually exclusive chromosome territories (CTs) with homologous chromosomes seen in separate locations. (Note that only one of the two CTs for each of 4 and 6 is displayed in this section.) (Image courtesy of F. Habermann.) [29]

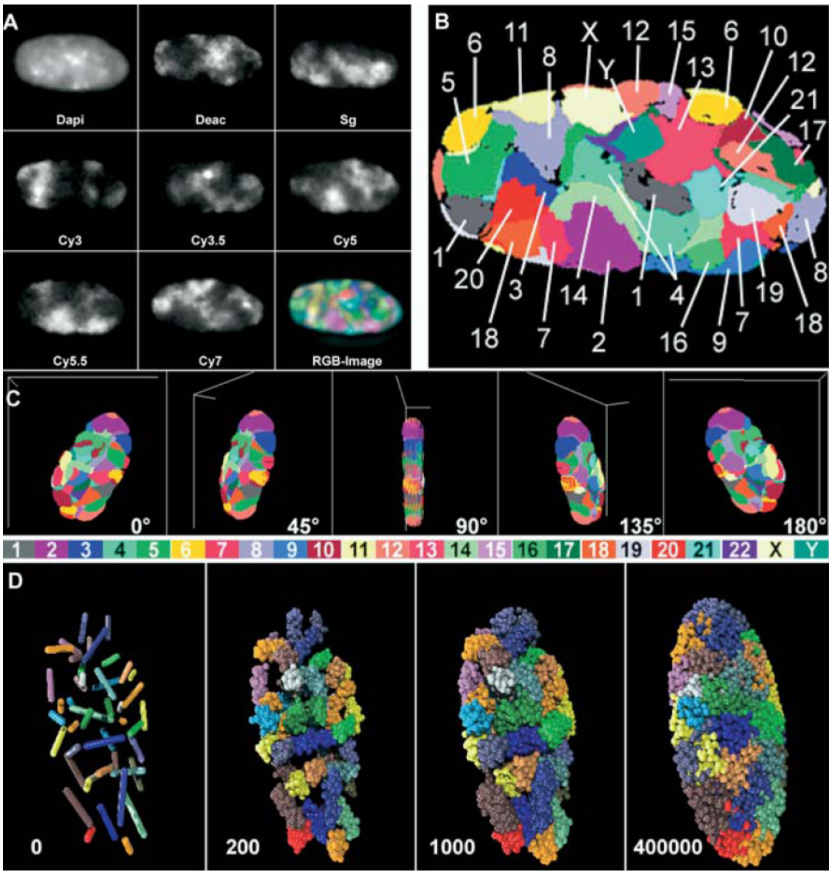

Figure 1.3. **24-colour 3D FISH representation and classification of chromosomes in a human G0 fibroblast nucleus.** A. deconvoluted mid-plane nuclear section recorded by wide-field microscopy in eight channels: one channel for DAPI (DNA counterstain) and seven channels for the following fluorochromes: diethylaminocoumarin (Deac), Spectrum Green (SG), and the cyanine dyes Cy3, Cy3.5, Cy5, Cy5.5, and Cy7. Each channel represents the painting of a CT subset with the respective fluorochrome. RGB images of the 24 differently labelled chromosome types (1–22, X, and Y) were produced by superposition of the seven channels (bottom right). (B) False colour representation of all CTs visible in this mid-section after classification with the program goldFISH. (C) 3D reconstruction of the complete CT arrangement in the nucleus viewed from different angles. (D) Simulation of a human fibroblast model nucleus according to the SCD model. The first image shows 46 statistically placed rods representing the 46 human chromatids. The next three images simulate the decondensation process and show the resulting CT arrangement obtained after different numbers of Monte Carlo relaxation steps (200, 1,000, and 400,000). [31]

but only with ellipsoid nuclei (fibroblasts and amniotic fluid cells), and with spherical nuclei (lymphocytes) the distribution pattern were much different, pointing out that the shape of nuclei also plays a role in chromosome radial positioning.

Note that sometimes chromosomes can be ordered in the nucleus both by size and by gene density [69, 70], implicating that probably the two theories are not mutually exclusive. Besides, chromosome positioning can be dynamic when the status of the cell changes. For example, chromosome 18 moved from a more peripheral to a more central position in human fibroblasts when the cells exited the cell cycle [71].

Gene Activity in Relation to The Nuclear Periphery and the Nuclear Pore Complex

The nuclear periphery has been frequently related with gene silencing, due to the fact that repressed chromatin regions cluster in silent foci at the nuclear periphery [6] and lamin B receptor physically interacts with the heterochromatin protein HP1 [7]. Besides, lamins also seem to be involved in positioning and repression of a specific set of genes [8, 9]. Many cases of gene activation have been observed to correlate with movements away from the nuclear periphery [72, 73, 74], though exceptions also exist [75, 76]. Recent studies have demonstrated that the nuclear periphery is not exclusively repressive but can also favor the enhanced expression of certain genes at the region around the nuclear pore complex [77, 78], probably due to the result of facilitated mRNA export [79]. However, certain position of the gene, periphery or associated with the nuclear pores, can facilitate but is not sufficient for the gene's function, and whether the gene position is the cause or the consequence of transcriptional activation is still unclear [3].

Cancer and Genome Organisation

Changes of chromatin organisation during malignancy have been noticed long ago [80]. Misteli and colleagues did some comparison between mouse lymphoma cells and normal splenocytes [81], showing that the relative arrangement of chromosomes can be conserved between normal and cancer cells and the physical proximity of the chromosomes can facilitate specific translocations. Later Cremer and colleagues found in seven human tumor cell lines chromosome territory 18 and 19 showed an inverted nuclear position compared with that of normal cells, indicating a partial loss of radial chromosome organisation order in tumor cell nuclei [82]. Furthermore, number and morphology of nucleoli [83], distribution patterns of centromeres [84] and telomeres [85] have also been observed to alter in cancer cells. Recently Misteli and colleagues analysed the spatial position of a set of cancer-associated genes in a 3-D cell culture model of early stages of mammary cancer, identifying that several genes are specifically repositioned during tumorigenesis. So far, most of the studies in regard to cancer-related genome organisation are carried out with cultured cell lines or formalin-fixed paraffin-embedded tissue sections [86], however the nuclear structure of the cells in those conditions can be quite different than that of the cells in well-preserved tissues, which still remains to be explored.

Part I

Methods

Chapter 2

The Mouse Model and Mouse Cell Lines

The transgenic mouse model used to study the mammary tumor development was constructed at the Jackson Laboratory [87]. The viral oncogene SV40Tag was targeted to the mouse mammary gland using the regulatory region of the whey acidic protein (WAP) gene (a well-characterized milk protein-encoding gene), creating a mouse model which was histopathologically similar to the case of human breast cancer. Besides, two mouse cell lines were used for testing the hybridisation conditions and also for the SV40 Tag gene size measurement.

2.1. The Simian Virus 40 (SV40)

Simian virus 40 (SV40) is a kind of polyomavirus which is able to transform cells from different species, including normal human cells, into cells with a neoplastic phenotype [88]. SV40 oncogenicity and transforming ability depend strictly on the expression of the early region gene product, the large tumor antigen (T antigen or Tag), which is responsible for both the control of viral infection and the required alterations of cellular processes [89]. T antigen binds to several cellular proteins, like the tumor suppressor gene p53, the retinoblastoma suppressor gene product and DNA polymerase α-primase, which promotes DNA replication and stimulates cell proliferation.

SV40 infects a variety of cultured mammalian cells, but initiates a productive infection cycle only in cells of primate species. Cells of rodents and other mammalian species are nonpermissive for SV40 infection. The infected cells can be immortalized and transformed, which may eventually induce specific types of tumors [90]. Human cells are only semipermissive for SV40 infection. However, about 50 years ago SV40 was introduced into the human population by contaminated polio vaccines and adenovaccines [90, 91]. The SV40 early region gene was found in human brain tumors, 23% of peripheral blood cells samples and also 45% of sperm fluids from healthy individuals [92], which indicates the possible manner of the transmission of SV40 from person to person in the normal human population.

2.2. The Mouse Model

SV40 Tag is an endogenous activated oncogene in transgenic mice. Under the control of the WAP gene promoter, SV40 Tag was introduced to the mammary gland, creating a transgenic mouse model of mammary cancer (Figure 2.1). The transgenic mouse linage, WAPTag 1, which was used in this work, was created by injection of a hybrid gene composed of the WAP regulatory region and the SV40 Tag coding region into zygotes of the inbred C57BL/6J mouse strain. The WAP promoter targeted the viral oncogene SV40 Tag to the mammary epithelium of lactating females. The SV40 Tag gene was transcribed during mid to late pregnancy and during lactation, when the WAP promoter was activated. After several rounds of pregnancy and lactation, mammary abnormalities were observed and finally developed into papillary and then solid carcinoma.

2.3. The Mouse Cell Lines

To establish the hybridisation conditions and also carry out the SV40 Tag gene size measurement experiment, two mouse cell lines were used. C57SV is a mouse fibroblast cell line transformed with SV40 DNA [93]. These fibroblasts do not contain infectious particles since rodents cannot produce whole particles of SV40. However, SV40 will integrate in rodent DNA and transform the cells, making them tumorigenic. MC57G is a mouse cell line derived from 3-methacholanthrene-induced tumor. These cells contain no SV40 DNA and are included as a negative control.

The two cell lines were routinely subcultured in Dulbecco's modified Eagle's medium (DMEM), containing 18% fetal bovine serum, 1% Penicillin/Streptomycin and 1% L-Glutamine, and incubated at 37°C in humidified 5% CO_2 atmosphere. The adherent cells were removed by trypsinization (0.5%/0.2% trypsin/EDTA in D-PBS) for subculturing and fixation.

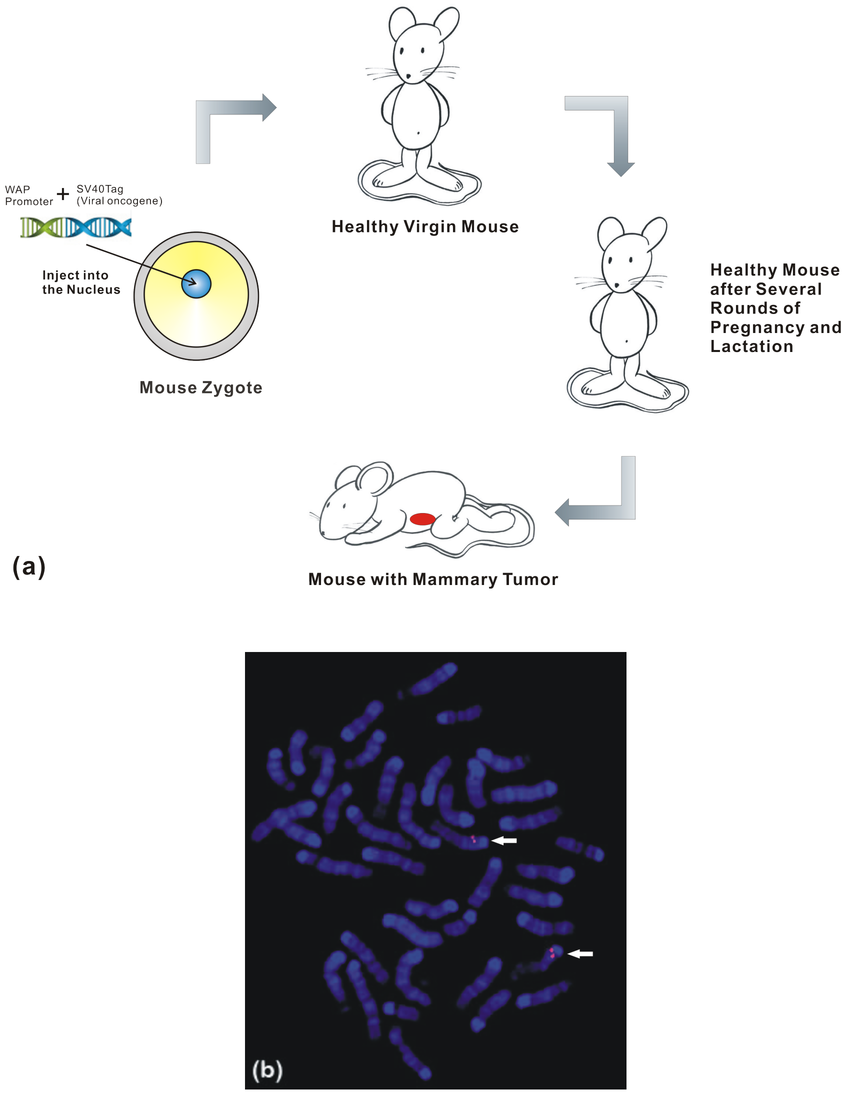

Figure 2.1. **The transgenic mouse model.** **(a)** The construction of the mouse model. The hybrid gene composed of the WAP gene (a milk protein encoding gene) promoter and the SV40 Tag coding region was injected into the zygote of the C57BL/6J mouse. The SV40 Tag gene was transcribed during mid to late pregnancy and during lactation when the WAP gene promoter was activated. After several rounds of pregnancy and lactation, mammary abnormalities were observed and finally developed into papillary and then solid carcinoma. **(b)** The DNA FISH result of the SV40Tag gene in the cells derived from the transgenic mouse. The arrows indicate the SV40Tag gene loci which are located on chromosome 11 according to Giemsa banding. This image was provided by Dr. Anne Peaston in the Jackson Laboratory.

Chapter 3

Cryosections

So far, most of the investigations in nuclear structure and function have been conducted with cultured tumor cell lines, fibroblast or lymphocytes. These studies have produced a lot of basic theories about nuclear organisation, but it was pointed out that cells in monolayer cultures have different nuclear structure comparing with that of the same cells in tissues [94]. Therefore, investigating the genome within the natural context of tissue becomes necessary to avoid obscuration of the differences between normal and malignant cells and give a better view of the higher-order nuclear spatial organisation.

Paraffin-embedded tissue sections were widely used for this purpose. These sections need to go through a de-waxing and a rehydration step before the fluorescence *in situ* hybridisation. And normally these sections are several micrometers thick, so harsh protein digestion step is included to let the probes to penetrate. All these treatments affect the preservation of the nuclear morphology and disturb investigation of the genome organisation.

To avoid the above mentioned drawbacks, Tokuyasu cryosectioning (Figure 3.1) was used to get ultra thin tissue sections in this work. It was developed by K.T. Tokuyasu for the intracellular localization of protein antigens, which avoids prolonged fixation, dehydration, and other harsh chemical or physical treatments [95]. The mouse was first anesthetized and then perfused with 4% ice-cold paraformaldehyde prior to dissection. 1 mm cubes were cut from different parts of the mammary gland and tumor, and were further fixed with 8% paraformaldehyde, which preserved the ultrastructure. Then the tissue blocks were embedded in 2.1 M sucrose in phosphate-buffered saline (PBS), which permeated through the fixed tissue and acted as a cryoprotectant [96, 97]. The tissue blocks were rapidly frozen by immersion in liquid nitrogen and can be stored indefinitely until use. Cryosections (about 200 nm thick) were cut using an ultracryomicrotome, captured on sucrose drops and transferred to a glass coverslip. The sucrose can be washed away prior to fluorescence *in situ* hybridisation by rinsing in PBS, yielding a thin section of fixed material that is not hindered by paraffin, and has not been subjected to detergents, organic solvents, drying or high temperatures, all of which can induce distortion of nuclear structure.

With Tokuyasu cryosectioning, increased probe accessibility allowed for the use of more stringent chemical fixation to give better structural preservation. The use of thin (about 200 nm) sections significantly improved imaging resolution, especially in the z-axis, and the ability to resolve chromosome territory organisation during interphase. Because of the direct probe accessibility, no harsh protein digestion step was needed before hybridisation (only

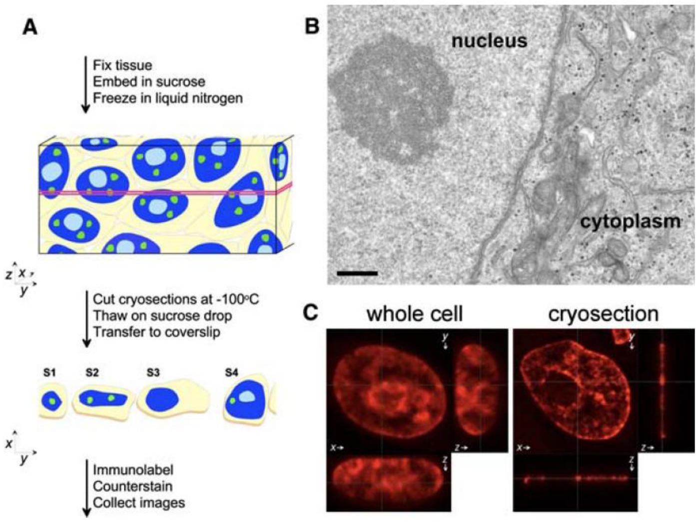

Figure 3.1. **Tokuyasu cryosectioning.** A. Cells or tissues go through chemical fixation, sucrose embedding and freezing in liquid nitrogen, before thin sections are cut by ultracryomicrotomy. Frozen sections are collected on sucrose drops, transferred to a solid support (glass coverslip or plastic coated metal grids). The sucrose will be washed away before labelling with antibodies or nucleic acid probes. The different cellular profiles present in a cryosection (along red lines: S1 − 4) originate from different cells in the tissue and represent the different parts of the nucleus. Pale yellow, cytoplasm; blue, nucleus; aqua, nucleoli; green, splicing speckles. B. Tokuyasu cryosections are obtained from cells fixed in conditions that preserve cell ultrastructure. HeLa cells were fixed as for cryosectioning, stained and Epon-embedded [96]; imaging by electron microscopy shows good preservation of membrane integrity, organelles (e.g. mitochondria) and nucleolus. Bar 500 nm. C. Thin cryosections provide optimal imaging condition for high resolution and contrast on fluorescence microscopes. 3D stacks were collected from whole HeLa cells or cryosections stained with TOTO-3, a nucleic acid dye. The images are adapted from [98].

with 0.1 M HCl for 10 min), which caused less damage to the nuclear morphology and further preserved nuclear ultrastructure. Pombo and colleagues have used 5 *nm* gold particles to immunolabel the histone H2B, and the images before and after *in situ* hybridisation showed that the gold particles are spatially preserved in both heterochromatic and euchromatic regions, which means the chromatin nanostructure is preserved during cryo-FISH [30].

Chapter 4

Molecular Cytogenetic Procedures

Fluorescence *in situ* hybridisation (FISH) is a cytogenetic technique that uses fluorescent labelled DNA sequences (probes) to detect specific DNA sequences on the chromosomes and in the native context of cell morphology. This technology was developed over two decades ago and has become one of the most important biological assays in both basic research and clinical diagnosis today [99]. Various FISH methods originated from the basic protocol has been reported these days, like COMBO-FISH (a method with no requirement for sample denaturation prior to hybridisation [100]), Immuno-FISH (a method combines both standard FISH and immunolabelling [101]), M-FISH (also known as Multicolour-FISH, a protocol for 24-colour karyotyping [102]), 3-D FISH (a method which can preserve nuclear architecture and large-scale chromatin organisation [103]) and so on. The cryo-FISH technique used in this work was introduced recently by Pombo and colleagues [30] which makes use of ultrathin cryosections ($150 - 200\,nm$ thick) of well-fixed, sucrose-embedded cells or tissue blocks. This method manages to preserve chromatin nanostructure while presenting a high efficiency of hybridisation and increased image resolution, which makes it ideal for the study of genome organisation.

The probes used for *in situ* hybridisation can be cloned probes, enzymatically amplified probes and chemically synthesized probes. They can be labelled either directly, by incorporation of fluorescent nucleotides, or indirectly, by incorporation of reporter molecules that are subsequently detected by fluorescent antibodies or other affinity molecules [104]. In this work, the probes used for detecting the SV40Tag gene were derived from plasmids, which were first isolated and then labelled by incorporation of Alexa 568 conjugated nucleotides with nick translation. The probes used for whole chromosome painting were Cy3 labelled and directly purchased from Cambio, UK. The probes however often contain repetitive sequences which will cause high background fluorescence, therefore need to be pretreated with unlabelled competitor nucleic acids which will compete with the specimens for non-specific binding sites.

The details of the molecular cytogenetic techniques used in this work will be briefly discussed in this chapter.

4.1. Plasmid Preparation

The probes used for hybridizing the SV40Tag gene were derived from plasmids. A standard alkaline lysis was performed using the *QIAprep*®

miniprep Kit. The *E.coli* bacteria containing the plasmid of interest was first grown, then lysed with a strong alkaline buffer which broke the cell membrane and denatured the proteins. Through a series of steps involving agitation, precipitation, centrifugation, and removal of supernatant, cellular debris was removed and the plasmid was isolated and purified. The detailed protocol can be found in the *QIAprep®* Miniprep Handbook [105], with the main steps listed here.
Protocol:

1. Pick a single colony of the DH5α *E.coli* bacteria containing the constructed plasmid from a freshly streaked selective plate and inoculate a culture of 3 ml LB medium containing 7 μl ampicilin. Incubate for 15 h at 37 °C with vigorous shaking.
2. Harvest the bacterial cells by taking 2 ml culture and centrifugation at 13000 rpm in a conventional, table-top microcentrifuge for 30 s at room temperature.
    - Note: The following steps are all carried out at room temperature.
3. Resuspend pelleted bacterial cells in 250 μl Buffer P1 and transfer to a microcentrifuge tube.
4. Add 250 μl Buffer P2 and mix thoroughly by inverting the tube 4–6 times.
5. Add 350 μl Buffer N3 and mix immediately and thoroughly by inverting the tube 4–6 times.
6. Centrifuge for 10 min at 13000 rpm in a table-top microcentrifuge.
7. Apply the supernatant from step 4 to the QIAprep spin column by decanting or pipetting.
8. Centrifuge for 30–60 s. Discard the flow-through.
9. Wash the QIAprep spin column by adding 0.5 ml Buffer PB and centrifuging for 30–60 s. Discard the flow-through.
10. Wash QIAprep spin column by adding 0.75 ml Buffer PE and centrifuging for 30–60 s.
11. Discard the flow-through, and centrifuge for an additional 2 min to remove residual wash buffer.
12. Place the QIAprep column in a clean 1.5 ml microcentrifuge tube. To elute DNA, add 50 μl Buffer EB (10 mM Tris · Cl, pH 8.5) or water to the centre of each QIAprep spin column, let stand for 1 min, and centrifuge for 2 min.

The purified plasmid DNA can then be labelled by nick translation. Here it is not necessary to eliminate vector DNA from the preparation, since they don't efficiently hybridize to the mammalian target sequences.

4.2. Nick Translation

Nick translation is a procedure for making DNA probe when sufficient clean DNA template is available. The DNA template is treated with DNase to produce single-stranded nicks, followed by incorporation of fluorescently labelled nucleotides from the nick sites by DNA polymerase I. Besides labelling the probe, the other purpose of nick translation is to reduce the size of the probe to a proper length. Too large probes can cause severe background problems and too small probes can be easily washed away in *in situ* hybridisation. Usually the probe length shall be under 500 *bp*, and in this work it was from 200 *bp* to 400 *bp* as controlled by TAE agarose gel electrophoresis.

The reagents for nick translation should be handled on ice. The light-sensitive fluorochrome should be covered (light-prove) during the operation steps. For the labelling purpose, $1\,\mu g$ DNA is used, which is equivalent to $10\,\mu l$ plasmid-DNA.

Protocol:

For a $50\,\mu l$ nick translation reaction, mix the following reagents as indicated in the table:

- β-Mercaptoethanol (0.1 M; AppliChem, Darmstadt)
- DNA-Polymerase I ($5\,U/\mu l$; endonuclease free; Roche Diagnostics GmbH, Penzberg)
- 10 x nick translation-buffer: 0.5 M Tris-b (with HCl pH 8.0) (Gerbu Biotechnik, Gaiberg) + 50 mM $MgCl_2$ (J.T. Baker B.V., Deventer NL) + 0.5 mg/ml Albumin, Bovine Fraction V (Sigma Aldrich Chemie GmbH, Steinheim)
- DNase I - stock (3 mg/ml): $300\,\mu l$ 0.3 M NaCl + $200\,\mu l$ DNase I, RNase free (10000 U/ml; for 2000 U $200\,\mu l$ is used; Roche Diagnostics GmbH, Penzberg) + $500\,\mu l$ Glycerol (filtered to be sterile)
- AGC-stock: $0.5\,\mu l$ dATP (100 mM, pH7.5) + $0.5\,\mu l$ dGTP (100 mM, pH 7.5) + $0.5\,\mu l$ dCTP (100 mM, pH 7.5) add ddH_2O to $100\,\mu l$
- Fluorochrome: ChromaTide® Alexa Fluor®488-5-dUTP, 1mM in TE buffer (Molecular Probes, USA)

	Volume (μl)	Final Concentration
ddH_2O	Add to $50\,\mu l$	
10x nick translation-buffer	5	1x
0.1 M β-Mercaptoethanol	5	0.01 M
0.5 mM AGC	5	0.05 mM
Fluorochrome	1	
DNA	10	
DNase I (1 : 10000 in 4 °C ddH_2O)	3	
DNA Polymerase I	1	$0.1\,U/\mu l$

Incubate the reaction in a waterbath at 15 °C without light for $90 - 120$ minutes. The incubation time depends on the desired fragment length. The shorter the incubation time, the longer the fragment. After that, put the reaction mixture immediately on ice to inhibit the DNase I activity. Check the size of the labelled fragments by TAE agarose gel electrophoresis. If the size is too large, put DNase I (1 : 1000) into the reaction mixture again and incubate at 15 °C until the size is proper ($200 - 400\,bp$). The labelled probe can be stored at -20 °C.

4.3. Repetitive Sequences Blocking

The labelled probes from the nick translation experiment are not ready to use, since they often contain repetitive sequences which will cause high background fluorescence in the hybridisation experiments. Cot-1 DNA was used to suppress the non-specific hybridisation caused by the repetitive sequences in the probe.

Protocol:

Prepare the following reagents:

- Mouse Cot-1 DNA (1 mg/ml; Invitrogen GmbH, Karlsruhe)
- Sodium Acetate (3 M, pH5.29)
- Ethanol (Merck, Darmstadt)
- Hybridisation buffer - Solution 1: Deionized formamide (99.5%, pH7; Sigma-Aldrich Chemie GmbH, Steinheim)
- Hybridisation buffer - Solution 2: 30% Dextran sulphate (Sigma-Aldrich Chemie GmbH, Steinheim) in 4 x SSC (Sigma-Aldrich Chemie GmbH, Steinheim)

Note: The hybridisation buffer is composed of 50% “solution 1” and 50% “solution 2”, therefore the end product is 50% deionized formamide and 15% dextran sulphate in 2 x SSC.

The components of hybridisation buffer is crucial for the efficiency of the hybridisation process, whose functions are described as follows.

Deionized formamide

It is a denaturing agent for nucleic acids. It acts by decreasing the melting temperature of DNA double helix, and therefore also stabilizes the single strands of denatured DNA.

Dextran sulphate

It has been found to be able to accelerate the hybridisation rates of single strand DNA, probably by reducing the amount of hydrating water for dissolving the nucleotides which therefore effectively increases the probe concentration.

SSC

It is the abbreviation of the saline-sodium citrate (SSC) buffer. It interacts mainly with the phosphate groups of the nuclei acids to decrease the electrostatic interactions of the double strands.

The handling of the reagents shall be carried out on ice. During the operation, the probe shall be covered from light. For 10 μl DNA, the reagents volumes are as follows:

Reagents	Volume (μl)
DNA (μl)	10
Cot-1 DNA (μl)	10
Sum (μl)	20
3 M NaOAc (1/10 vol.)	2.0
100% Ethanol (−20 °C) (2.5 x vol.)	55

1. Precipitate the reagents at −20 °C overnight or at −80 °C for 30 min.
2. Centrifuge the tube for 30 min at 13000 rpm at 4 °C and then remove the supernatant.
3. Wash the pellet with 200 μl 70% ethanol (−20 °C).
4. Centrifuge the tube for 10 min at 13000 rpm at 4 °C and then remove the supernatant.
5. Air dry the pellet at RT or in the hot block (42 °C).
6. Resuspend the pellet in 4 μl deionized formamide (“hybridisation buffer solution 1”) at 42 °C in the hot block with moderate vibration. Usually 3 − 4 hours are needed for a sufficient solving.
7. Add 4 μl “hybridisation buffer solution 2”, briefly vortex and centrifuge.
8. Denature the probe at 75 °C for 10 min (the temperature and time depend on the probe!).
9. Hold the probe for 30 min-1 h at 37 °C before apply it to the specimen.

Usually the hybridisation experiment can be carried out simultaneously after Step 5.

4.4. Fluorescent *in situ* Hybridisation using Fixed Cells

One of the advantages of fluorescent *in situ* hybridisation is its ability to localize and detect specific nucleic acid targets in morphologically preserved cell preparations. Therefore, in order to hybridise the target sequences localized inside the cells, the first step is sample permeabilization.

Pepsin is an enzyme that breaks down proteins into polypeptides. Since it is originally released in the stomach to degrade food proteins, it functions best in acidic environments at a temperature between 37 °C and 42 °C. In this work, 0.03% pepsin in 0.01 N HCl was used, to digest the membrane proteins as well as the proteins that surrounds the target sequence. The optimal reaction time was determined by parallel experiments. Since the C57SV and MC57G cell lines used in this experiment have a high background in the nuclei caused by nuclear proteins, 30 s, 1 min, 2 min and 5 min pepsin digestion time were used under the same conditions, and 5 min digestion has been proved to effectively reduce the background fluorescence, which is very important for the following gene size measurement.

In this experiment, to avoid the background caused by the RNA in the nuclei and cytoplasm, additional RNase (Ribonuclease, a nuclease that catalyzes the degradation of RNA) treatment was added.

After the sample was dehydrated by serial immersion in ethanol series with increasing concentration, the target chromosomes were denatured in 70% formamide in 2 x SSC (pH 7.0) at 72 °C for 2 min, followed by rinsing in the ethanol series again. Then the probe (from Section 4.3) in hybridization buffer was added to the denatured sample and they were incubated for over 48 h at 37 °C in a humidified chamber.

Post-hybridisation washes are required to remove the unbound probe and the probe which are loosely bound to the sites other than the target sequences. The stringent wash normally is done with 0.1 − 2 x SSC at temperatures between 25 and 75 °C. The less concentrate the salt solution, the longer the duration of the wash and the higher the temperature, the higher the stringency. Since the probes used in this experiment is very short (under 500 bp, see Section 4.2), the stringency should be lowered accordingly to avoid losing too much hybridisation signals. Here washing in 4 x SSC for 3 x 5 min at 42 °C was used and it proved to be appropriate.

In the end, the slide or coverslip should be briefly rinsed in water to remove the SSC, then air-dried at room temperature and mounted with the antifade solution.

Protocol:

This protocol is for hybridising the SV40Tag gene in the methanol and acetic acid fixed C57SV cells and MC57G cells (control). Since the effective imaging resolution and signal strength will decrease with the distance between the objects and the coverslip, the cells were prepared on the coverslip instead of on the slide.

Use 70% Ethanol to wash the coverslip and dry it with tissue paper. Put it into −20 °C for about 1 min till the surface is wet, then drop about 20 μl cell solution onto the coverslip. Check the spread under a light-field microscope before proceed with the following steps.

Optional: Age the specimen in room temperature over night, which can make the chromosomes combine tighter with the glass surface and also increase the hardness of the chromosomes.

1. RNase Digestion
    a) Wash the coverslip for 5 min in 2 x SSC.
    b) Incubate the coverslip in a humidified chamber for 1 h at 37 °C with RNase solution(1 μl RNase from stock + 99 μl 2 x SSC).
    Note: RNase stock is 10 mg/ml RNase in 10 mM Tris-HCl, stored in −20 °C.
    a) Wash the coverslip for 5 min in 2 x SSC.
2. Pepsin Digestion
    a) Wash the coverslip for 5 min in 1 x PBS.
    b) Incubate the coverslip for 5 min at 37 °C in Pepsin solution.
    Note:
    Pepsin solution is 21 μl Pepsin from stock solved in 70 ml 0.01 N HCl (pre-warmed to 37°C).
    Pepsin stock is 100 mg/ml pepsin in 0.01 N HCl (pH 2.3), stored in −20 °C.
    a) Wash the coverslip for 5 min in 1 x PBS.
3. Sample Denaturation
    a) Dehydrate the sample in 70%, 90%, 100% ethanol series (room temperature) for 3 min each. Air dry.
    b) Denature it in 70% Formamide/2 x SSC, pH 7.0, at 72 °C for 2 min.
    c) Dehydrate the sample in −20 °C 70%, 90%, 100% ethanol series for 3 min each. Air dry.
4. Probe Denaturation

   a) Repetitive sequences blocking (see Section 4.3).
   b) Apply the probe to denatured sample, seal with Fixogum (rubber cement) and continue with hybridisation.
5. Hybridisation
   a) Incubate for over 48 h at 37 °C in a humidified chamber.
6. Post-hybridisation Wash
   a) To remove the slide, dip in 2 x SSC at RT.
   b) Wash the coverslip in 4 x SSC for 3 x 5 min at 42 °C without agitation.
   c) Wash the coverslip for 5 min in 1 x PBS at RT. Check under confocal microscope before proceed to counterstaining.
7. Counterstain
   a) Apply 20 μl ToPro3 iodide (1 : 1000 diluted in 1 x PBS) for 1 min.
   b) Wash in 1 x PBS for 5 min.
8. Briefly rinse the coverslip in water. Air dry. Add a drop of VECTASHIELD (Invitrogen) on the coverslip, seal with Fixogum (or nail polish for long time storage). Proceed with Microscopy.

4.5. Fluorescent *in situ* Hybridisation using Cryosections (Cryo-FISH)

The hybridisation conditions developed for thin cryosections (Cryo-FISH) are consistent with the general concept of fluorescent *in situ* hybridisation. Since the about 200 nm thickness of cryosections allows direct probe accessibility, no harsh protein digestion step is needed before the hybridisation, except for 0.1 M HCl for 10 min, which causes less damage to the nuclear morphology comparing with pepsin digestion and preserves the nuclear ultrastructure.

One important thing is the handling of cryosections must be very gentle. The mouse mammary gland cryosections used in this work were attached to the small round coverslips and embedded with sucrose-based embedding medium. At the beginning of the experiment, the whole slide need to be immersed in 1 x PBS for 1 to 1.5 hour at room temperature, until the coverslip float by itself. Here no organic solvant should be included and also no mechanical pulling or tearing, since they will destroy the morphology of the cryosection. The sample should be handled in the same way prior to post-hybridisation washes for the same reason.

The Cryo-FISH protocol used in this work was adapted from the method used in [30] with slight adjustments, especially in the post-hybridisation wash conditions. The first step of washes is incubating the sample in 50% Formamid/ 2 x SSC for 3 x 25 min at 42 °C, during which the excess probe and the hybridisation buffer are removed. The second step is the stringent wash in 1 x SSC for 3 x 30 min at 42 °C. To avoid losing the hybridisation signal, the concentration of SSC is enhanced from 0.1 x to 1 x and the temperature is lowered from 60 °C to 42 °C here, which reduces the stringency of the wash. At last is a detergent wash using 4 x SSC with 0.1% Tween-20 at 42 °C for 10 min.

Protocol for Whole Chromosome Painting:

1. Carefully wash the nail polish and the sucrose-based embedding medium off by dipping the slides in 1 x PBS for 1 to 1.5 hour at room temperature, until the coverslip float by itself.
2. Rinse the coverslip shortly in 1 x PBS
3. Incubate the section with RNase/2 x SSC (final concentration 250 μg/ml) for 1 h at 37 °C in a humidified chamber.
4. Wash the section in 1 x PBS for 5 min.
5. Incubate the section in 0.1 M HCl at room temperature for 10 min.
6. Wash the section in 1 x PBS for 5 min.
7. Dehydrate the section in 70%, 90%, 100% ethanol series (on ice) for 5 min each. Air dry.
8. Denaturate the DNA by incubating in 70% Formamid/ 2 x SSC at 80 °C for 8 min.
9. Dehydrate the section in ice-cold 70%, 90%, 100% ethanol series for 5 min each. Air dry.
10. The chromosome paints (Cambio, UK) need to be prewarmed to 37 °C. Before use, vortex and centrifuge for $1 - 3$ seconds. Denature the probe for 10 min at 65 °C, and hold at 37 °C for $30 - 60$ min.
11. Add the probe onto the section. Seal with Fixogum and incubate in a humidified chamber overnight.
12. Post-hybridisation wash.
    a) Remove the Fixogum and wash carefully in 1 x PBS until the coverslip float.
    b) Stringency Wash - Wash the section in 50% Formamid/ 2 x SSC for 3 x 25 min at 42 °C.
    c) Stringency Wash - Wash in 1 x SSC for 3 x 30 min at 42 °C.
    d) Detergent Wash - Wash the section in 4 x SSC with 0.1% Tween-20 at 42 °C for 10 min.
13. Counterstain with DAPI (20 ng/ml in 1 x PBS with 0.1% Tween-20) for 10 min. Wash in 1 x PBS for 3 x 5 min.
14. Briefly rinse the coverslip in water. Air dry. Apply the mounting medium (Prolong Gold) and proceed to microscopy.

Protocol for Co-hybridisation:

For co-hybridisation of SV40Tag gene and chromosome 11 using cryosections, the protocol is the combination of the repetitive sequences blocking of SV40Tag gene probe (see Section 4.3) and the whole chromosome painting method described above. Only at the 6th step of repetitive sequences blocking, use the ready-to-use chromosome paints instead of the hybridisation buffer to solve the pellet, and the denaturation temperature of the probes should be 75 °C (the higher one of the two probes), also the hybridisation time should be over 48 hours (the longer one of the two probes).

4.6. MAA Fixation

Fixation is important for preserving the cells and tissues in a close to life-like state for further research use. “MAA” here stands for methanol and acetic acid, which are both protein-denaturing agents. They are used in combination because the shrinkage effect caused by methanol will neutralize the swelling effect cause by acetic acid to some extent.

The protocol here is also for preparing metaphase chromosome spread. Colcemid is able to inactivate spindle fibre formation and thus arrest cells in metaphase. 75 mM KCl here serves as a hypotonic solvent to swell the cells, therefore the cells break more easily when dropped onto the slide. For nuclear structure measurement, these two steps are not necessary.

Protocol:

1. Split the cells on the previous day in order to reach 80% confluency.
2. Renew the medium and add 0.5 μg/ml Colcemid (CaryoMax).
3. After 1 h 30 min incubation at 37 °C, vigorously shake the culture flask and collect the supernatant. Trypsinize the remaining adherent cells, centrifuge them together with the previously collected supernatant at 1000 g for 10 min at RT.
4. Re-suspend the pellet in 300 to 500 μl fresh medium. Add pre-warmed (37 °C) 75 mM KCl dropwise to a final volume equal to the original culture volume. As soon as there are about 3 ml KCl in the tube, the rest can be dropped faster.
5. Incubate the cells for 30 min at 37 °C in a water bath. Pellet by centrifugation and gently resuspend in 300 to 500 μl KCl solution.
6. Add the ice cold fixation solution (freshly prepared methanol / glacial acetic acid, 3 : 1 (vol/vol)) dropwise to a final volume equal to the original culture volume.
7. Incubate the cells for 30 min at –20 °C.
8. Centrifuge at 1000 rpm for 5 min at RT and resuspend the pellet in 2 ml fixation solution. Repeat the step for five times.
9. After the last washing step, resuspend the cells in 100 to 500 μl fixation solution. The solution can be stored in −20 °C for months.
10. Before use, the cell solution can be dropped from 10 to 30 cm height on the inclined slides. Breathing on the slides or putting the slides shortly in −20 °C prior to the dropping facilitated chromosome spreading. Check the spread under microscope.

Chapter 5

Fluorescence Microscopy

A fluorescence microscope is a light microscope used to study properties of organic or inorganic substances using the phenomena of fluorescence and phosphorescence instead of, or in addition to, reflection and absorption.[109, 110] The technique of fluorescence microscopy has become an essential tool in biology and the biomedical sciences as well as in materials science. The application of various fluorophores has made it possible to identify cells and sub-microscopic cellular components with a high degree of specificity.

A fluorophore is a chemical moiety which absorbs energy provided by a light source with a suitable wavelength and then emits lower energy at a longer wavelength, in which process fluorescence can be observed. The difference in energy or wavelength of excitation and emission is called the Stokes shift. This is a critical element in fluorescence imaging since the detection system must exclude wavelengths of light from the excitation source. Generally fluorophores with larger Stoke shifts are preferred since they allow the using of filter sets that have wider bandwidths to permit maximum capture sensitivity.

Fluorescence microscope has been widely used to study tissue, cell or subcellular structures labelled with various fluorescent probes. Most fluorescence microscopes in use are epifluorescence microscopes. These microscopes have become an important part in the field of biology, opening the doors for more advanced microscope designs, such as the confocal laser scanning microscope and the Vertico SMI microscope which combines localisation microscopy with spatially modulated illumination using standard fluorescence dyes to reach an optical resolution below 10 nanometers ($1\,\mathrm{nanometer} = 1\,\mathrm{nm} = 1 \times 10^{-9}\,\mathrm{m}$).

5.1. Epifluorescence Microscopy

Epifluorescence microscopy is a method of fluorescence microscopy that is widely used in life sciences. Figure 5.1 demonstrates the light path of an epifluorescence microscope. The excitatory light is passed from above (or, for inverted microscopes, from below), through the objective and then onto the specimen instead of passing it first through the specimen. The fluorescence in the specimen gives rise to emitted light which is focused to the detector by the same objective that is used for the excitation. A filter between the objective and the detector filters out the excitation light from fluorescent light. Since most of the excitatory light is transmitted through the specimen, only reflected excitatory light reaches the objective together

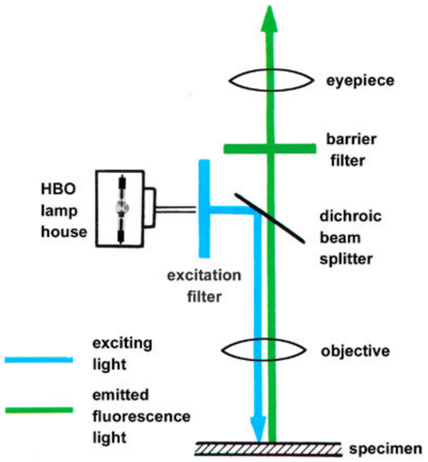

Figure 5.1. **Schematic show of the light path of the epifluorescence microscope.** [111]

with the emitted light and this method therefore gives an improved signal to noise ratio.

5.2. Image Formation, PSF and Resolution

In linear systems like fluorescent microscopes, image formation is linear in complex field when the light is coherent. This means that when two objects A and B are imaged simultaneously, the result is equal to the sum of the independently imaged objects. The image of an object in a microscope can be computed by expressing the object-plane field as a weighted sum over 2D impulse functions, and then expressing the image plane field as the weighted sum over the images of these impulse functions (Figure 5.2). This is known as the superposition principle, valid for linear systems. The image of the individual object-plane impulse function is called point spread function (PSF), which maps the intensity distribution of an infinitely small point object in the image plane. When the object is divided into discrete point objects of varying intensity, the image is computed as a sum of the PSF of each point.

All optical microscopes are limited in resolution determined by a series of physical factors [112, 115, 116]. The resolution of an optical microscope is defined as the shortest distance between two points on a specimen that can still be distinguished as separate entities. As demonstrated in Figure 5.3, point sources of light from a specimen appear as Airy diffraction patterns at the microscope intermediate image plane. Although the intensity point spread function extends in all three dimensions, usually only the lateral components of the intensity distribution, refered as the Airy disk [118], is considered.

The limit of resolution of a microscope objective refers to its ability to distinguish between two closely spaced Airy disks in the diffraction pattern. There are various criteria to determine the resolution of an optical system. Here are the most common ones:

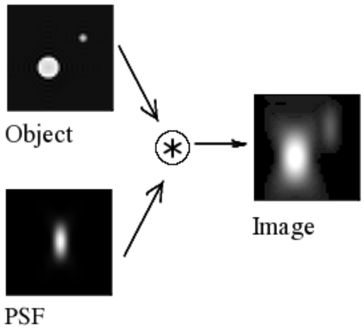

Figure 5.2. **Image formation in a confocal microscope (XZ slice).** The PSF weighted with the amplitude of the object at every point forms the image of the object. (Wikipedia)

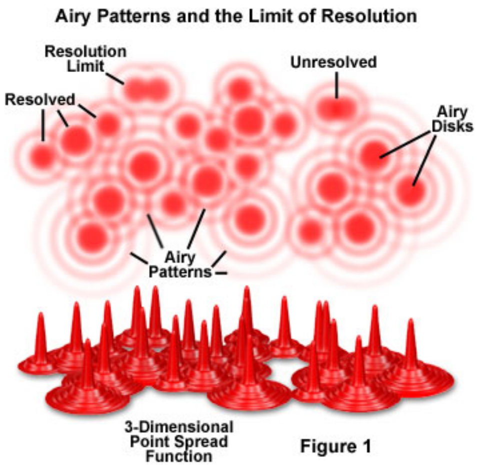

Figure 5.3. **Airy patterns and the limit of resolution.** [117]

Abbe Criterion

According to Abbe [119], exact spacing in the specimen can be resolved when the numerical aperture of the objective lens is large enough to capture the first order differaction pattern produced in a differaction-limited microscope at a specific wavelength. It is expressed as:

$$D = \lambda/2NA$$

where D is the lateral resolution, λ is the wavelength of the illuminating light, NA is the numerical aperture of the objective, given by the formula $NA = n\sin(\theta)$, with n the refractive index of the immersion media and θ the lens aperture angle.

Rayleigh Criterion

Rayleigh Criterion [120] defines an empirical diffraction limit: two point like objects are said to be resolved when the distance between them is greater than the distance between the maximum and the first minimum of the diffraction pattern. For a spherical aperture,

$$D = 0.61\lambda/NA$$

FWHM Criterion

Since resolution is defined as the minimum separation distance at which the two objects can be sufficiently distinguished, obviously this property is related to the width of the intensity peaks (the point spread function). Therefore microscope resolution is directly related to the full width at half maximum (FWHM) of the PSF [121]. For a circular aperture,

$$FWHM = 0.51\lambda/NA$$

5.3. Confocal Laser Scanning Microscopy

Confocal laser scanning microscopy (CLSM or LSCM) has become an essential tool for the investigations in biological and medical sciences, with the ability to obtain high-resolution optical images with depth selectivity in living and fixed specimens [112, 113]. When fluorescent specimens are imaged using a conventional widefield optical microscope, secondary fluorescence emitted by the specimen that appears away from the region of interest often interferes with the resolution of in-focus features. This situation is especially problematic for specimens having a thickness greater than about 2 micrometers. Confocal laser scanning microscopy solves this problem by excluding out-of-focus light and acquiring in-focus images from selected depths, a process known as optical-sectioning. The images are acquired in a point-by-point way and the information about the entire specimen can be obtained and then reconstructed by the computer, making three-dimensional reconstructions of topologically-complex objects possible.

The decisive feature of a confocal laser scanning microscope is the confocal aperture (usually called pinhole) arranged in a plane conjugate to the intermediate image plane and, thus, to the object plane of the microscope.

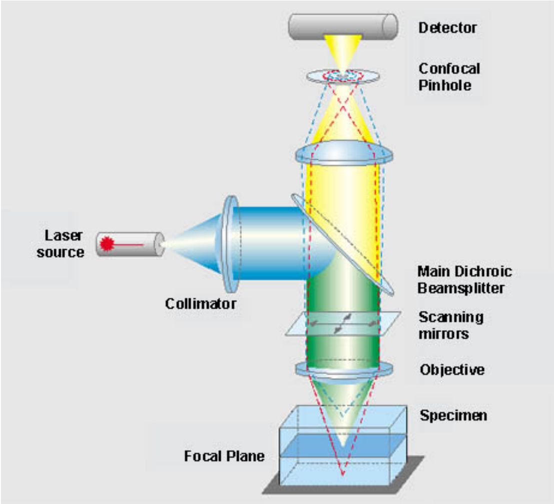

Figure 5.4. **The light path of the confocal laser scanning microscope.**[114]

As a result, the detector (PMT) can only detect light that has passed the pinhole. The pinhole diameter is ideally infinitely small, and thus the detector looks at a point (point detection). Scattered and reflected laser light as well as any fluorescent light from the illuminated spot is then re-collected by the objective lens. The out-of-focus light is mostly blocked by the pinhole, which results in sharper images than those from conventional fluorescence microscopy techniques and permits one to obtain images of planes at various depths within the sample. (Figure 5.4)

Besides the above mentioned advantages of CLSM, the lateral and axial resolution have also been modestly improved comparing with that of widefield microscope. In CLSM, both illumination and detection are limited to a point. The lateral (and axial) extent of the PSF is therefore reduced by about 30 percent compared to that in the widefield microscope. The lateral and axial resolution [122, 123] for the confocal configuration can be calculated with:

$$R_{lateral} = 0.4\lambda/NA$$

$$R_{axial} = 1.4\lambda \cdot \eta/NA^2$$

Where η is the refraction index.

5.4. Spatially Modulated Illumination Microscopy

Since the optical resolution of microscopes is directly related to the width of the point spread function (PSF), many PSF engineering methods have evolved to narrow the full width at half maximum (FWHM) of the microscopic PSF to enhance the optical resolution. Such methods like 4Pi microscopy [124, 125] and stimulated emission depletion microscopy (STED) [126] can bring the optical resolution down to less than 100 nm and even to the macromolecular scale [127]. Spatially modulated illumination microscopy is another kind of PSF engineering microscopy. SMI microscopy does not directly improve the optical resolution (the lateral optical resolution of SMI microscopy remains the same as that of a wide field microscopy), but allows to measure the axial distances of fluorescent objects with a precision down to the 1 nm range and the sizes (axial extension) of the fluorescent object with a diameter ranging from about 40 to 200 nm with an accuracy between 5 to 10% [128, 129].

The spatially modulated illumination microscope is a wide field epifluorescence microscope with structured illumination in the axial direction (Figure 5.5). The key feature is that the two counter-propagating excitation laser beams form an interference pattern with a $\cos^2$ form along the optical (z) axis which modulates the illumination of fluorescent objects [131, 132, 133, 134, 135]. The object is moved axially in precise, small steps through the illumination pattern and the microscope focus. The images acquired at each step with the CCD camera results in 3D image stacks with a PSF corresponding to the multiplication of a normal wide field PSF and the SMI standing wave pattern.

The SMI point spread function is characterized by a modulation along the optical axis, which will be blurred out by the object being measured, with the modulation highly visible for very small objects and completely missing for objects larger than approximately 140nm. The relationship of this blurring of the modulation and the object size can be quantified, which forms the basis of SMI size measurement. In order to carry out this quantification, an intensity profile is taken through the images along the optical axis, the so called AID (axial intensity distribution). The inner and outer envelope of the AID can be automatically fitted and the ratio between them is called the modulation contrast (R), see Figure 5.6. Thus a modulation contrast 0 corresponds to the case of an infinitely small object and 1 to a large object where no modulation is visible. To avoid some certain confusion, the term modulation depth (r) is introduced[137], which has a relationship $r = 1 - R$ with the modulation contrast.

Given an object form, it is possible to calculate the relationship between modulation depth and object size by calculating the convolution between the equation for the axial projection of the object and that for an axial profile through the PSF. These calculations have been described in detail in previous Ph.D. thesis [138]. The result of such a calculation for a spherical object is shown in Figure 5.7.

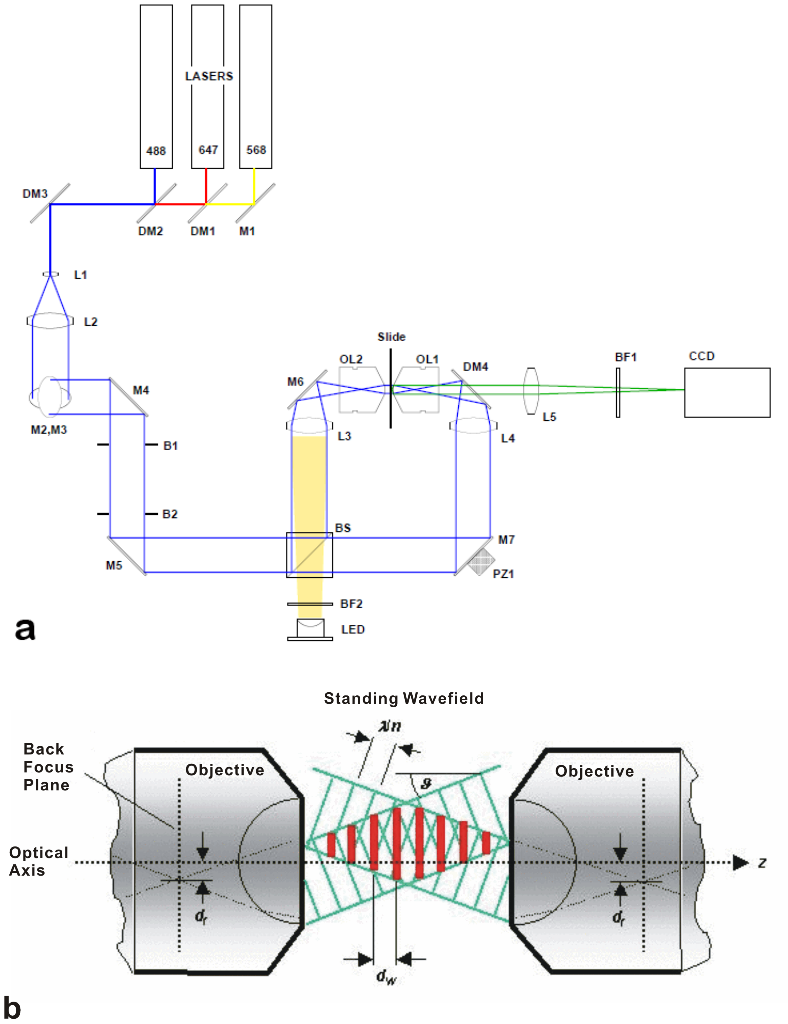

Figure 5.5. **Experimental setup of the SMI microscope. (a)** The sample is positioned between the two objectives (OL1, OL2) using a 3-axis (x,y,z) stepper motor stage for coarse movements and a 2-axis (y,z) piezo stage for fine control and object scanning. The fluorescence from the sample is collected by the right hand objective (OL1) and imaged on the CCD camera. [130] **(b)** Two laser beams propagate in opposite directions and interfere in the optical axial direction between the two opposing objectives, creating a standing wave field with intensity modulation along the optical axis.

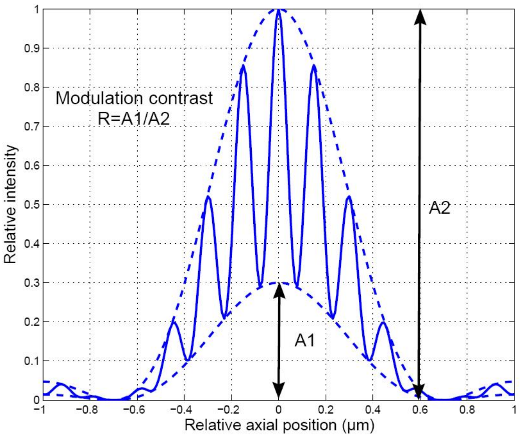

Figure 5.6. **Scheme of the extraction of the modulation contrast R.** The modulation contrast R is equal to the ratio of the amplitude of the inner and outer envelope (dashed line) of the AID (solid line), from which the axial object size can be calculated. [136]

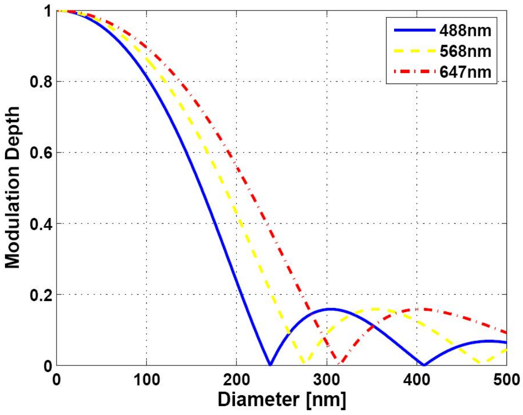

Figure 5.7. **Relationship between object diameter and modulation depth for a spherical object.** This simulation assums a refractive index of 1.47, complete interference and an angle of 0° between the two laser beams. The modulation depth decreases monotonically with increasing object size up to around 240nm, after which a low amplitude ringing is seen. In the region from 40nm to around 200nm, this relationship is one to one and can be inverted to obtain a mapping from measured object modulation depth to object size. [137]

Chapter 6

Stereology Methods

Since what we are interested are the features of the cell nucleus as a three dimensional (3D) object and what we have are the measurements made with the two dimensional (2D) cryosections of the nucleus, the one problem which we need to deal with is how to extract quantitative information about a 3D material from measurements made on 2D planar sections of the material, which is exactly what stereology methods are developed for.

6.1. Introduction to Stereology Methods

Stereology is the science of the geometrical relationships between a structure that exists in three dimensions and the images of that structure that are fundamentally two-dimensional (2D). It was initially developed to deal with quantification problems of electron-micrographs (Weibel 1979) and today its most intensive use is still in conjunction with microscope images, including light microscopes (conventional and confocal), electron microscopes and other types. For biological specimens, as long as the section thickness is much thinner than any characteristic dimension of the structure being examined, it is convenient to treat these images as ideal sections (i.e., infinitely thin).

The basic elements of a 3D structure are three-dimensional volume, two-dimensional surfaces, one-dimensional surfaces intersections and edges, zero-dimensional features which are basically points in space. When a probe section intersects these 3D features, the resulted image will show traces of those features that are reduced in dimension by one (Figure 6.1). That is, volumes (three-dimensional) are revealed by areas, surfaces (two-dimensional) by lines, curves (one-dimensional) by points, and points are not seen if the section plane does not hit them.

6.2. Fundamental Equations of Stereology

The geometric properties of a 3D structure, which include volume, surface area, line length and curvature, in most cases are measured on a sample of the entire specimen and are expressed as "per unit volume" of the structure. Letters V, S, L, and M are employed to respresent volume, surface area, length, and curvature, respectively. Since they are measured with respect to volume, we get

$\mathbf{V}_V$ the volume fraction (volume per unit volume, a dimensionless ratio) of a phase (the general stereological term used for any identifiable region or class of objects, including voids)

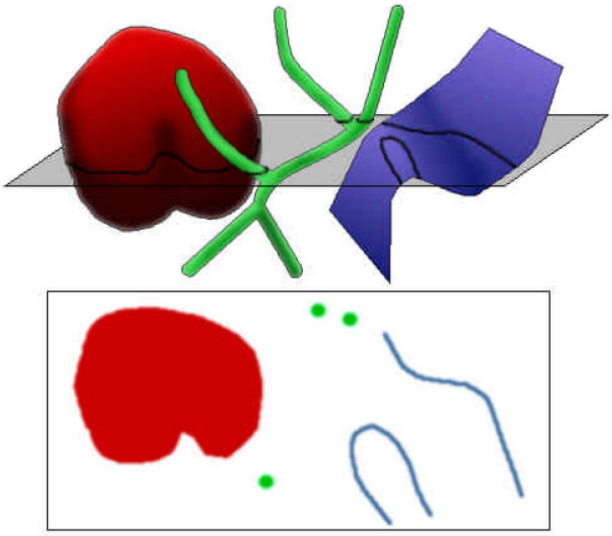

Figure 6.1. **Sectioning features in a three dimensional space with a place.** The area intersection with a volume (red), the line intersection with a surface (blue) and the point intersection with a linear feature (green) are shown. [106]

S$_V$ the specific surface area (area per unit volume, with units of m^{-1}) of a surface

L$_V$ the specific line length (length per unit volume, with units of m^{-2}) of a curve or line structure

M$_V$ the specific curvature of surfaces (with units of m^{-2})

Measurements on an image are reported as "per unit area" and have a subscript A, so we can have

A$_A$ the area fraction (dimensionless)

L$_A$ the length of lines per unit area (units of m^{-1})

P$_A$ the number of points per unit area (units of m^{-2})

Likewise if we measure the occurrence of events along a line the subscript L is used, giving

L$_L$ the length fraction (dimensionless)

P$_L$**(or** N$_L$) the number of points per unit length (units of m^{-1})

And if we place a grid of points on the image and count the number of points that fall on a structure of interest relative to the total number of points, that would be reported as

P$_P$ the point fraction (dimensionless)

The 3D microstructure of a specimen is measured by sampling it with probes. The most common stereological probes are points, lines, surfaces and volumes (Table 6.1). The fundamental relationships connect the various measures obtained with different probes with the structural parameters, and they follow the expected value (denoted by $< >$) theorems, which means that the equations apply to the average value of the population of probes in the 3D space. (Table 6.2) All of these relationships are based on the need to sample the structure to obtain a mean value, and the sampling must be IUR - isotropic, uniform and random.

Table 6.1. Interaction of probes with feature sets to produce events. [106]

3D Feature	Probe	Events	Measurement
Volume	Volume	Ends	Count
Volume	Plane	Cross-section	Area
Volume	Line	Chord intercept	Length
Volume	Point	Point intersection	Count
Surface	Plane	Line trace	Length
Surface	Line	Point intersection	Count
Line	Plane	Intersection points	Count

Table 6.2. Fundamental equations of stereology. [106]

Measurement	Relation	Property
Point count	$< P_P >= V_V$	Volume fraction
Line intercept count	$< P_L >= S_V/2$	Surface area density
Area point count	$< P_A >= L_V/2$	Length density
Feature count	$< N_A >= M_V/2\pi = N_V \cdot < D >$	Total curvature
Area tangent count	$< T_A >= M_V/\pi$	Total curvature
Disector count	$< N_V >= N_V$	Number density
Line fraction	$< L_V >= V_V$	Volume fraction
Area fraction	$< A_A >= V_V$	Volume fraction
Length per area	$< L_A >= (\pi/4) \cdot S_V$	Surface area density

The expected value relationships of stereology are powerful because they require no assumptions about the geometry of the features being examined, as long as the probes are appropriately designed. The fields to be characterized in a sample are examined by overlaying an appropriate grid containing the probes (Figure 6.2). Interactions of the probes with features of interest in the sample are noted and counted. The mean of these counts is then computed and normalized, which gives the expected value of the population mean for the full set of probes. This result is inserted in the corresponding fundamental relationship to yield an estimate of the geometric property for the three dimensional structure. The standard deviation of the sample measurements is used to calculate the precision of the estimate.

6.3. Ground Rules for Sample Design

Although the fundamental relationships require no geometric assumptions because the probe sense specific geometric properties directly, regardless of how the features are arrayed in the structure, the sample design has to obey some ground rules to ensure that the sample mean is an unbiased estimate of the expected value of the entire probe population. The primary requirements for an unbiased estimation are the "**IUR**" rules.

Isotropic	Probes with directions, like lines and planes, their orientations must be uniformly distributed over the sphere of orientations in three dimensional space, that is, isotropically distributed.

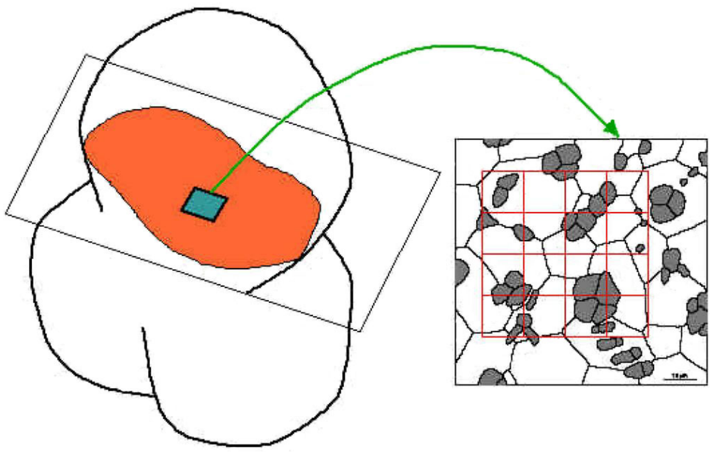

Figure 6.2. **Probe construction.** A grid of lines is superimposed on a plane section through the microstructure, and the interactions of the probes with features of interest in the sample will be noted and counted. [106]

Uniform	The fundamental relationships assume that the elements of the probe population are uniformly distributed in space. If the structures being probed are uniformly distributed in space and isotropic in orientation, then any set of sample probes can be used.
Random	For statistical purposes it is required that sample probes are selected randomly from these uniform distributions, because this simplifies the statistical interpretation of the result.

6.4. Why the Fundamental Equations Work

Though with the very simple form, stereology equations are able to characterize features in three dimensional sample without making geometric assumptions. How can it be so simple yet so powerful? This question goes to the core of stereology.

Since we are going to use point counts to sense the volume fraction in this work, here we will only look in detail of this fundamental equation

$$< P_P >= V_V$$

where V_V is the volume fraction occupied by the phase being counted and the brackets around $< P_P >$ signify the expected value for this normalized count, in this case the point fraction. This equation may be read as "The expected value of the fraction of the population of points that exist in the volume of the structure under study that lie in the phase of interest is equal to the fraction of the volume of the structure occupied by that phase."

Consider the population of points in three dimensional space. In a two phase $\alpha + \beta$ structure, this population of points fills the volumes occupied by the α and β phases. If points are uniformly distributed in space, the number of points in the α part of the structure is proportional to the volume of the α part. The number of points in the total specimen is proportional to the

Figure 6.3. **Different size circles can be generated by sectioning of a sphere.** [106]

total volume of the specimen. The volume fraction of the α phase can be considered as the ratio of the number of points in the α phase to the number of points in the total specimen, which is what the equation says. If a sample of points is drawn uniformly and randomly from this population, then the fraction of points in α phase in this sample will estimate the fraction of points in the population, which in the equation is shown to be equal to the volume fraction of the α phase in the structure.

A more detailed explanation and also deductions of the other equations can be find in [106].

6.5. The Sequential Subtraction Method

When using a plane to probe a sphere object, a series of circles of different sizes can be generated (Figure 6.3). If the sphere object is not with one given size, but has a size fluctuation, which is the case in this work, then only the equatorial section can represent the true size of the sphere object. The sequential subtraction method has been introduced by Weibel (Weibel, 1979) to calculate the true size distribution of spherical objects, which discards the contributions of all the polar sections from the whole section size distribution, leaving only the equatorial sections to represent the true sizes. In this method, the largest section of all is considered as the equatorial section of the largest object. The frequency of polar sections which are generated from random sectioning of this object can be calculated from this equation

$$f[r_i, r_{i+1}] = \frac{z_{i+1} - z_i}{R} = \frac{\sqrt{R^2 - r_{i+1}^2} - \sqrt{R^2 - r_i^2}}{R}$$

where $f[r_i, r_{i+1}]$ is the happening frequency of a give section size whose radius falls into $[r_i, r_{i+1}]$, which is equal to the ratio of the vertical distance of the two sections (with radius $r_i$and r_{i+1}), $z_{i+1} - z_i$, and the sphere radius R. (Figure 6.4)

The polar sections generated from the largest object are then calculated and subtracted from the whole population. The next size category therefore consists no polar sections generated from the last size category. This procedure is then repeated for the other size categories until only equatorial sections are left, which represents the true size distribution of the object.

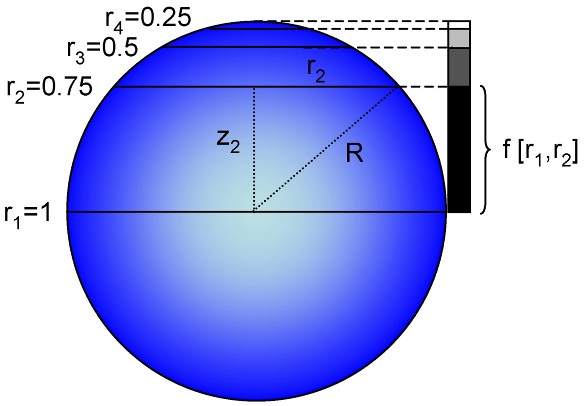

Figure 6.4. **Schematic show of how to obtain the frequency (f) of sections whose radius falls into $[r_i, r_{i+1}]$ in a sphere with radius R.** [107]

Chapter 7

Statistics

Since the fundamental relationships of stereology are based on the expected value theorem, the following statistical interpretation of the experimental data becomes an important step in the whole analysing process. When a sample of a population is studied, the data collected can be subjected statistical analysis for two related purposes: description and inference. Descriptive statistics can be used to summarize the data, either numerically or graphically, to describe the sample. For continuous data that includes mean, median and standard deviation, for example. Inferential statistics is used to model patterns in the data, accounting for randomness and drawing inferences about the larger population. Hypothesis testing, correlation and regression tests for example all belong to this category.

7.1. The Mean, Median and Standard Deviation

The mean value is the sum of all the measurements divided by the number of measurements, also known as the average. It is the simplest way to reduce all of the data to a single value for representation or comparison. Whether or not the mean value can reflect the “true” value of the data set depends on the shape of the distribution. Two other parameters are also commonly used to describe a histogram distribution in a single quantity - the median and the mode. The median is the value that lies in the middle of the distribution, therefore at most half the population have values less than the median and at most half have values greater than the median. The mode is simply the value that is most frequently observed. For a symmetrical Gaussian distribution, the mean, median and mode are identical.

Any variable that is the sum of a large number of independent factors is likely to be normally distributed. The distribution can be called normal distribution or Gaussian distribution, which describes data that clusters around a mean value and is bell-shaped with a peak at the mean. The theoretical background of this is called the central limit theorem (CLT). It states that whenever there are a very large number of independent random variables, each producing fluctuations in the measured result, then regardless of what the shape of each individual distribution may be, the effect of adding them all together is to produce an approximately overall Gaussian distribution.

The probability density function, which describes the density of probability at each point in the sample space, for a Gaussian distribution is given by the formula

$$p(x) = \frac{1}{\sigma\sqrt{2\pi}} \exp\left(-\frac{(x-\mu)^2}{2\sigma^2}\right)$$

where μ is the mean, σ is the standard deviation (a measure of the "width" of the bell), and exp denotes the exponential function.

Standard deviation is a measure of the variability or dispersion of a probability distribution. It is defined as the square root of the mean value of the square of the difference between each value and the mean (hence the name "root-mean-square" or rms difference). Another measure of the distribution width is the variance, which is just the square of the standard deviation.

It needs to be noticed that there is a difference between the standard deviation of the data sample (σ) and the standard error of the calculated mean value μ. The calculated mean value which is calculated from the data sampled from a larger population is also an estimate of the true value of the entire population. How well the calculated mean value estimates that of the population depends on how many data points have been taken. The standard error of the mean is just $\sigma/\sqrt{N}$ where σ is the calculated standard deviation of the sample and N is the number of data points used.

7.2. Student's *t*-test and ANOVA Test

When there are two (or more) sets of measurements, one important question is if they are statistically different or they are actually drawn from the same population with the differences arising by chance due to sampling. Student's *t*-test (Gossett, 1908) can solve this problem when the data are normally distributed. The *t*-test compares the actual difference between two means in relation to the variation in the data (expressed as the standard deviation).

Most t test statistics have the form $T = Z/s$, where Z and s are functions of the data. Typically, Z is designed to be sensitive to the alternative hypothesis, whereas s is a scaling parameter that allows the distribution of T to be determined. For example, in the one-sample *t*-test Z is $\sqrt{n}\bar{X}/\sigma$, where $\bar{X}$ is the sample mean of the data, n is the sample size, and σ is the population standard deviation of the data; s is $\hat{\sigma}/\sigma$, where $\hat{\sigma}$ is the sample standard deviation.

The following assumptions need to be met in a *t*-test:

- Z follows a standard normal distribution
- ps^2 follows a chi-square distribution with p degrees of freedom under the null hypothesis, where p is a positive constant
- Z and s are independent

Different expressions can be used for various *t*-tests. Each of these statistics can be used to carry out either a one-tailed test or a two-tailed test, and also the appropriate degrees of freedom is given. Once a t value is determined, a *p*-value can be found according to the table of values from Student's t-distribution. If the calculated *p*-value is below the threshold chosen for statistical significance (usually the 0.10, the 0.05, or 0.01 level), then the null hypothesis will be rejected.

Analysis of variance (ANOVA) test generalizes Student's two-sample t-test to more than two groups, still making the assumption that each of the groups has a normal data distribution. ANOVA gives a statistical test of whether the means of several groups are all equal, in terms of their number of observations and variances. For the case of two groups, it is identical to t-test and their relation is given by $F = t^2$.

To perform the ANOVA test, the following sums-of-squares (SS) terms are calculated from the observations y_{ij} (i =class, j =observation number). y_i^* is the mean of observations in class i, and y_{mean} is the global average. There are n_i observations in each class, k total classes, and t total observations.

- SST (total sum of squares of differences) $=\sum\sum(y_{ij} - y_{mean})^2$
- SSA (sum of squares of difference within the classes) $=\sum\sum(y_i^* - y_{mean})^2 = \sum n_i \cdot (y_i^* - y_{mean})^2$
- SSE (difference between the total variation and that within classes) = SST - SSA

Then an F value is calculated as $F = (SSA/n_1)/(SSE/n_2)$, where the degrees of freedom are $n_1 = k - 1$ and $n_2 = t - k$ [106]. The calculated F value is compared with the corresponding critical values form, if the F value is less than the critical values, then the difference between the groups is not significant at the corresponding level of probability.

7.3. Kolmogorov-Smirnov Test

The t-test and ANOVA test mentioned before both rely on the assumption that the data are normally distributed, since only then the mean and the standard deviation can fully describe the data. For the other cases, nonparametric tests are introduced, which do not make assumption of normality and do not use "parameters" such as mean and standard deviation to characterize the data. The Kolmogorov-Smirnov test (K-S test) is such a kind of nonparametric test that uses cumulative plots of variables and compares these plots for two data sets to find the largest difference. The cumulative distribution plot shows the percentage of observations that have a value at least as great as the value along the axis. Since the percentage rather than the actual number of observations is used, it is then possible to compare distributions with different numbers of measurements.

When the Kolmogorov-Smirnov test is used to test whether the distributions of two samples differ, the statistic is

$$D_{n_1,n_2} = \underset{x}{sup}|F_{n_1}(x) - F_{n_2}(x)|$$

where the sup S is the supremum of set S.

The null hypothesis, that the samples are drawn from the same distribution, is rejected at level α if

$$\sqrt{\frac{n_1 \cdot n_2}{n_1 + n_2}} D_{n_1,n_2} > K_\alpha$$

where K_α is found from $Pr(K \leq K_\alpha) = 1 - \alpha$.

Nonparametric tests can also be applied to normally distributed data as well as to any other data set, though in these cases they are not as efficient at providing answers of a given confidence level as parametric tests. However, unless a data set is known to be Gaussian in distribution, it is generally safer to use nonparametric tests to avoid erroneous results. [108]

Part II

Results and Discussion

Chapter 8

Mouse Mammary Tissue Cryosections

Traditionally used paraffin-embedded tissue sections in chromosome organisation research have several drawbacks. First, they normally need to go through a de-waxing and a rehydration step before the fluorescence *in situ* hybridisation to retrieve the original sections. Second, these sections are usually several micrometers thick, so before hybridisation harsh protein digestion is required to allow the probes to penetrate into the nuclei. All these treatments affect the preservation of the nuclear morphology and disturb investigation of the genome organisation.

Using thin cryosections, these problems can be solved. The mouse mammary tissue cryosections used in this work are 200 nm in thickness, which allows direct probe accessibility. Therefore no harsh protein digestion was used before hybridisation except for 0.1 M HCl for 10 min, which caused less damage to the nuclear morphology and preserved the nuclear ultrastructure. After cutting, the tissue sections were captured in sucrose drops which is 2.1 M sucrose in phosphate-buffered saline (PBS) and transferred to a glass coverslip. The sucrose can be washed away prior to fluorescence *in situ* hybridisation simply by rinsing in PBS, yielding a thin section of fixed material that is not hindered by paraffin, and has not been subjected to detergents, organic solvents, drying or high temperatures, all of which can induce distortion of nuclear structure.

The resolution is also enhanced due to sectioning. Figure 8.1 shows an example of nucleus staining in mammary gland tissue sections. The nuclei are all stained with DAPI. (a) is part of a paraformaldehyde (PFA) fixed paraffin embedded mouse mammary gland tissue section; (b) is part of a PFA fixed thin cryosection from the normal mammary gland of the transgenic mouse which has been through 5 rounds of pregnancy and lactation. The basic features of genome organisation (nuclear envelope, heterochromatin, euchromatin, chromocenters) can be clearly recognized in the cryosection (b), whereas it is all blurred in the paraffin-embedded section (a). Zooming in to the single cells, the ones in the cryosection (d) show clearly the nuclear structure and in the case of paraffin-embedded section (c) the cells can hardly be recognised. From Figure (d), one can see the chromatin is not evenly distributed in the nucleus. The tightly packed heterochromatin is intensely stained and gathers mainly at the periphery of the nucleus. The less compacted euchromatin stains lighter and occupies the rest of the nuclear space. The bright points are densely stained chromatin called chromocenters, which are aggregation of heterochromatin containing telomeric DNA and telomerase activity [140, 141].

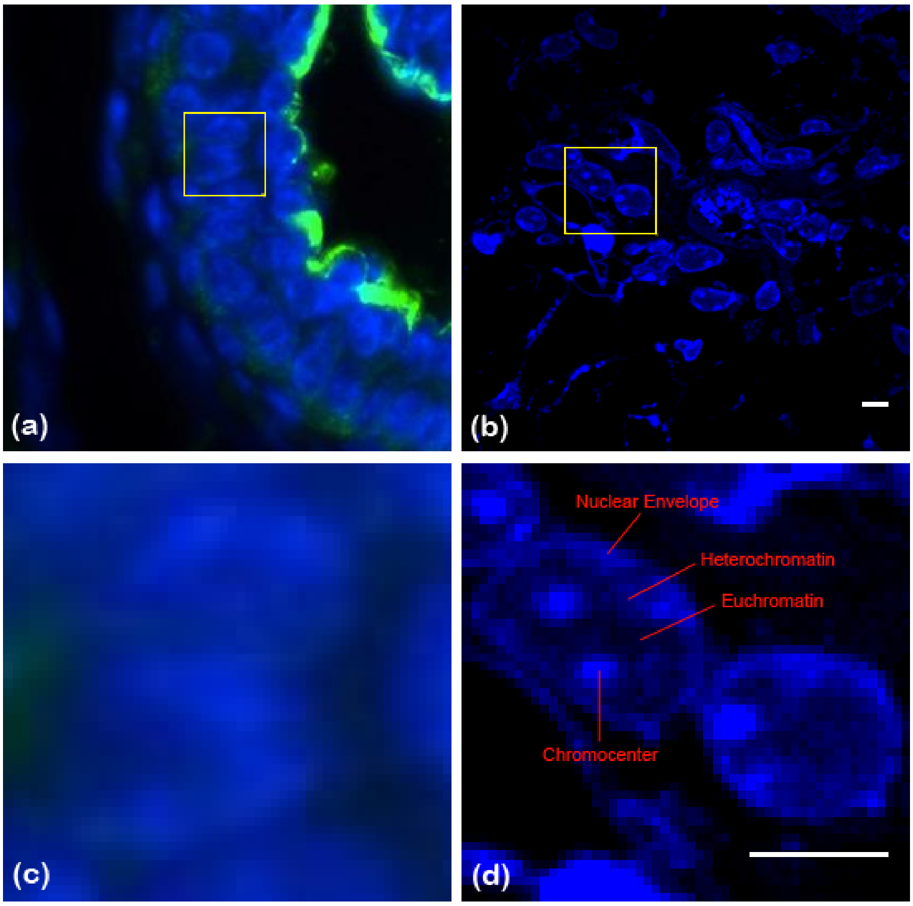

Figure 8.1. **Nucleus staining (DAPI) of mouse mammary gland tissue sections**. **(a)** Part of a paraformaldehyde (PFA) fixed paraffin embedded mouse mammary gland tissue section. The image is from [139]; **(b)** Part of a PFA fixed thin cryosection (200 nm in thickness) from the normal mammary gland of the transgenic mouse which has been through 5 rounds of pregnancy and lactation. The image was taken in the Nikon Imaging Center in Heidelberg with Nikon C1Si-CLEM spectral imaging confocal laser scanning system, with NA1.4 60x oil immersion objective. Scale bar: 5 μm. Not only the nuclear structure was preserved using cryosections, the resolution has also been enhanced due to sectioning. The basic features of genome organisation (nuclear envelope, heterochromatin, euchromatin, chromocenters) can be clearly recognized in the cryosection (b), whereas it is all blurred in the paraffin-embedded section (a). **(c)** and **(d)** are the zooming in of the selected area in (a) and (b), respectively. From Figure (d), one can see the chromatin are not evenly distributed in the nucleus. The tightly packed heterochromatin is intensely stained and gathers mainly at the periphery of the nucleus. The less compacted euchromatin stains lighter and occupies the rest of the nuclear space. The bright points are densely stained chromatin called chromocenters, which are aggregation of heterochromatin containing telomeric DNA and telomerase activity. The scale bar in (d) is 5 μm.

Chapter 9

Nuclear Volume Measurements

Topologically, the transcriptionally active gene region can be significantly more decondensed than the inactive ones, which is reflected in the three- dimensional volume change of the fluorescently labelled gene region, as revealed by *in vivo* and *in vitro* experiments. Therefore, measuring the average nuclear volumes in the different cases during physiological changes and tumorigenesis becomes necessary, as an indication of the overall genome activity, and also the values are useful for calculating the 3D nuclear radial distribution of the chromosome. The 3D nuclear volume can be represented by the nuclear radius. In this section, the stereological method used for calculating the true nuclear radius distribution of the cell population will be demonstrated and also the biological significance as well as the precision of the results will be discussed.

Note: In the nuclear volume measurements (this chapter) and the calculation of chromosome 11 volume and nuclear radial position in Chapter 11 and Chapter 12, the same set of tissue cryosections was used for data evaluation. Three types of cryosections from the mammary gland of the transgenic mice were used to represent the whole tumorigenesis process. One is from the healthy mouse without any pregnancy and lactation, which is referred to as from "normal" mouse in the text; the second is from the normal mammary tissue of the mouse with 5 rounds of pregnancy and lactation (referred to as the "lactated" mouse), during which the oncogene has been transcribed; and the last is from the mammary tumor of the transgenic mice (referred to as "tumor"), at which state the oncogene has been activated.

9.1. Measuring the Nuclear Radii Distributions using the Sequential Subtraction Method

The cutting process of the cryosections will generate nuclear sections randomly, including polar sections and equatorial sections, when only the latter can represent the true size of the nucleus. Therefore, a method which can extract all the equatorial sections from whole population is required. Sequential subtraction method has been introduced for the exact purpose, with which the contributions of all the polar sections were discarded from the whole section size distribution, leaving only the equatorial sections to represent the true size distribution of the cell population of each tissue type. The detailed calculating process is described here, using the case of "normal" mammary gland cryosections for an example.

In the case of the cryosections from the normal mouse mammary gland, the minimum and maximum radius of the nuclear sections was observed to be $0.9\,\mu m$ and $3.6\,\mu m$, respectively. (For the whole set of data, see Appendix A.) The nuclear radii were first grouped into different size categories in this size range. How many values fell into each size category was calculated and listed in Table 9.1.

The largest size category here, $3.6\,\mu m$, was taken as the radius of the equatorial sections of the largest nuclei. For a given nucleus radius R, because of the sectioning process, the happening frequency (f) of the polar sections whose radius fall into $[r_i, r_{i+1}]$ is

$$f\left[r_i, r_{i+1}\right] = \frac{\sqrt{R^2 - r_{i+1}^2} - \sqrt{R^2 - r_i^2}}{R}$$

Therefore the happening frequencies of polar sections within the size categories listed in Table 9.1 can be calculated out. The real numbers of the polar sections derived from radius R were the section number, which is 2 here in the $3.6\,\mu m$ size category, multiplied by the fraction of the corresponding happening frequencies. Then these numbers of the polar sections were subtracted from the population, and resulted in a population free of polar sections derived from nuclei with radius $3.6\,\mu m$.

The calculating process of the equatorial sections of the second largest size category ($3.4\,\mu m$) is shown in Table 9.2. The first column is the existing nuclear section size categories of the cells from normal mouse mammary gland cryosections and the second column is the measured number of cases whose radius fell into each size category, which has already been shown in Table 9.1. The third column is the theoretical happening frequencies of polar sections within corresponding size categories, which was calculated by the above mentioned equation, where R is $3.6\,\mu m$ in this case. For example, for $f\left[r_1, r_2\right]$, r_1 is $3.6\,\mu m$, r_2 is $3.4\,\mu m$, therefore

$$f\left[r_1, r_2\right] = \frac{\sqrt{R^2 - r_2^2} - \sqrt{R^2 - r_1^2}}{R} = \frac{\sqrt{3.6^2 - 3.4^2} - \sqrt{3.6^2 - 3.6^2}}{3.6} = 0.3287$$

The other frequencies were calculated in the same way. Since the actual nuclear radius count is 2 for $R = 3.6\,\mu m$, the other frequencies were then normalized accordingly, shown in the fourth column as "Normalized Number of Cases". For example, the frequency of generating the $3.4\,\mu m$ size category polar sections was calculated to be 0.1295, as shown in the third column of Table 9.2, therefore the normalized nuclear radius count was $\frac{0.1295}{0.3287} \times 2 = 0.7877$, which means two $R = 3.6\,\mu m$ nuclei should generate 0.7877 $r = 3.4\,\mu m$ polar sections in theory. From the measurement there were five $r = 3.4\,\mu m$ nuclear profiles, as shown in the second column as "Measured Number of Cases" which was derived from Table 9.1, then the actual counts of $r = 3.4\,\mu m$ nuclei was subtracting 0.7877 from 5, which was 4.2123. The other subtracting results are listed in the last column as "Difference (Measured

Table 9.1. The measured number of cases in different size categories of the nuclear sections from “normal” mammary gland cryosections.

Nuclear Sections Size Categories (Radius, μm)	Nuclear Sections Size Ranges (Radius, μm)	Number of Cases
1.0	0.8 - 1.0	5
1.2	1.0 - 1.2	6
1.4	1.2 - 1.4	12
1.6	1.4 - 1.6	13
1.8	1.6 - 1.8	10
2.0	1.8 - 2.0	16
2.2	2.0 - 2.2	17
2.4	2.2 - 2.4	10
2.6	2.4 - 2.6	13
2.8	2.6 - 2.8	11
3.0	2.8 - 3.0	10
3.2	3.0 - 3.2	7
3.4	3.2 - 3.4	5
3.6	3.4 - 3.6	2

- Normalised)”, showing the counts of all the size categories without the affection of the polar sections generated by the 3.6 μm size category.

The same process was repeated sequentially for all the other size categories, until there was no polar sections and only the equatorial sections were left to represent the true size distribution of the nuclei. The final results are listed in Table 9.3.

The calculating processes of the nuclear radius distribution of the “lactated” and “tumor” cases will not be described in detail here, since the theory is the same with that of “normal” case discussed above. The final results of these two cases are shown in Table 9.4.

The nuclear radius distributions of the three cases are compared in Figure 9.1. The average nuclear radii in the cases of “lactated” (2.35 μm) and “tumor” (2.64 μm) are smaller than that of the “normal” case (2.67 μm), and the differences among the three size distributions are statistically significant. The distribution of the nuclear radii of the tumor cells is much wider than the other two, which indicates the loss of growth control property of tumor cells.

9.2. The Nuclear Volumes Vary at Different Physiological States of the Cells

The measured nuclear radii of the cell populations can be translated into nuclear volumes using the equation $V = 4 \cdot \pi \cdot r^3/3$, giving the nuclear volume

Table 9.2. The calculating process of the number of equatorial sections in the 3.4μm size category.

For R = 3.4 μm				
Nuclear Sections' Sizes (Radius,μm)	Measured Number of Cases	Polar Section Frequency	Normalized Number of Cases	Difference (Measured - Normalised)
1.0	5	0.0394	0.2395	4.7605
1.2	6	0.0178	0.1085	5.8915
1.4	12	0.0215	0.1310	11.8690
1.6	13	0.0255	0.1550	12.8450
1.8	10	0.0298	0.1812	9.8188
2.0	16	0.0345	0.2102	15.7898
2.2	17	0.0399	0.2430	16.7570
2.4	10	0.0462	0.2811	9.7189
2.6	13	0.0537	0.3267	12.6733
2.8	11	0.0631	0.3841	10.6159
3.0	10	0.0758	0.4611	9.5389
3.2	7	0.0946	0.5759	6.4241
3.4	5	0.1295	0.7877	4.2123
3.6	2	0.3287	2.0000	0.0000

Table 9.3. The final results of the nuclear radius distribution in the case of “normal” mammary gland cryosections.

Nuclear Radius (μm)	Counts (Equatorial Sections)	Percentage (%)
2.0	6.6524	13.5
2.2	10.1707	20.6
2.4	2.5078	5.1
2.6	6.7375	13.7
2.8	5.7800	11.7
3.0	6.4675	13.1
3.2	4.7702	9.7
3.4	4.2123	8.5
3.6	2.0000	4.1

Table 9.4. The final results of the nuclear size distribution in the “lactated” and “tumor” cases.

Lactated		
Nuclear Radius (μm)	Counts (Equatorial Sections)	Percentage (%)
1.8	5.5479	5.8
2.0	17.4194	18.1
2.2	17.6898	18.4
2.4	28.5088	29.7
2.6	11.4367	11.9
3.0	4.0000	4.2

Tumor		
Nuclear Radius (μm)	Counts (Equatorial Sections)	Percentage (%)
1.2	1.9038	1.7
1.4	5.6888	5.0
1.6	7.2008	6.3
1.8	6.3924	5.6
2.0	6.2341	5.4
2.2	11.3509	9.9
2.4	10.2371	8.9
2.6	10.2518	8.9
2.8	12.6989	11.1
3.0	13.0974	11.4
3.2	10.1780	8.9
3.4	1.5565	1.4
3.6	8.2039	7.2
3.8	2.8751	2.5
4.0	2.5378	2.2
4.4	2.0000	1.7

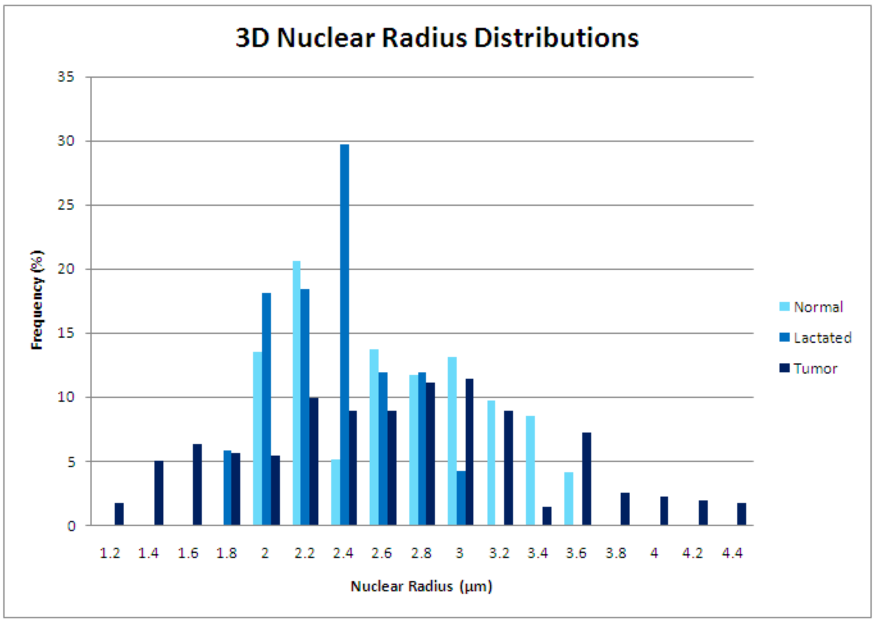

	Normal	Lactated	Tumor
Mean (μm)	2.67	2.35	2.64
Median (μm)	2.6	2.4	2.6
STD (μm)	0.49	0.31	0.77
Number of Nuclear Profiles	137	254	282
ANOVA	$p < 0.0001$		

Figure 9.1. **The 3D nuclear radius distributions and the summary of the basic statistics of the three cases.** The average nuclear radii in the cases of “lactated” and “tumor” are smaller than that of the “normal” case, and the three size distributions are statistically different. The distribution of the radii of the “tumor” case is much wider than the other two, which indicates the loss of growth control of tumor cells.

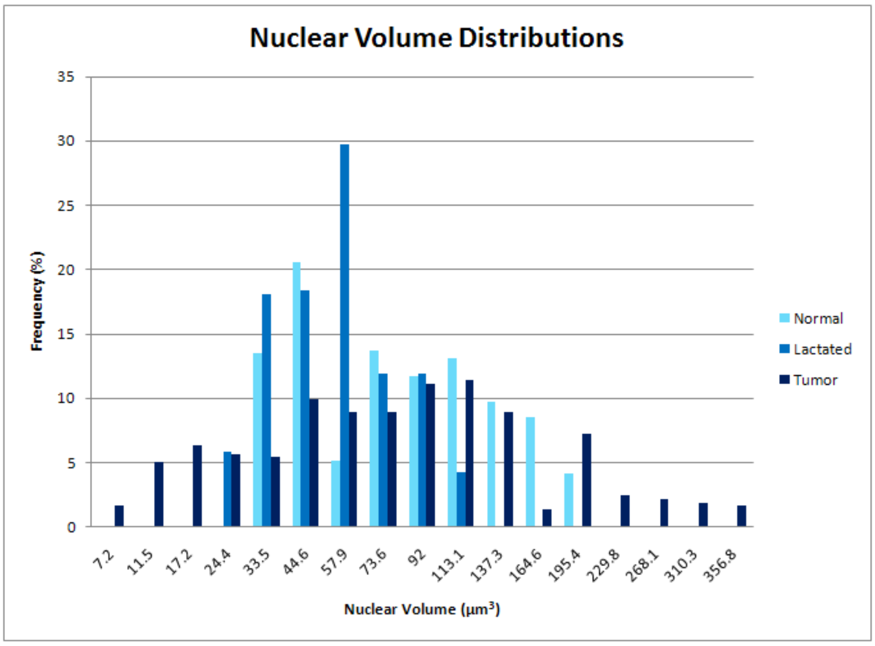

	Normal	Number of Nuclear Profiles	Lactated	Number of Nuclear Profiles	Tumor	Number of Nuclear Profiles
Nuclear Radius (μm)	2.67 ±0.49	137	2.35 ±0.31	254	2.64 ±0.77	282
Average Nuclear Volume (μm^3)	79.69	137	54.33	254	77.03	282

Figure 9.2. **The nuclear volume distributions of the three cell populations.** The table below lists the equivalent average nuclear volumes based on the average nuclear radii. The differences among the three distributions are statistically significant as revealed by ANOVA test ($p < 0.0001$).

distribution in Figure 9.2. The ranges of the nuclear volume are dynamic during the tumorigenesis process, with the “normal” case from 33.5 μm^3 to 195.4 μm^3, the “lactated” case from 24.4 μm^3 to 113.1 μm^3 and the “tumor” case from 7.2 μm^3 to 356.8 μm^3. The largest volume of the nuclei in the “tumor” case is about two-fold of that in the “normal” case and about three-fold of that in the “lactated” case, indicating the existence of actively dividing cells which have double DNA content. There are also extremely condensed nuclei in the “tumor” case, with a volume (7.2 μm^3) only about one fifth of the smallest nuclei in the “normal” case and about one third of the smallest nuclei in the “lactated” case, implicating the unique situation of malignancy.

As mentioned at the beginning of this chapter, three types of tissue sections were used in this work to represent the tumorigenesis process, referred to as from “normal”, “lactated” and “tumor” mouse. The “normal” mouse here means the mouse is a female virgin without any pregnancy and lactation, therefore the viral oncogene SV40Tag is inactive. At this time,the mammary gland has a simple tree-like structure, which is composed of the basic components called the alveoli (lined with milk-secreting cuboidal cells and surrounded by myoepithelial cells). The alveoli join up to form groups called lobules and each lobule has a lactiferous duct that drains into openings in the nipple. When the mouse with the same genotype has developed and gone through physiological changes like pregnancy and lactation, the alveoli proliferate and fill the fat pad with grape-like clusters. In this process, along with the activation of the WAP gene promoter, the oncogene SV40Tag will be actively transcribed. After lactation, changes of hormone level cause mammary involution. The elimination of differentiated mammary epithelial cells remodels the gland to a duct system similar to that of a mature virgin. At this point, the milk secretion stops and therefore the oncogene can not be transcribed, which is the case for the "lactated" mouse here.

As observed in this study, the average nuclear volume of the "lactated" case is smaller than that of the "normal" case, which can be translated into a volume difference of 32% (Figure 9.2). Since the structures of the mammary gland are similar in the two cases, the influence of geometrical constrains should be trivial. The nuclear volume difference is very likely to be caused by the expression of the SV40Tag gene product and the different physiological conditions of the cells.

In the transgenic mouse model used in this work, it was observed that after several normal pregnancies and lactations, the female mouse starts to develop papillary and then solid carcinoma, which is the case of the "tumor" mouse here. This is due to the activation of the SV40Tag gene. The early region gene product of SV40Tag, the large tumor antigen (T antigen or Tag), binds to several cellular proteins, like the tumor suppressor gene p53, the retinoblastoma suppressor gene product and DNA polymerase α-primase, which promotes DNA replication and stimulates cell proliferation. From the distributions of the nuclear volume (Figure 9.2), one can see an obvious wider distribution of the "tumor" case comparing with the other two situations, which indicates the loss of growth control property that is typical for tumor cells.

Note that instead of the tree-like ductal structure, mammary epithelial cells grow out of control and form solid carcinoma, which means in the case of "tumor" mouse, the geometrical conditions are different from the other two. The nuclear volumes range from $7.2\,\mu m^3$ to $356.8\,\mu m^3$. The nuclei whose volumes are near $356.8\,\mu m^3$ represent very likely the nuclei which have duplicated their DNA, and the extremely small nuclei whose volume are near $7.2\,\mu m^3$ indicate the existence of highly condensed nuclei, which seems to be the unique situation of malignancy. The continuously transcription of the oncogene makes the physiological conditions of the tumor cells much different from that of the normal cells. These facts make it complicate to draw a conclusion simply out of the average volume changes, and it is more reasonable to focus on the distribution pattern differences.

9.3. The Precision of the Measurements

Although in this work the cell nuclei were approximated as spherical objects, exactly speaking the actual shape of the nucleus is ellipsoid (see

Appendix B). In principle, it is possible to use plane probes to determine both the size and the shape of the object, and the result must be a statistical distribution made from a population of objects instead of a single object. However, the precondition of this method is the shape of all the objects is the same, which is usually not the case for biological specimen. As revealed by the radius ratio measurement of the nuclear sections examined in this work, the actual shape of the nucleus varies from nearly sphere to ellipsoid. In this case, theoretically a two-dimensional histogram of counts can be constructed with both area and eccentricity parameters to determine both the size and shape distributions, but this will result in a very sparse distribution of the bins which causes substantial statistical error, so practically it is not feasible. Besides, the approximation of the nuclei with different shapes of ellipsoid will also make the following chromosome radial position determination impossible due to the lack of common reference. Therefore, in this work, the cell nuclei were approximated as spherical objects which is a necessary and appropriate description with the given conditions. Especially when doing comparison between the three cases, the error caused by this approximation shall be smaller since all the three classes were calculated in the same way.

Nevertheless, with the given conditions, the average nuclear radii and volumes calculated using the sequential subtraction method are precise and can represent the true situation of the specimen. These values will be used as reference in the nuclear radial position measurements of chromosome 11.

Chapter 10

The Whole Chromosome Painting Results using Cryosections

FISH (fluorescence *in situ* hybridisation) is a cytogenetic technique that uses fluorescent labelled DNA sequences (probes) to detect specific DNA sequences which show a high degree of sequence similarity on the chromosomes. The mixture of probe sequences determines the type of feature the probe can detect. When the probe is chromosome-specific composite probe pool that hybridise along an entire chromosome, it is often refered to as "whole chromosome painting".

Whole chromosome painting allows the visualization of individual chromosomes in interphase and metaphase cells and has been widely applied in the field of clinical cytogenetics, cancer cytogenetics, comparative cytogenetics, radiation biology and nuclear topography. In this work, it is used to label the mouse chromosome 11 where the oncogene SV40 Tag is located and the images will be used to evaluate the chromosome volume and position changes during the oncogenesis process. The labelling method has been discussed in Section 4.5 and a typical result is shown in Figure 10.1. It is a part of the mammary gland cryosection from the "lactated" mouse. Chromosome 11 territories were labelled by the Cy3 conjugated chromosome 11 painting probe and the nuclei were counterstained with DAPI. Note that not all the nuclei in this plane have chromosome 11 signals but about one third of them, which is reasonable concerning the sectioning process.

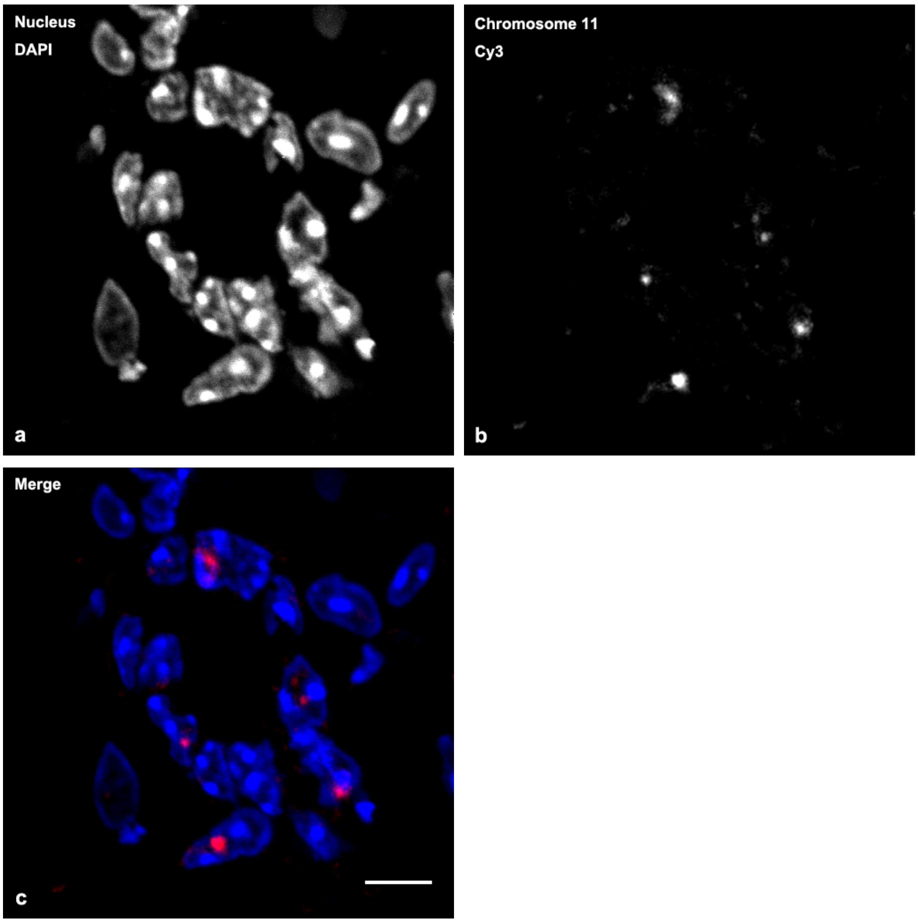

Figure 10.1. **Whole chromosome painting results of chromosome 11 with the mammary gland cryosection from the "lactated" mouse.** **(a)** The nuclei were counterstained with DAPI. The staining shows the basic chromatin organisation, which is heterochromatin gathers mainly at the periphery of the nucleus and euchromatin more at the interior of the nucleus. Chromocenters (aggregations of heterochromatin) are brightly stained. **(b)** Chromosome 11 which were labelled by the Cy3 conjugated chromosome 11 painting probe. **(c)** The merge of the two channels. Not all the nuclei in this plane have chromosome 11 signals but about one third of them, which is reasonable concerning the sectioning process. The images were taken in the Nikon Imaging Center in Heidelberg with Nikon C1Si-CLEM spectral imaging confocal laser scanning system, with NA1.4 60x oil immersion objective. Scale bar: $5\,\mu m$.

Chapter 11

Chromosome 11 Volume Measurements

In traditional stereological methods, grids with points or lines probes are used to sample an image. Counting the interactions of the probes with particular structures (usually called "phase" in the context of stereology) in the image provides the raw data for analysis. The volume fraction of a phase is estimated by the number of grid points that hit the phase divided by the total number of points in the grid. If the volume fraction of one structure within another is desired, that can be calculated out from the ratio of the number of points in the inner structure divided by the sum of these points and those which lie within the outer structure. That means, in the situation of this work, the volume fraction of a nucleus occupied by chromosome 11 can be measured by marking points within chromosome 11 (N_1) in one colour, and points within the nucleus but outside chromosome 11 (N_2) in a second colour. Then the volume fraction of the nucleus occupied by chromosome 11 is $N_1/(N_1 + N_2)$.

An unbiased estimation in a stereological measurement requires the selection of probes from the probe population to be ***I***sotropic, ***U***niform and ***R***andom (the "***IUR***" rules). In the measurement of volume fraction, the grid need to be randomly placed with respect to the features in the structure. When the structure itself and the acquisition of the image are random, this criterion is fulfilled by a regular grid of points.

Actually with a digitized image, instead of overlaying a grid of points, it is more practical to directly counting the pixels. For an array of square pixels that are either black (features) or white (background), the procedure is to count the pixels and use that as a measurement of area. Here the basic stereological rule $V_V = P_P$ is equal to $V_V = A_A$. The fraction of all the pixels in the image that are black must measure the area fraction of the selected phase and therefore the volume fraction of this phase.

11.1. Converting the Grey Scale Image to Binary Image

Counting process of the "points-phase interaction" can be directly carried out by combining the grid with the image. To do this, a segmentation process is usually necessary, which is converting the grey scale or colour image to a binary or black and white image. A straightforward method is the histogram-based thresholding, that is selecting a range of grey values by setting markers on the histogram and treating any pixel whose value lies within that range as foreground, and vice versa, although not a lot of images in

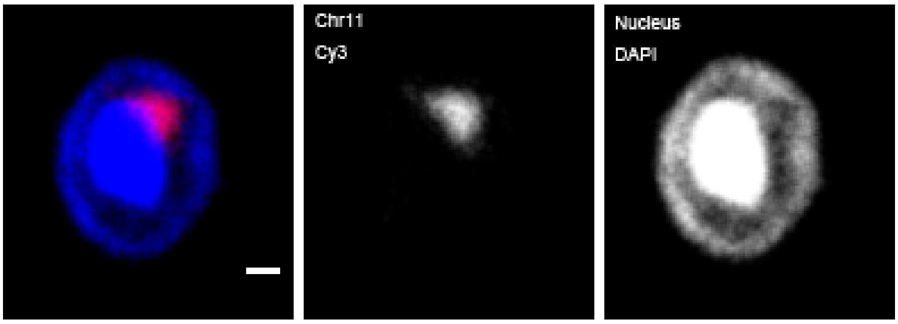

Figure 11.1. **The cell used for the demonstration of the segmentation process.** A cell from the mammary gland tissue cryosection of lactated mouse is shown here. The nucleus was counterstained with DAPI and the chromosome 11 in this section was labelled with Cy3. The images were taken in the Nikon Imaging Center in Heidelberg with Nikon C1Si-CLEM spectral imaging confocal laser scanning system, with NA1.4 60x oil immersion objective. Scale bar: 1 μm.

biology can be simply treated this way. Like in the case of this work, further image processing is required. The segmentation process will be demonstrated with the cell shown in Figure 11.1. The images have been slightly adjusted in brightness and contrast and smoothed only for demonstration purpose.

The threshold was manually defined to make sure that the entire chromosome territory was selected but not the blurring and the nuclear background (Figure 11.2, a,b). The reliability of this empirical method has been tested by Pombo and colleagues [30], which proved the variability of this method is in the same order of magnitude as the variability obtained across independent experiments. Especially in the comparison of different cases during oncogenesis in this work, the variability will be offset since all the analyses were accomplished by the author. Automatic threshold selection is not possible so far due to the various situation of every cell.

As for the thresholding for the nucleus (Figure 11.2, c), in the Matlab script described later, the binary images will be used as masks for the original images to measure the pixel numbers in every shell, therefore what is important for the segmentation is to select the nuclear boundary properly. When the same method used for chromosome territory selection was used, it usually happened that there was unselected nucleus area because of the unevenly distribution nature of the chromatin (Figure 11.2, d), which will cause error in the following calculating process. To solve this problem, an additional step was applied, which was done by “Image J - Process - Binary - Fill Holes”. The underlying algorithm is based on morphological reconstruction [142]. The “holes” are defined as sets of background pixels that cannot be reached by filling in the background from the edge of the image. 4-connected or 8-connected background neighborhood connectivity rules are normally used for two-dimensional images. The selected “hole” area which are sets of “1” values were converted to “0”s and combined with the original image, then the whole nucleus was properly thresholded (Figure 11.2, e).

After separate segmentation of the chromosome and the nucleus, the bi-

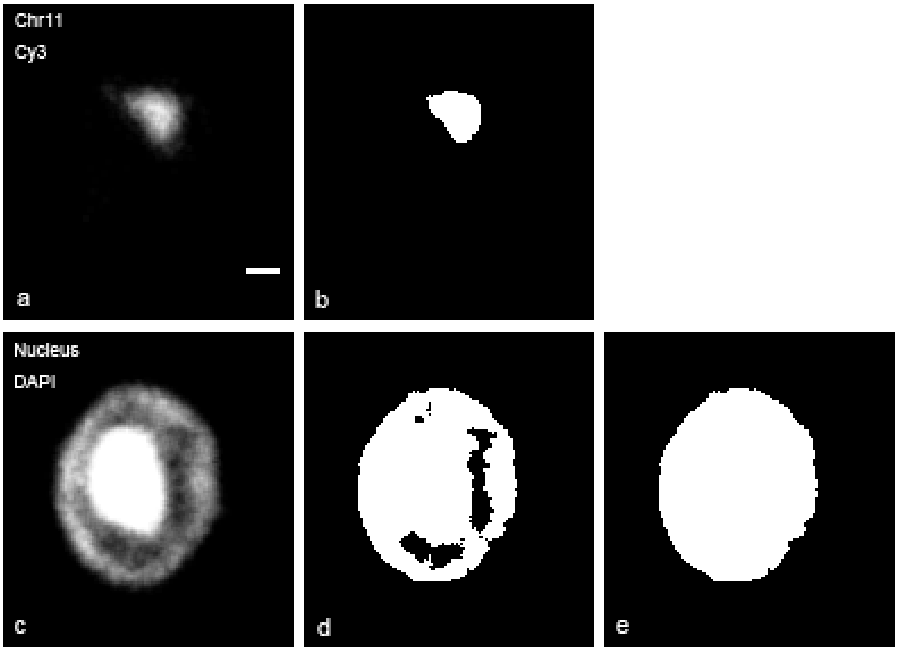

Figure 11.2. **The segmentation process of the chromosome territory and the nucleus.** The threshold value for the chromosome territory (a) was manually defined to make sure that the entire chromosome territory was selected but not the blurring and the nuclear background, which resulted in the binary image shown in b. The segmentation for the nucleus (c) was more complicated due to the unevenly distribution nature of the chromatin. The first step was to set a threshold which ensured the proper selection of the nuclear boundary (d), then an additional step was applied, which was done by “Image J - Process - Binary - Fill Holes”. The selected “hole” area which are sets of “1” values were converted to “0”s and combined with the original image by this operation, then the whole nucleus was properly converted to a binary image (e).

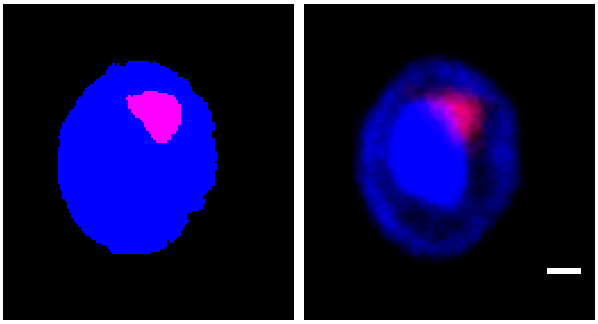

Figure 11.3. **The segmentation result.** After separate segmentation of the chromosome and the nucleus, the binary images were merged by "Image J - Image - Color - RGB Merge" to give the left image, which will be used as masks for the original image (right) in various measurements afterwards.

nary images (Figure 11.2, b and e) were merged by "Image J - Image - color - RGB Merge" to give the image in Figure 11.3 (left), which will be used as masks for the original image (Figure 11.3, right) in various measurements afterwards.

11.2. Chromosome 11 Volume Fraction Determination and Comparison

After the segmentation of the chromosome and the nucleus, the binary image was analysed with a matlab program (kindly provided by Dr. Miguel Branco, Biotechnology and Biological Sciences Research Council, UK). The program calculated parameters for both volume fraction determination and radial position calculation of the chromosome which will be discussed in the next chapter. The analysing principle was basically the same with the one developed by Dr. Johann von Hase [143], which divided the segmented nuclear space into concentric shells and evaluated the voxel intensities of CTs in each shell to get an intensity distribution of the CTs along the nuclear radius. Only here random sections of nuclei were used for analysis but not 3D nucleus, therefore an additional step to determine the axial position (z) of each section in the nucleus was included, which is $z = \sqrt{R^2 - r^2}$ with R the average 3D nuclear radius and r the radius of the section. The nucleus was divided into 10 concentric shells and the distribution of shells in each section was determined by its axial position (Figure 11.4).

For calculating the volume fraction of chromosome 11, based on the stereology principle $V_V = P_P = A_A$, the segmented images were used as masks for the original grey scale images. The pixel numbers of both the chromosome paint and the counterstain in each shell were then calculated and multiplied by the pixel size to give the area value. Since all the images were taken with the same magnification and the pixel size was the same for both channels in all the images, only the pixel numbers were recorded for calculating the ratio. The pixel numbers were summed up for all the shells and the ratio was the individual area fraction. The calculating process for the cell in Figure 11.3

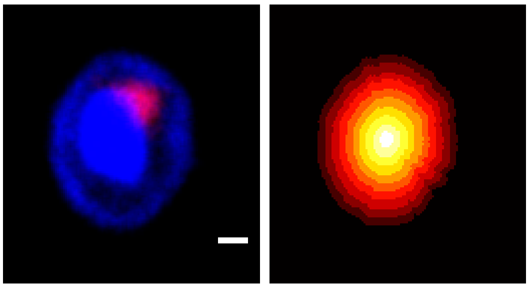

Figure 11.4. **Dividing the nuclear profile into concentric shells.** The matlab script calculated the axial position of the section and divided the nucleus into concentric shells according to it. The shape of the shells was adjusted by the shape of the original nucleus. The pixel numbers of both channels were measured and used as the base of calculation for chromosome volume and radial position.

Table 11.1. Calculating the area fraction of the chromosome in the nucleus for the cell in Figure 11.3.

Shell Number	Chromosome Pixel Numbers (per shell)	Counterstain Pixel Numbers (per shell)
10	370	4612
9	370	3751
8	370	2926
7	338	2247
6	237	1638
5	138	1156
4	43	726
3	0	408
2	0	171
1	0	43
Sum	1866	17678
Ratio	$= 1866/17678 = 0.10555$	

is listed in Table 11.1 for an example. The sum of pixel numbers of the chromosome territory is 1866 and the sum of that for the nucleus is 17678, since the pixel size is the same ($65.5\,nm$), the area fraction is equal to the point fraction which is $1866/17678 = 0.10555$, meaning the area fraction of the chromosome 11 in this individual nucleus is 10.555%.

When the area fraction calculated in Table 11.1 is for an individual cell, the average of all the individual area fractions, which is called expected area fraction A_A , can represent the expected volume fraction V_V. Taking the "lactated" cell class for example, all together 254 nuclear profiles from random sections of the same mammary gland were recorded unbiasedly, regardless of having the chromosome paint signal or not. This satisfied the "***R***andom" rule of the "***IUR***" rules. The probes, here the grids of pixels, were "***U***niformly" distributed and had no directions ("***I***sotropic") due to the nature of digital images, therefore the ground rules "***IUR***" were all satisfied.

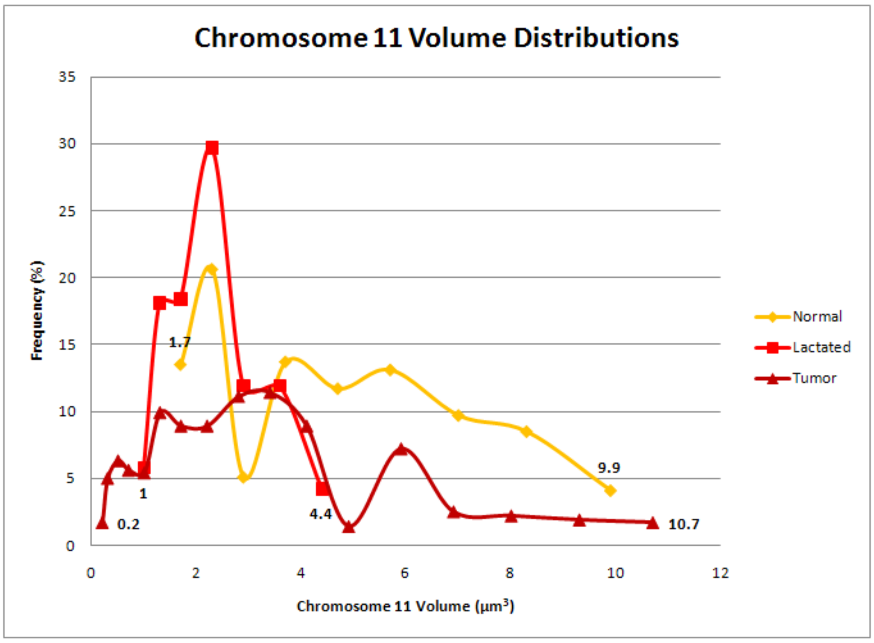

Figure 11.5. **The distributions of chromosome 11 volumes.** The exact values (volumes) at the two ends of the distributions are marked besides the data series.

Among the 254 nuclear profiles, 97 of them had chromosome paint signal and their area ratios were calculated and listed in Table 11.2. The average of these area ratios is 0.10250. Taking the whole nuclear profile population into account, the expected value of the area fraction (A_A) of the "lactated" cell class should be $(0.10250 \times 97)/254 = 0.0391$ (the area fractions for the other nuclear profiles are 0), meaning the expected volume fraction of chromosome 11 in the nucleus is 3.91%.

Using the same method, the expected volume fractions of chromosome 11 in the nucleus for the three cell classes were calculated to be 5.07% ("normal"), 3.91% ("lactated") and 3.00% ("tumor"). Taking the nuclear volumes (Figure 9.2) into account, the expected volume fractions can be translated into the absolute chromosome volumes, as summarized in Table 11.4 and Figure 11.5. The differences among the distributions of the chromosome volume are statistically significant as revealed by Kolmogorov-Smirnov test (Figure 11.6).

The genomic size of chromosome 11 is about 122 Mbp, that is 4.62% of the whole haploid genome (about 2.6 Gbp) of a cell from the female C57BL/6J mouse (see Figure 12.2). This value is diffrent from the measured volume fractions of chromosome 11 in all the three cases, which means the chromatin distribution in the nucleus is uneven.

Table 11.2. The volume fraction of chromosome 11 in the nucleus of the "lactated" cell class.

Cell Nr.	Area Ratio	Cell Nr.	Area Ratio	Cell Nr.	Area Ratio
1	0.07106	34	0.25808	67	0.06018
2	0.26212	35	0.13878	68	0.08973
3	0.16186	36	0.05191	69	0.1407
4	0.15692	37	0.08254	70	0.17008
5	0.13253	38	0.24168	71	0.11176
6	0.11015	39	0.06633	72	0.18441
7	0.07494	40	0.08677	73	0.06205
8	0.08677	41	0.18832	74	0.09155
9	0.06083	42	0.09062	75	0.02351
10	0.03844	43	0.06151	76	0.15046
11	0.10186	44	0.13001	77	0.14563
12	0.06275	45	0.02029	78	0.27828
13	0.04194	46	0.06158	79	0.1263
14	0.01289	47	0.08345	80	0.15427
15	0.07032	48	0.07462	81	0.05134
16	0.10918	49	0.10252	82	0.02447
17	0.05585	50	0.07691	83	0.1028
18	0.07825	51	0.07822	84	0.14255
19	0.11266	52	0.0709	85	0.0583
20	0.04117	53	0.1069	86	0.17128
21	0.05076	54	0.04653	87	0.25239
22	0.02361	55	0.03637	88	0.17952
23	0.14054	56	0.12845	89	0.04283
24	0.16107	57	0.17045	90	0.08797
25	0.03867	58	0.18003	91	0.06774
26	0.06468	59	0.15307	92	0.12858
27	0.08898	60	0.04102	93	0.05549
28	0.10349	61	0.06069	94	0.05442
29	0.03845	62	0.12773	95	0.13339
30	0.0498	63	0.1076	96	0.08498
31	0.11581	64	0.04075	97	0.09969
32	0.18622	65	0.02481		
33	0.20843	66	0.11322		
Expected Value of Cell Nr. 1-97 = 0.10250					
Expected Value of the Cell Population $A_A = (0.10250 \times 97)/254 = 0.0391$					
Expected Value of the Volume Fraction $V_V = A_A = 3.91\%$					

Table 11.4. Comparison of the volume fractions and the absolute volume ranges of chromosome 11 in the nucleus during tumorigenesis.

	Normal	Number of Nuclear Profiles	Lactated	Number of Nuclear Profiles	Tumor	Number of Nuclear Profiles
Chr 11 Volume Fraction	**5.07 %**	137	**3.91 %**	254	**3.00 %**	282
Chr11 Volume (μm^3)	1.7 - 9.9		1 - 4.4		0.2 - 10.7	

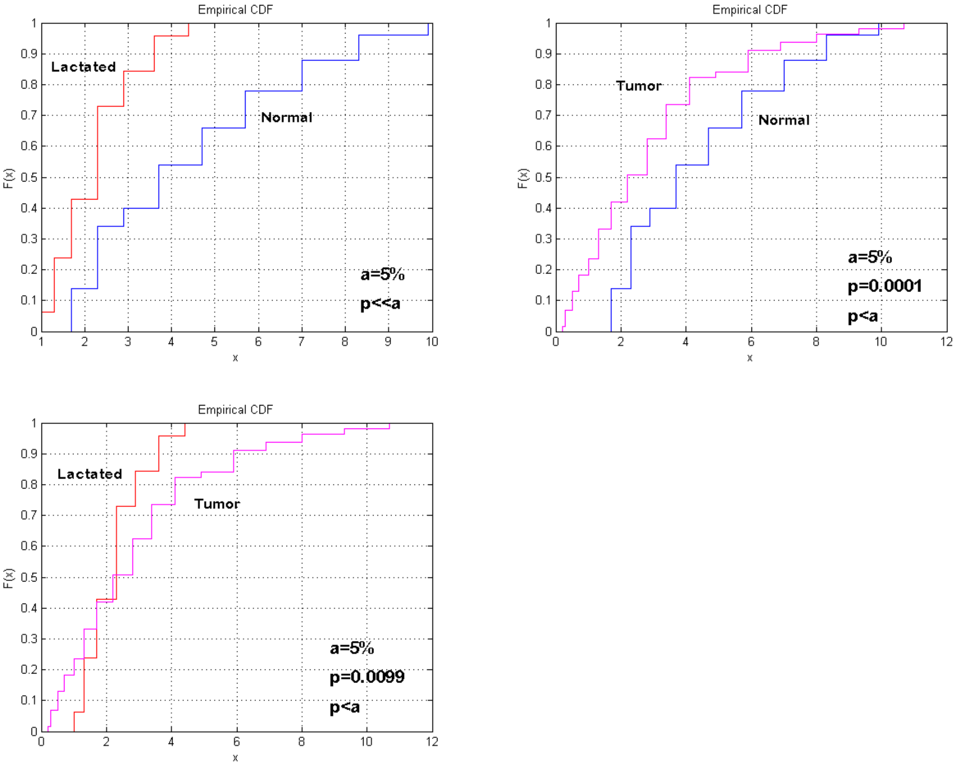

Figure 11.6. **The plots of the cumulative distribution function (CDF) for the chromosome 11 volume data in Figure 11.5.** The differences among the distributions are statistically significant at the 5% level, as revealed by Kolmogorov-Smirnov test.

11.3. The Changes of Relative Chromosome Volume Possibly Indicate Different Transcriptional Activities

The volume of chromosome 11 did not stay the same during physiological changes and tumorigenesis in this study. While the absolute volume of the chromosome ranges from $1.7\,\mu m^3$ to $9.9\,\mu m^3$ in the "normal" case, from $1.0\,\mu m^3$ to $4.4\,\mu m^3$ in the "lactated" case and from $0.2\,\mu m^3$ to $10.7\,\mu m^3$ in the "tumor" case, the relative volume fraction of the chromosome in the nucleus becomes smaller all the way from the case of "normal" mouse to that of the "tumor" mouse.

While the absolute volume of chromosome 11 is related to the nuclear volume, the relative volume fraction of it in the nucleus is directly calculated by the stereology method and therefore is an unbiased indicator of the relative volume changes of the chromosome. The volume fractions in the three cases were calculated from the original nuclear profiles using one of the basic stereology relationships $V_V = P_P = A_A$. One advantage of the stereology methods is that they make no geometric assumptions about the structure of interest, as long as the sampling process obeys the "***IUR***" rules, which is the case in this work. Together with the high resolution imaging provided by cryosections and the well nuclear ultrastructure preservation provided by cryo-FISH, the volume fractions of chromosome 11 in the nucleus calculated in this work have been the most precise measurements of this parameter in tissue sections so far.

The changes of the volume fraction indicate that the chromosome condensation state is dynamic during physiological changes and the tumorigenesis process. It has been reported long ago that the condensation state of DNA has its impact on gene expression, which was noticed by the fact that active genes are often found in less compact euchromatin and silenced genes in condensed heterochromatin [36]. Many studies have pointed out, chromosome fibre can unfold extensively [42, 51] or loop out of the chromosome territory [49] when a gene or an array of genes is activated. It is very likely that the genes on chromosome 11 had different transcriptional activities in various physiological states, which caused the relative volume changes in different states, though ideally with gene expression profiles in these conditions can better interpret the data.

The activity of the oncogene SV40Tag seems to have certain impact on the overall condensation state of the whole chromosome. The relative chromosome volume become smaller from the "normal" state to the "lactated" state, during which the SV40Tag gene has been transcribed, though the gene is inactive in both the two states; when the gene has been activated which is the case of the "tumor" mouse, the oncogene is actively transcribed and the relative chromosome volume is the smallest in the three conditions. Again, it is hard to draw a conclusion without knowing the overall gene expression profile of the chromosome, which makes it interesting to investigate the topology changes of the oncogene itself. Nevertheless, the precise measurements of the relative volumes of the chromosome provide important evidences for the chromosome condensation states during physiological changes and tumorigenesis, and will lead to a better understanding of functional genome organisation with more information.

Chapter 12

3D Nuclear Radial Positions of Chromosome 11

12.1. Analysing the Chromosome Nuclear Radial Position with the Concentric Shell Model

In former chromosome radial position study [143], the segmented nuclear space was divided into concentric shells and the voxel intensities of CTs in each shell were evaluated to get an intensity distribution of the CTs along the nuclear radius. In this work, pixel numbers in each shell of the 2D section were recorded instead of the voxel intensities, which can represent the radial position of the chromosome as well. Since random sections of nuclei were used for analysis but not 3D nucleus, an additional step to determine the axial position (z) of each section in the nucleus was included, which is $z = \sqrt{R^2 - r^2}$ with R the average 3D nuclear radius and r the radius of the section.

In this way, all together 51 nuclear profiles from the cryosections of the mammary gland of the “normal” mouse, 97 nuclear profiles from that of the “lactated” mouse and 119 nuclear profiles from that of the “tumor” mouse were analysed by the matlab script (written by Dr. Miguel Branco [107]), and the results were summarized in Table 12.1, Table 12.2 and Table 12.3, for the “normal”, “lactated” and “tumor” case, respectively. The average nuclear radius is represented by the percentage of the nuclear radius, where 0 corresponds to the nuclear centre and 100 corresponds the nuclear edge. The pixel numbers of the chromosome paint and the nuclear counterstain were summed up in each shell for all the cells in each class, and the percentage of the pixel numbers distributed along the nuclear radius was calculated as the indication of the corresponding nuclear radial position.

12.2. The Comparison of the 3D Nuclear Radial Positions of Chromosome 11

The results from Table 12.1, Table 12.2 and Table 12.3 were plotted in Figure 12.1. Although the peak values of the three chromosome distributions are slightly different, with the “normal” class at 65% (peak value 15.6%), the “lactated” class at 55% (peak value 15.6%) and the “tumor” class at 65% (peak value 16.5%), ANOVA test reveals that there is no statistically significant difference among the three distributions ($P = 0.99$), which means that the average radial position of chromosome 11 remained the same during physiological changes and tumorigenesis. Note that this is not consistent

Table 12.1. The percentage of the pixel numbers of chromosome 11 and nuclear counterstain in each shell. “Normal”.

Shell Number	Average Nuclear Radius (%)	Chromosome 11		Counterstain	
		Pixel Numbers	%	Pixel Numbers	%
1	5	471	1.3	1796	0.6
2	15	1420	4.0	5864	2.1
3	25	2417	6.9	10444	3.7
4	35	3274	9.3	14864	5.2
5	45	4737	13.5	21684	7.6
6	55	4882	13.9	28326	10.0
7	65	5482	15.6	38155	13.5
8	75	5336	15.2	45912	16.2
9	85	4495	12.8	53691	18.9
10	95	2640	7.5	62765	22.1
Sum		35154		283501	

Table 12.2. The percentage of the pixel numbers of chromosome 11 and nuclear counterstain in each shell. “Lactated”.

Shell Number	Average Nuclear Radius (%)	Chromosome 11		Counterstain	
		Pixel Numbers	%	Pixel Numbers	%
1	5	511	1.3	2390	0.6
2	15	1570	4.0	7725	1.9
3	25	2653	6.7	14041	3.5
4	35	3989	10.1	22239	5.5
5	45	5428	13.8	32775	8.1
6	55	6152	15.6	41452	10.2
7	65	6087	15.5	54533	13.4
8	75	5657	14.4	66064	16.3
9	85	4457	11.3	76050	18.8
10	95	2819	7.2	88243	21.8
Sum		39323		405512	

Table 12.3. The percentage of the pixel numbers of chromosome 11 and nuclear counterstain in each shell. “Tumor”.

Shell Number	Average Nuclear Radius (%)	Chromosome 11		Counterstain	
		Pixel Numbers	%	Pixel Numbers	%
1	5	721	1.5	6255	0.8
2	15	2063	4.2	19576	2.4
3	25	3545	7.2	33458	4.1
4	35	5128	10.4	48663	6.0
5	45	6971	14.2	67609	8.4
6	55	7630	15.5	81825	10.1
7	65	8105	16.5	105317	13.0
8	75	6870	14.0	125742	15.6
9	85	5534	11.3	147495	18.3
10	95	2570	5.2	171698	21.3
Sum		49137		807638	

with the relative chromosome volume changes, which has been smaller in this process.

This result indicates three facts: Firstly, the trancription of the oncogene during the pregnancies and lactations wasn’t accompanied by the alteration of the chromosome nuclear position, since the chromosome radial position distributions are the same in the “normal” case and the “lactated” case; Secondly, when the oncogene has been activated in the tumor cells, the nuclear position of the whole chromosome didn’t change either, which means the activation of the oncogene was possibly related to other genome structure changes if there was any; Thirdly, the relative volume fraction changes of the chromosome indicate the overall chromatin condensation changes, and the same position distributions mean that the position of the chromosome doesn’t have to change in this process.

The spatial organisation of the genome has been reported to be tissue- and cell type- specific in mouse [144]. Since all the measurements were carried out with mouse mammary gland cryosections here, and the vast majority of mammary tissue are epithelial cells, the differences of the 3D nuclear radial position of the chromosome are only correlated with the physiological states of the cells and the three situations are comparable.

12.3. Chromosome 11 Radial Positions Consist with the Gene-density Theory of Chromosome Non-random Positioning

Chromosome 11 was chosen to study the higher order genome structure, not only because the oncogene is located on it, but also because it is representative with regard to the gene density feature of the chromo-

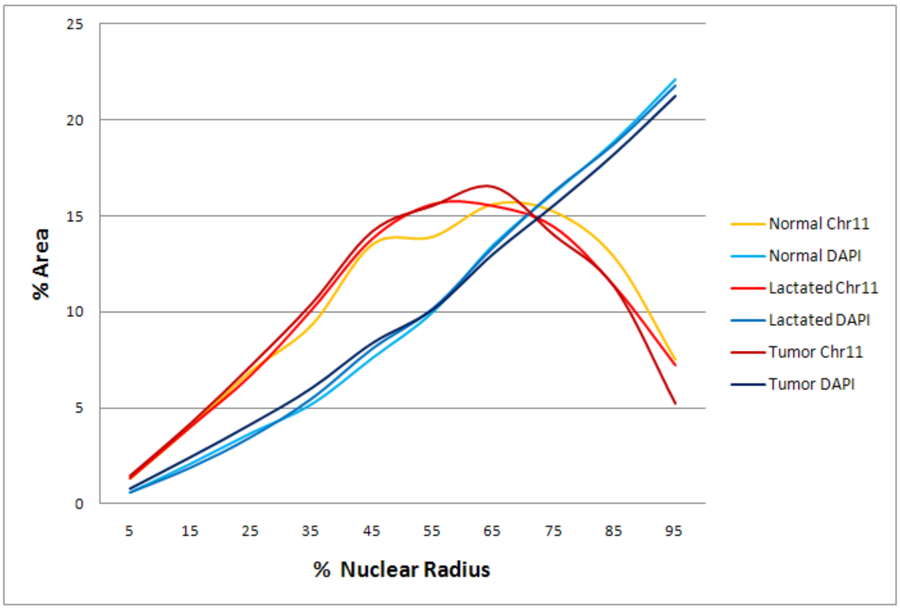

Figure 12.1. **The comparison of 3D nuclear radial positions of chromosome 11 during tumorigenesis.**

some, since it is the second most gene-dense chromosome in the mouse karyotype (17.2 $genes/Mbp$, Figure 12.2). Dietzel and colleagues analysed the radial distribution of several mouse chromosomes in different cell types using 3D-FISH [145], and the results showed that chromosome 11 located much more internally than all other chromosomes in mouse lymphocyte, fibroblast and embryonic stem cell nuclei. The results of this work showed similar distribution pattern, regardless of the physiological states of the cells, the overall radial position of chromosome 11 stayed the same and located in the interior of the cell nuclei (peak value at 55%-65% of the nuclear radius). This result was in agreement with the gene density related chromosome radial positioning theory, the same as the results from cultured cells.

The size of mouse chromosome 11 (122 Mbp) is similar to that of chromosome 9 (124 Mbp) and 14 (125 Mbp), which is comparatively small but not the smallest of the whole genome. According to the volume exclusion theory supported gene size related positioning, chromosome 11 is expected to be found in a more peripheral location than revealed in this work. However, the differences in gene density and size between mouse chromosomes are less pronounced than that of human. As summarized in Figure 12.2, for mouse chromosomes, the difference of gene density is about two fold ($9-19\,genes/Mbp$, for chromosome 18 and chromosome 7, respectively) and the difference of chromosome size is about three fold ($61-197\,Mbp$, for chromosome 19 and chromosome 1, respectively). Y chromosome was not considered in this case since all the cells were from female mice. Therefore, though the central position is in good agreement with the gene-density theory, the possibility of size dependent chromosome positioning can not be excluded only with the data of chromosome 11.

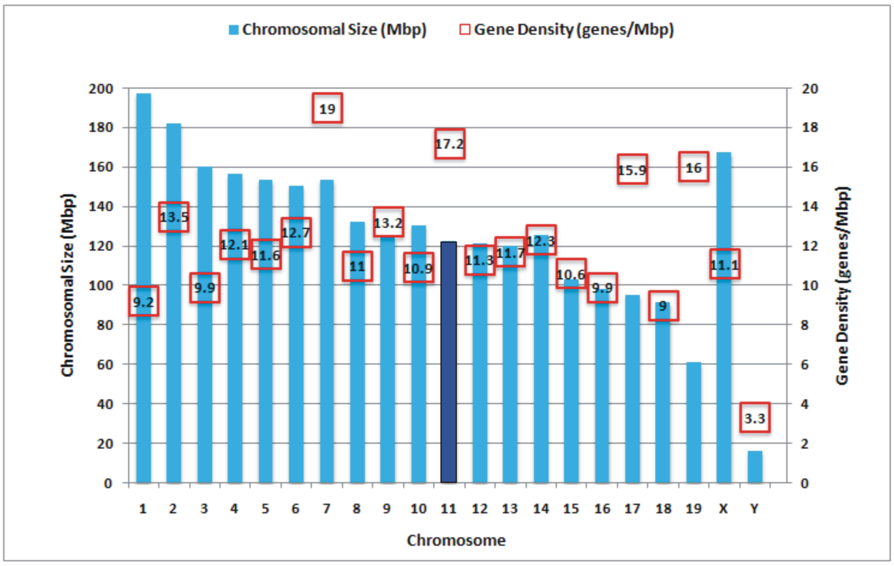

Chromosome	1	2	3	4	5	6	7
Chr. Size (Mbp)	197	182	160	156	153	150	153
Total Genes	1819	2455	1579	1881	1773	1906	2908
Gene Density (genes/Mbp)	9.2	13.5	9.9	12.1	11.6	12.7	19.0

Chromosome	8	9	10	11	12	13	14
Chr. Size (Mbp)	132	124	130	122	121	120	125
Total Genes	1446	1640	1412	2095	1371	1401	1538
Gene Density (genes/Mbp)	11.0	13.2	10.9	17.2	11.3	11.7	12.3

Chromosome	15	16	17	18	19	X	Y
Chr. Size (Mbp)	103	98	95	91	61	167	16
Total Genes	1091	973	1511	823	974	1847	53
Gene Density (genes/Mbp)	10.6	9.9	15.9	9.0	16.0	11.1	3.3

Figure 12.2. **Sizes and gene densities of mouse chromosomes.** The bars indicate the genomic sizes of the chromosomes. The distance of the square to the x-axis is scaled according to the gene density of each chromosome, with the value highlighted inside the square. The gene density is expressed as genes/Mbp. The source data are listed in the table below, which are the exact chromosome size and gene density of each chromosome of the mouse karyotype. For a diploid cell from the female C57BL/6J mouse, the total length of all the chromosomes is about 5280 Mbp, from which 4.62% is chromosome 11. The data is based on the NCBI Build 37.1 (the latest) mouse assembly (April 2007, strain C57BL/6J) [146].

Chapter 13

The Preliminary Co-hybridisation Experiments

The activity of the viral oncogene SV40Tag varies in different physiological states of the cells. The SV40Tag gene coding region is fused with the WAP gene (a milk protein encoding gene) promoter which will be transcribed during pregnancy and lactation. Therefore in virgin mouse, the oncogene is inactive and the female mouse is healthy. Then during pregnancies and lactations, the female mouse starts to produce milk, the oncogene is transcribed through the activation of the WAP gene promoter. After lactation, the milk production stops and the oncogene is not transcribed anymore. It was observed that after several normal pregnancies and lactations, the female mouse starts to developed mammary abnormalities and finally solid carcinoma. In this case, the oncogene is activated again, though the molecular mechanism is still unknown. In the mouse fibroblast cell line (C57SV) transformed with SV40 DNA, the SV40Tag gene product which transform the cells into the neoplastic phenotype was detected (image not shown). From the point of view of higher-order genome organisation, it is necessary to investigate the nuclear position changes and the condensation state changes of the SV40Tag gene in the tumorigenesis process.

Figure 13.1 shows some typical results of the preliminary co-hybridisation experiments of SV40Tag gene and chromosome 11. In the images, the nuclei are visible due to green autofluorescence. The chromosome 11 territories were labelled with Cy3-conjugated DNA probes (purchased from Cambio, UK) and the SV40Tag gene was labelled with Alexa488-conjugated probes made by nick translation. (a) is part of the mouse mammary tumor cryosection. The white arrows point out several typical nuclear profiles, including nuclei with both the chromosome painting signal and the SV40Tag gene signal (locates at the nuclear periphery), nucleus with one chromosome painting signal and nucleus with two chromosome painting signals, as shown individually in image (c) (d) and (e). The situation in image (b) is actually rare, where the two SV40Tag gene signals are on the same plane of the nuclear section.

The 3-D positioning of active and inactive genes in the nuclear space and relative to the CTs has always been an important question in the area of nuclear organisation. Though it has not come to a clear conclusion now, there are several hints about the mechanism of gene positioning.

It is well known that heterochromatic region is closely related to gene silencing [147] [148]. For example, Fisher and colleagues found repressed genes selectively localized to centromeric heterochromatin clusters in the nuclei of mouse B lymphocytes [149]. Upon transcriptional activation, gene repositioning away from the heterochromatic region has been observed. Groudine and colleagues reported that localization away from centromeric heterochro-

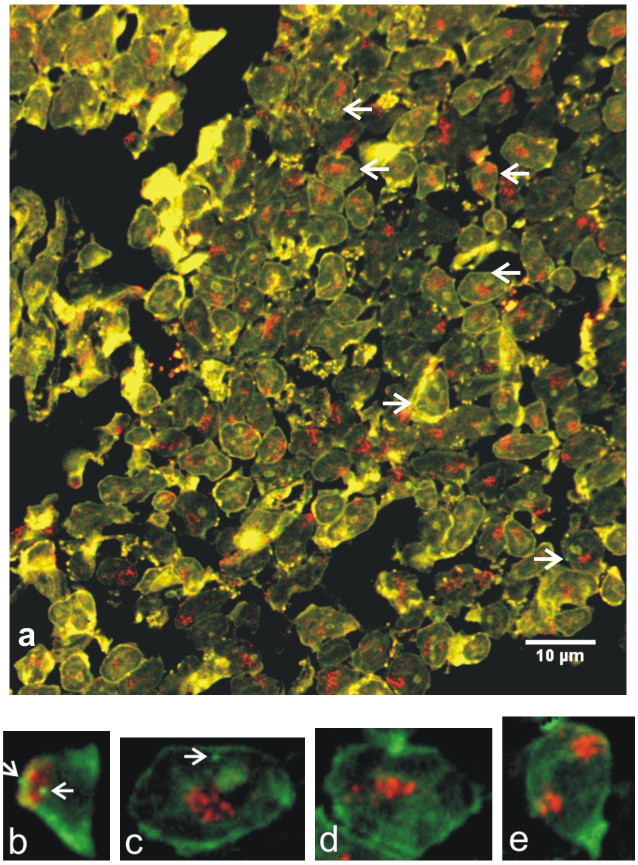

Figure 13.1. **The co-hybridisation results of SV40Tag and chromosome 11. (a)** Part of the mouse mammary tumor cryosection. The nuclei are visible due to green autofluorescence. The chromosome 11 territories were labelled with Cy3-conjugated DNA probes (purchased from Cambio, UK) and the SV40Tag gene was labelled with Alexa488-conjugated probes made by nick translation. The white arrows point out several typical nuclear profiles, including nuclei with both the chromosome painting signal and the SV40Tag gene signal which locates at the nuclear periphery, nucleus with one chromosome painting signal and nucleus with two chromosome painting signals. The image was taken in the Nikon Imaging Center at University Heidelberg, with an Nikon Eclipse 90i upright automated epifluorescence microscope, and the image has been adjusted in brightness and contrast for demonstration purpose. Scale bar: $10\,\mu m$. **(b) (c) (d) (e)** are individual nuclear profiles from the same cryosection, which shows the four typical co-hybridisation results: with the chromosome painting signal and two SV40 gene signals (arrows), with the chromosome painting signal and one SV40 gene signal which loops out of the chromosome territory (arrow), with only the chromosome painting signal (one chromosome) and with two chromosome painting signals, respectively.

matin is required to achieve general hyperacetylation and an open chromatin structure of the human beta-globin locus [150]. Belmont and colleagues found the interphase chromosome site of the viral protein VP16 moved fast and directionally from the nuclear periphery to the interior one to two hours after induced transcriptional activation in CHO cells [74]. Note that the nuclear periphery is not exclusively repressive. It can also favor the enhanced expression of certain genes at the region around the nuclear pore complex [77, 78], probably due to the result of facilitated mRNA export [79].

In this work, within the mammary tumor cryosection shown in Figure 13.1, there are about ten nuclei showed the SV40Tag gene signals (bright green), and all of them located towards the nuclear periphery but in a lightly stained area, with a typical example shown in image (c). Since the SV40Tag gene is activated when the mouse develops mammary tumor, the peripheral location of the gene loci probably is consistent with the gene activation role of the nuclear pore complex, although only the statistical results from large number of nuclear profiles in different states can really give a conclusion.

Many studies have pointed out that the regulation of gene expression on higher-order chromatin level is quite likely to be organised by large-scale [45, 46] or local [47, 48] chromatin loops, which are able to place the genome regions in distinct separate nuclear environments to optimize their activity. In a study of the *HoxB* locus upon induction of transcription reported by Bickmore and colleagues [51], locus-wide histone modification and chromatin decondensation were observed at the early stage of gene activation, then the decondensed chromatin further looped out from the chromosome territories. Similarly, the activated SV40Tag gene loci were constantly found out of the chromosome 11 territories, as shown in Figure 13.1 (c). This result may in agreement with the chromatin looping out upon transcription theory, and thinking of the peripheral location of the gene loci, this looping out might aim to favor the mRNA export.

With all the interesting results and hypothesis revealed by the preliminary co-hybridisation experiments, no statistics with the three different groups of cryosections has been made, which is due to the following difficulties: Firstly, the co-hybridisation experiment is quite time-consuming; Secondly, the results depend a lot on the type and quality of the cryosections, and it is extremely difficult with the cryosections from the normal mouse; Thirdly, the low happening frequency of the co-hybridisation signals (less than ten percent of the cell population, as roughly estimated) makes it more difficult for statistical results. Nevertheless, though not included in this work, the nuclear positions of the SV40Tag gene in different activities remains to be an interesting topic for the proceeding projects.

Chapter 14

SV40Tag Gene Size Measurements using SMI Microscopy

The Spatially Modulated Illumination (SMI) microscopy developed here in the Cremer group used structured illumination along the optical axis to modify the point spread function (PSF) of the microscope, allowing to measure the axial distances of fluorescent objects with a precision down to the 1 nm range and the sizes (axial extension) of the fluorescent object with a diameter ranging from about 40 to 200 nm with an accuracy between 5 to 10% [128, 129]. Before the sizes in this range were only measured with electron microscope (EM) because of the resolution limits of confocal microscopy are about $250\,nm$ laterally and $600\,nm$ axially. But with electron microscopy, multi-layers of antibodies labelling leads to over- or underestimation of object sizes, therefore it is not suitable for precise size measurement [151, 152]. Besides, the ability of imaging differently labelled structures in the same cell is also limited with EM.

SMI microscopy has been applied in various biological fields like analysing tiny changes of chromatin condensation [136, 153, 154] and that of functional biological nano-structures (protein-protein interaction or protein-DNA interaction) [155] in 3D fixed cells and also in live cells [156]. In this section, its application in studying specific chromatin condensation status in the area of functional genome topology will be discussed. The $2.7\,kb$ long viral oncogene SV40Tag (see Appendix C) was labelled with Alexa 568 conjugated DNA probes with fluorescent *in situ* hybridisation (FISH) method. C57SV cell line, which is a mouse fibroblast cell line transformed with SV40 DNA, was used in this experiment. The cells were fixed with methanol and acetic acid (3:1 in volume). The gene size, which corresponds to the axial extension of the labelled gene, was measured with both SMI and confocal microscopy and compared with the simulation by Virtual SMI microscopy.

14.1. Standard SMI Evaluation Procedures

The algorithm used in this work to evaluate the SMI data was developed by Dr. David Baddeley [137], aiming to automatically extract information about the object size and position from the axial profile taken through the object. Envelopes were fitted from the axial intensity distribution of the object to get the modulation contrast, and the object size, which was previously determined graphically from the modulation contrast, now has been replaced by computing a numerical solution after each fit.

An interactive data viewer is shown in Figure 14.1, where fitting can be performed by clicking on individual points. Finding objects, subsequent fitting of the axial profiles and reports generation can be done automatically by the Matlab script, with the main procedures listed as following (will be mentioned as the "*sviewer* package" in this dissertation):

`connectToDB`
Connects the computer to the SQL database on a server where parameters for the data analysis are stored.

`svlauncher`
A graphical user interphase will be displayed to load the images files.

`sviewer`
Displays the interactive data viewer shown in Figure 14.1.

`ofind3`
Locates all point like objects within an image using a multi-thresholding method. The result is the matrix `pos` containing pairs of (x, y) coordinates identifying the found points.

`dofits`
Performs the fit procedure for each of the points in `pos` resulting in a file containing the size and position information of the object.

14.2. Using Virtual SMI Microscopy to Estimate the Gene Size

Before the precise size measurement of the SV40Tag gene, it is necessary to first simulate the gene's size to control the results. What is well known about gene structure is the hierarchical folding of the chromatin [157]. As shown in Figure 14.2, the lowest level of organisation is that bare DNA strand (whose diameter is about $2\,nm$) winds around the outside of a histone octamer to form the "beads-on-a-string" structure (The diameter of the string is about $11\,nm$). At the next level of organisation the string of nucleosomes coils into a fibre which is about $30\,nm$ in diameter, and these fibres are then further folded into higher-order structures. Since the experiment were carried out with MAA (methanol and acetic acid, 3:1 in volume) fixed mouse fibroblast cells, due to the fixation and the FISH, there should be loss of histone to some extent. The two extreme situation of the gene structure after FISH will be: bare DNA with total histone loss and chromatin fibre without any histone loss.

The bare DNA fibre was simulated using the worm-like chain model [159], since this structure can be described as an isotropic rod that is continuously flexible. Given the total length of the SV40Tag DNA is $2700\,bp$, a typical structure of this simulation is shown in Figure 14.3. Virtual fluorophores were placed on the bare DNA model in a $10nm$ step and the result was convolved with the theoretical SMI PSF to generate an image. This PSF was simulated using a Khoros PSF simulation plugin written by Rainer Heintzmann to generate a widefield PSF and multiply the result by $\cos^2(2\pi \cdot n \cdot z/\lambda)$ to construct the SMI axial illumination pattern [137]. The simulation was done by David Baddeley using parameters which were typical in real SMI image. The resulted images were evaluated as normal SMI images by the standard SMI evaluation procedure. After 100 times random repeats of this simulation

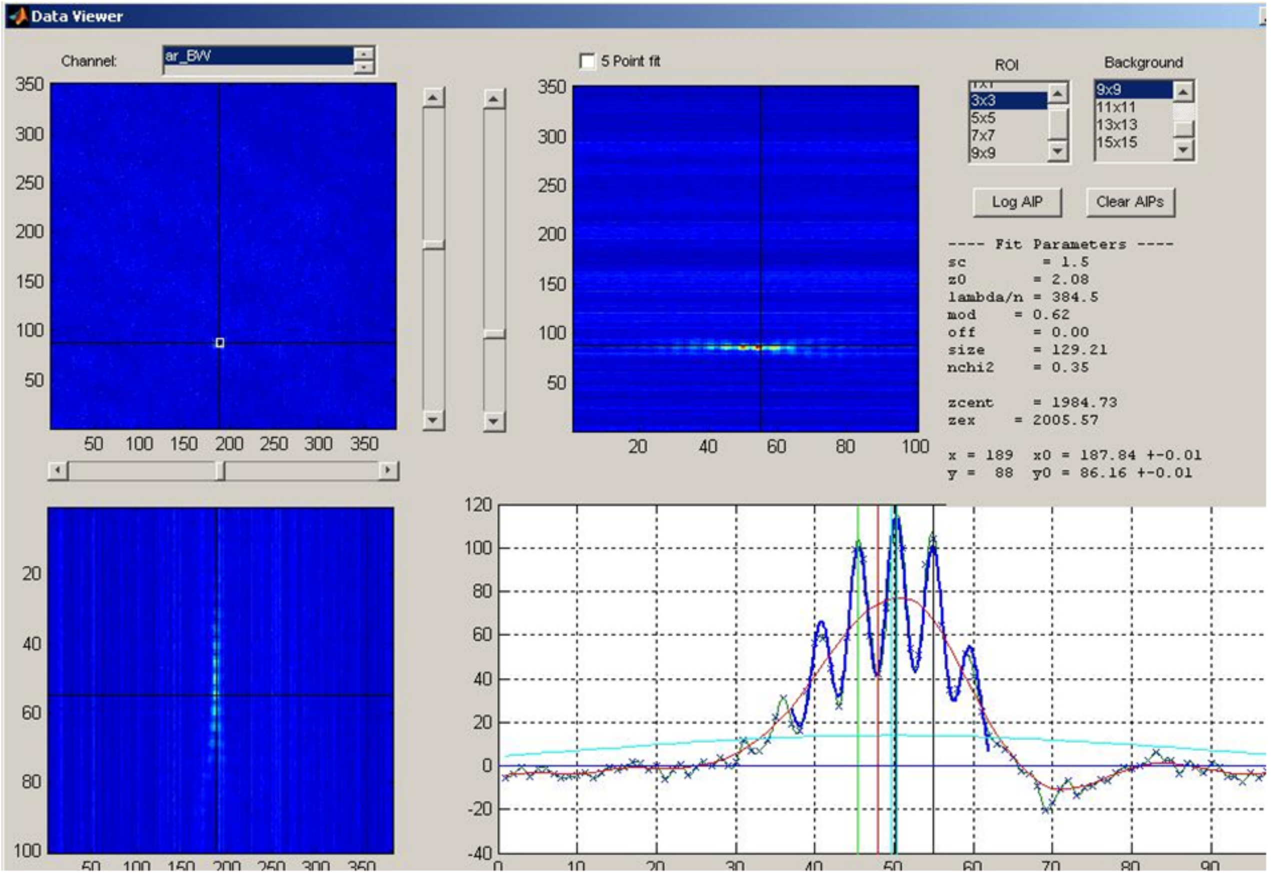

```
---- Fit Parameters ----
sc          = 1.5
z0          = 2.08
lambda/n = 384.5
mod      = 0.62
off         = 0.00
size        = 129.21
nchi2       = 0.35

zcent       = 1984.73
zex      = 2005.57

x = 189   x0 = 187.84 +-0.01
y =  88   y0 = 86.16 +-0.01
```

Figure 14.1. **A screenshot of the interactive data viewer (the "sviewer") when analysing the SV40Tag gene locus.** The x-y, x-z and y-z sections of the object image were displayed, where a typical modulation pattern in the z direction can be observed. Also the fit curve of the axial intensity distribution and the fitted parameters have been shown.

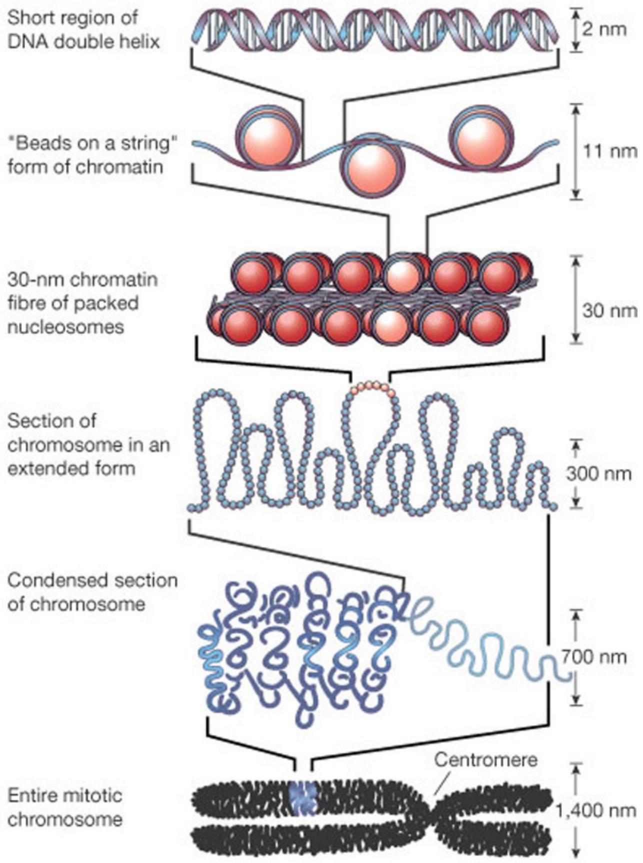

Figure 14.2. **The major chromatin structures during chromosome condensation.** The lowest level of organisation is the nucleosome, where two superhelical turns of DNA (a total of 165 base pairs) are wound around the outside of a histone octamer. Nucleosomes are connected to one another by short stretches of linker DNA and this is called the “beads-on-a-string” structure. The diameter of the string is about 11 nm. At the next level of organisation the string of nucleosomes coils into a fibre which is about 30 nm in diameter, and these fibres are then further folded into higher-order structures. At levels of structure beyond the nucleosome the details of folding are still uncertain. [158]

process, the measured mean size of the structure is $119\,nm$ with a standard deviation of $24\,nm$ (Figure 14.3), which will serve as the upper limit of the SV40Tag gene size measurement.

Although there is no convictive evidence about the chromatin compaction details beyond the $30\,nm$ fibre state, the existence of the $30\,nm$ fibre itself as a distinct secondary higher-order chromatin structure has been supported by a lot of findings [160]. With the "gene density" of the $30\,nm$ fibre state is $105\,bp/nm$ [161], the length of the $30\,nm$ chromatin polymer formed by $2700\,bp$ DNA is about $26\,nm$. Considering the diameter of the chromatin fibre is $30\,nm$, this $26 \times 30\,nm$ structure is unlikely to be further compacted in the higher order chromatin condensation process and should have basically the same behaviour as a $30\,nm$ fluorescent bead under microscope (Figure 14.4). Since this size is already slightly below the lower limit (around $40\,nm$) of precise SMI size measurement, it is not very practical to measure the size distribution of the $30\,nm$ fluorescent beads. Theoretically the measured size should be still around $30\,nm$.

Note that in this section all the measured sizes were expressed in FWHM (full width at half maximum). FWHM is an expression of the extent of a function, which is given here by the distance between points on the object's PSF at which the function reaches half its maximum value (Figure 14.5).

When the function is a normal distribution, the relationship between FWHM and the standard deviation σ is

$$FWHM = 2\sqrt{2\ln 2}\sigma \approx 2.35482\sigma$$

For spherical objects, the relationship between FWHM and the diameter d is

$$FWHM_{sphere} = \frac{d}{\sqrt{2}}$$

14.3. Size Measurements using SMI Microscopy

The optical conditions of the SMI microscope is not always perfect. System errors can be caused by such as aberrated wavefronts, tilted focal plane, slight differences in the intensity of the two laser beams and so on. To reduce this kind of error and measure the actual PSF of the system (modulation depth of the structured illumination), a calibration process using objects with known size is therefore necessary. The calibration process should be carried out using the same objective, at the same excitation and emission wavelengths and with the same refraction index. Since the SV40Tag gene was labelled with Alexa 568 conjugated FISH probe, $100\,nm$ diameter red fluorescent beads (excitation wavelength $568\,nm$, Molecular Probes, Invitrogen) were chosen for the calibration purpose (see Appendix D). All the measurements were carried out using the standard SMI setup in the lab equipped with 100×, NA1.4 oil immersion objectives from the Leica Microsystems. The beads and the cell preparation were both on the coverslips ($170\,\mu m$ thickness), to avoid the decrease in the effective imaging resolution

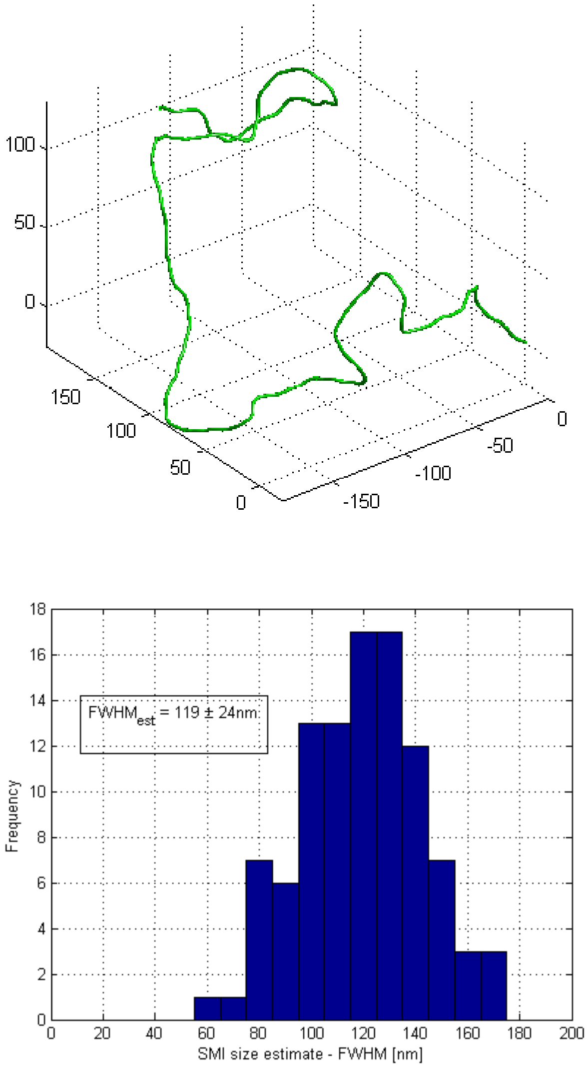

Figure 14.3. **Simulation of** 2700 *bp* **bare DNA doing random walk in a relatively restricted nuclear space using the worm-like chain model.** The upper image is a typical structure of this simulation (axes in nanometer) and the lower one shows the measured size distribution of the structure after 100 times random repeats. The measured mean size of the structure is 119 *nm* with a standard deviation of 24 *nm*. (The simulation was carried out by David Baddeley.)

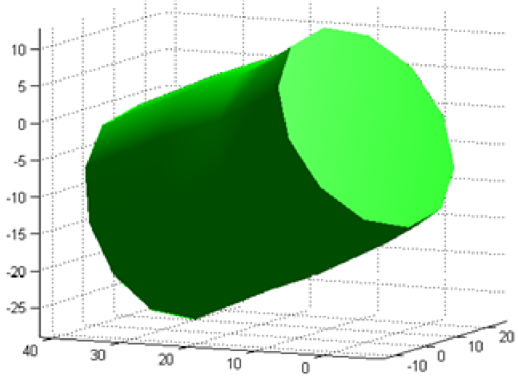

Figure 14.4. **Simulation of the SV40Tag gene ($2700\,bp$) in the $30\,nm$ fibre state using the worm-like chain model.** Knowing the "gene density" of the $30\,nm$ fibre state is $105\,bp/nm$, the $30\,nm$ chromatin polymer formed by $2700\,bp$ DNA is about $26\,nm$ in length, which is unlikely to be further compacted in the higher order chromatin condensation process. The axes are in nanometer. (The simulation was carried out by David Baddeley.)

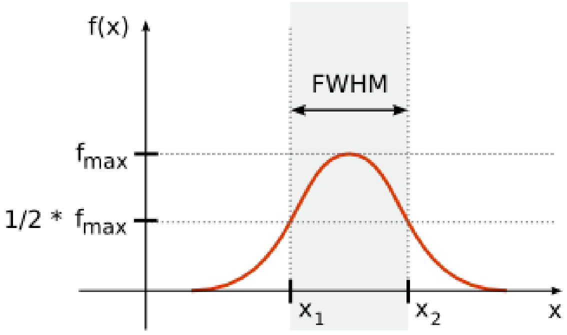

Figure 14.5. **The definition of full width at half maximum (FWHM).** It is an expression of the extent of a function, which is given by the distance between points on the function at which the function reaches half its maximum value. (Wikipedia)

and signal strength caused by the objects-coverslip distance. The specimens were all mounted with VECTASHIELD Mounting Medium (Vector Laboratories) whose refraction index is 1.44. Though ideally it will be the best to inject the fluorescent beads into the cells to have the exact refraction index match, practically this is hard to realize and the signals may disturb each other. Here the beads sample and the FISH specimen were prepared on separate coverslips, yet still gave results that were accurate enough.

Figure 14.6 shows the analysis result of the 100 nm beads sample exported by the *sviewer* package. All together 89 beads signal were detected and 2 of them were too large for the fit (black points in the colour map, which are probably beads clusters), the mean size of the left 87 is 94.58 nm, which is in good agreement with the manufacturer stated size considering its intrinsic size fluctuations. The distribution of the sizes is narrow (standard deviation 10.29 nm), which indicates the high reproducibility and precision of SMI size measurement. Considering the relationship of diameter with FWHM for spherical object is $FWHM_{sphere} = d/\sqrt{2}$, the above mentioned mean size and standard deviation in diameter can be translated into $66.9 \pm 7.3\,nm$ in FWHM, to in agreement with the gene size measurements afterwards.

The SV40Tag gene was labelled with Alexa 568 conjugated FISH probe in MAA (methanol and acetic acid, 3:1 in volume) fixed mouse fibroblast (C57SV cell line). The image in Figure 14.7 is a maximum intensity projection in the z-axis of the image stack taking through the nucleus with an axial step size of 40 nm. The evaluation process was the same as with the beads sample (Figure 14.8). Note that though the analysis can be automatically executed by the Matlab script, the fit process of every gene locus has been verified by hand to make sure that the signal was suitable for SMI analysis, meaning neither too large for the fit nor too small that has been treated as noise. Figure 14.9 shows an example of the main steps of individual data evaluation process. A single gene locus was identified by the command "`ofind3`" using the multi-thresholding method. The sensitivity of the object detection can be changed manually. The identified locus was then analysed by the fitting procedure named "`dofits`". The modulation depth can be calculated from the fitting curve, which was then interpolated into the calibration curve (Figure 5.7) by Matlab to extract the size value. In the end, all the 84 gene loci were proved to be suitable for the analysis using the *sviewer* package. The mean size of the SV40Tag gene measured by SMI microscopy is 93.4 nm with a standard deviation of 25.0 nm (Figure 14.10).

14.4. Size Measurements using CLSM

The same gene region was subjected to confocal microscopy using a different analysing strategy. A model based method was designed for accurate quantification of the 3D structure of fluorescently labelled cellular objects similar in size to the optical resolution limit [162]. In this method, a mathematical model was fitted to the raw image data, which approximated the object by a small number of discrete points that are convolved with the microscope PSF to give the image. The lateral and axial microscope PSFs

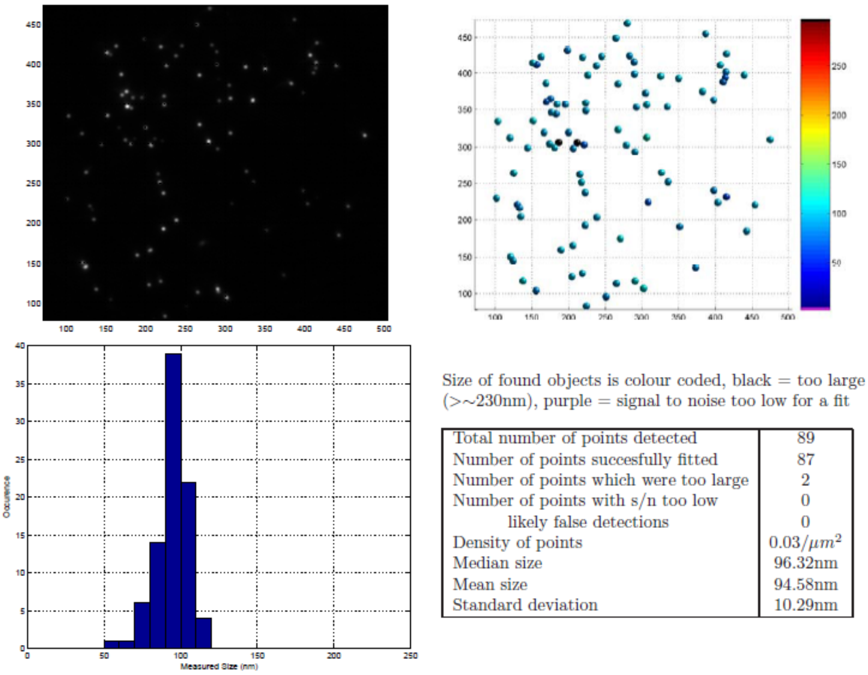

Size of found objects is colour coded, black = too large (>~230nm), purple = signal to noise too low for a fit

Total number of points detected	89
Number of points succesfully fitted	87
Number of points which were too large	2
Number of points with s/n too low	0
likely false detections	0
Density of points	$0.03/\mu m^2$
Median size	96.32nm
Mean size	94.58nm
Standard deviation	10.29nm

Figure 14.6. **The analysis output of a 100nm beads sample evaluated by the *sviewer* package.** The image of the beads was taken at 568 nm excitation and it was the maximum intensity projection of the image stack along the z-axis (upper panel, left), accompanying with the colour coded representation of the size estimation (upper panel, right). In the colour map black means the object is larger than about 230 nm which is too large for a fit and purple means the signal to noise ratio of the image is too low for that. In the lower panel is the size distribution of the measured beads and some basic statistics. Note that the measured diameter of the beads sample is $94.58 \pm 10.29\,nm$ which is in good agreement with the manufacturer stated size and shows the high reproducibility and precision of SMI size measurement.

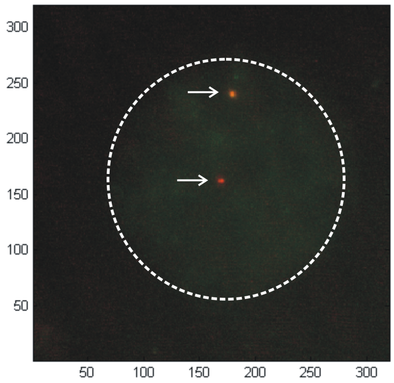

Figure 14.7. **A mouse fibroblast cell nucleus (C57SV cell line) recorded with SMI microscopy.** The image stack was acquired using the standard SMI setup in the lab equipped with 100×, NA1.4 oil immersion objectives from the Leica Microsystems, at excitation wavelength 568 nm, taking optical sections with an axial step size of 40 nm. The image presented is the maximum intensity z-projection of the image stack. The nucleus was visible due to low-level autofluorescence and the SV40Tag gene was labelled with Alexa 568 conjugated FISH probe.

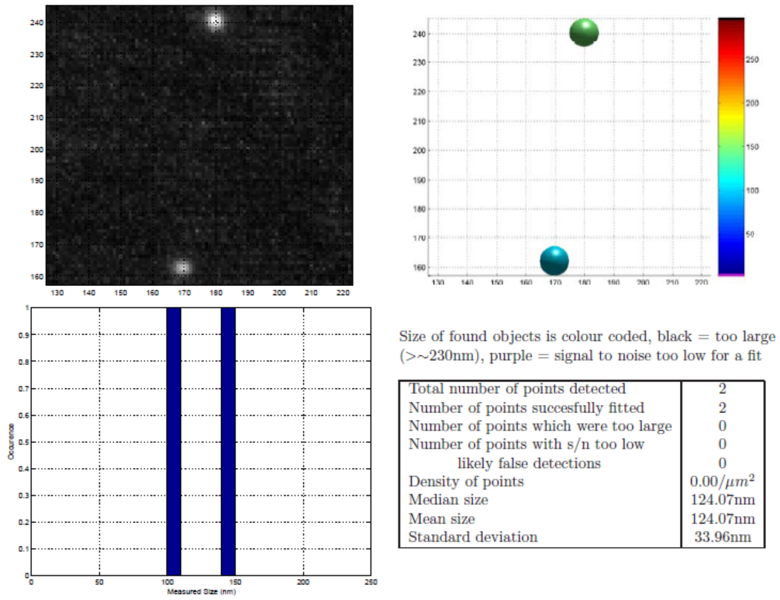

Size of found objects is colour coded, black = too large (>~230nm), purple = signal to noise too low for a fit

Total number of points detected	2
Number of points succesfully fitted	2
Number of points which were too large	0
Number of points with s/n too low	0
likely false detections	0
Density of points	$0.00/\mu m^2$
Median size	124.07nm
Mean size	124.07nm
Standard deviation	33.96nm

Figure 14.8. **The analysis output of the SV40Tag gene loci in the cell of Figure 14.7 obtained by the *sviewer* package.** The image of the gene loci and the corresponding colour map of the size estimation are shown, together with the basic statistics of two size parameters, though what is more important for the final analysis is the individual size of every gene locus (not displayed here).

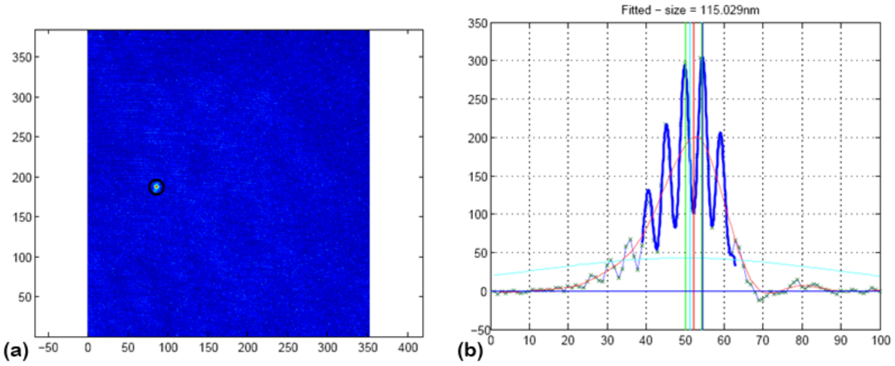

Figure 14.9. **The crucial steps in data evaluation.** (a) shows the result of the command "`ofind3`". A single gene locus was identified by the multi-thresholding method. The sensitivity of the object detection can be changed manually. (b) The identified locus was analysed by the automated fitting procedure named "`dofits`". The modulation depth can be calculated from the fitting curve, which was then interpolated into the calibration curve (Figure 5.7) by Matlab to extract the size value. In this case, the fitted size of the gene locus was 115.03 nm.

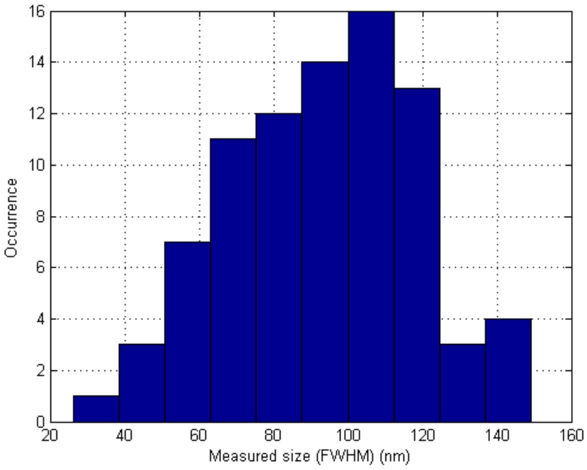

Mean Size (FWHM, nm)	93.4
Median Size (FWHM, nm)	96.9
Standard Deviation (nm)	25.0
Number of Gene Loci	84

Figure 14.10. **The size distribution of the SV40Tag gene loci measured by SMI microscopy.** 84 gene loci were evaluated and the mean size is 93.4 nm with a standard deviation of 25.0 nm.

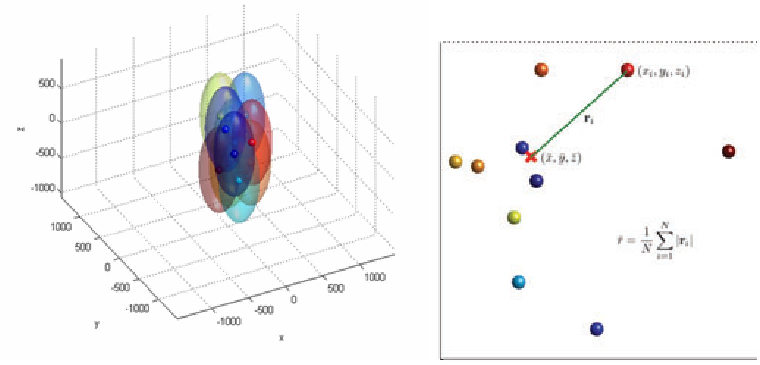

Figure 14.11. **The multi-point model. Left:** The object is approximated by a small number of discrete points (10 points are used here) which are convolved with the microscope PSF to give the image. The lateral and axial PSFs can be determined by calibration objects like fluorescent beads. **Right:** The mean distance of the fitted points to the object centre is taken as the size parameter which can be transformed into the FWHM of a matching Gaussian. [162]

were determined by calibration objects (here fluorescent beads were used, data not shown) ideally under the same optical conditions as the objects to be measured. 10 points were used here to approximate the object as a compromise between final accuracy, noise sensitivity, sensitivity to PSF approximations, convergence and speed. The mean distance of the fitted points to the object centre is taken as the size parameter which can be transformed into the FWHM of a matching Gaussian (Figure 14.11).

Using this method, 72 gene loci were evaluated and a typical result page is shown in Figure 14.12. The cells (mouse fibroblast, C57SV cell line) were fixed with methanol and acetic acid. The nucleus was counterstained with To-Pro-3 iodide and the SV40Tag gene was labelled with Alexa 568 conjugated FISH probe. Image acquisition was carried out with a Leica TCS NT Confocal Laser Scanning Microscope (CLSM) equipped with a PlanApo 63x, NA= 1.4 oil immersion objective. Image stacks were taken through the optical axis with an axial step size of 203nm to render the z-projection images of the nuclear profiles. The SV40Tag gene loci were fitted with the 10 points model and the parameters needed for the gene size and shape estimation were calculated. From the results one can see the fit and the original image are in good agreement. Figure 14.13 shows the size distribution of the 72 gene loci, with the mean size $283.8\,nm$ and a standard deviation of $51.6\,nm$.

14.5. The Comparison between the Theoretical Gene Size and Different Measurements

This chapter demonstrated a method to measure the precise axial extension of tiny gene locus using SMI microscopy. By using the so called PSF engineering method, SMI microscopy is able to enhance the precision of the size and distance measurement to about $2-5\,nm$ in the axial direction,

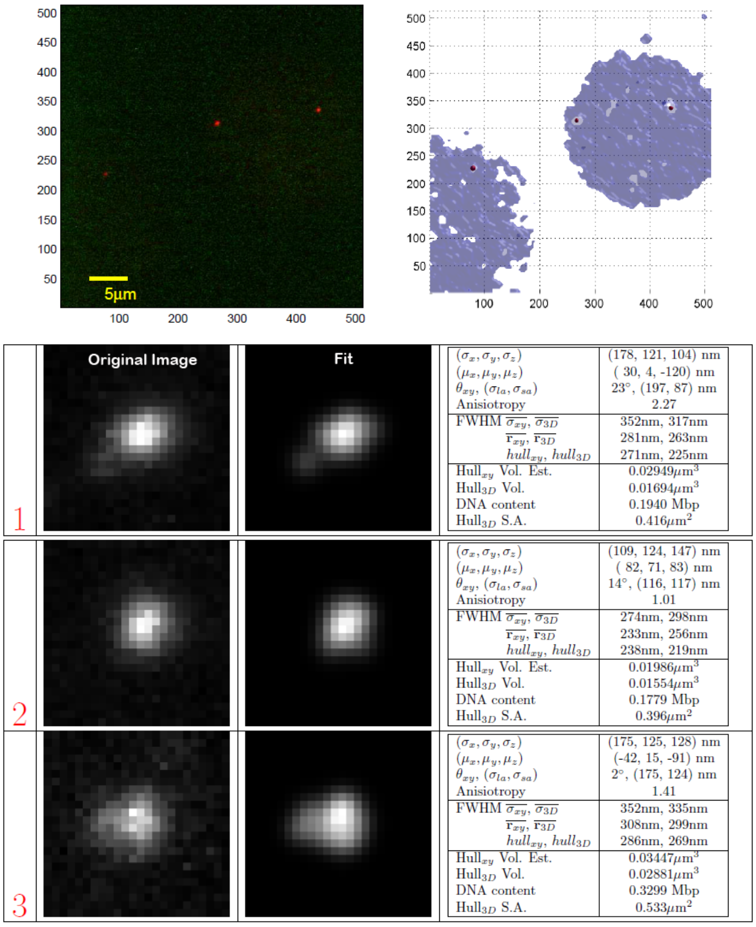

$(\sigma_x, \sigma_y, \sigma_z)$	(178, 121, 104) nm
(μ_x, μ_y, μ_z)	(30, 4, -120) nm
θ_{xy}, $(\sigma_{la}, \sigma_{sa})$	23°, (197, 87) nm
Anisiotropy	2.27
FWHM $\overline{\sigma_{xy}}, \overline{\sigma_{3D}}$	352nm, 317nm
$\overline{\mathbf{r}_{xy}}, \overline{\mathbf{r}_{3D}}$	281nm, 263nm
$hull_{xy}$, $hull_{3D}$	271nm, 225nm
Hull$_{xy}$ Vol. Est.	0.02949μm^3
Hull$_{3D}$ Vol.	0.01694μm^3
DNA content	0.1940 Mbp
Hull$_{3D}$ S.A.	0.416μm^2

$(\sigma_x, \sigma_y, \sigma_z)$	(109, 124, 147) nm
(μ_x, μ_y, μ_z)	(82, 71, 83) nm
θ_{xy}, $(\sigma_{la}, \sigma_{sa})$	14°, (116, 117) nm
Anisiotropy	1.01
FWHM $\overline{\sigma_{xy}}, \overline{\sigma_{3D}}$	274nm, 298nm
$\overline{\mathbf{r}_{xy}}, \overline{\mathbf{r}_{3D}}$	233nm, 256nm
$hull_{xy}$, $hull_{3D}$	238nm, 219nm
Hull$_{xy}$ Vol. Est.	0.01986μm^3
Hull$_{3D}$ Vol.	0.01554μm^3
DNA content	0.1779 Mbp
Hull$_{3D}$ S.A.	0.396μm^2

$(\sigma_x, \sigma_y, \sigma_z)$	(175, 125, 128) nm
(μ_x, μ_y, μ_z)	(-42, 15, -91) nm
θ_{xy}, $(\sigma_{la}, \sigma_{sa})$	2°, (175, 124) nm
Anisiotropy	1.41
FWHM $\overline{\sigma_{xy}}, \overline{\sigma_{3D}}$	352nm, 335nm
$\overline{\mathbf{r}_{xy}}, \overline{\mathbf{r}_{3D}}$	308nm, 299nm
$hull_{xy}$, $hull_{3D}$	286nm, 269nm
Hull$_{xy}$ Vol. Est.	0.03447μm^3
Hull$_{3D}$ Vol.	0.02881μm^3
DNA content	0.3299 Mbp
Hull$_{3D}$ S.A.	0.533μm^2

Figure 14.12. **Using the multi-point model to evaluate the SV40Tag gene size.** Two methanol and acetic acid fixed mouse fibroblast cells (C57SV cell line) are shown in the upper panel. The image was acquired with a Leica TCS NT Confocal Laser Scanning Microscope (CLSM) equipped with a PlanApo 63x, NA= 1.4 oil immersion objective. The image presents the maximum intensity z-projection of the image stack taken through the optical axis with an axial step size of 203nm. The nucleus was counterstained with To-Pro-3 iodide and the SV40Tag gene was labelled with Alexa 568 conjugated FISH probe. The lower panel is the SV40Tag gene loci images (left) and the corresponding 10 points fit (right). All the parameters needed for the gene size and shape estimation are listed.

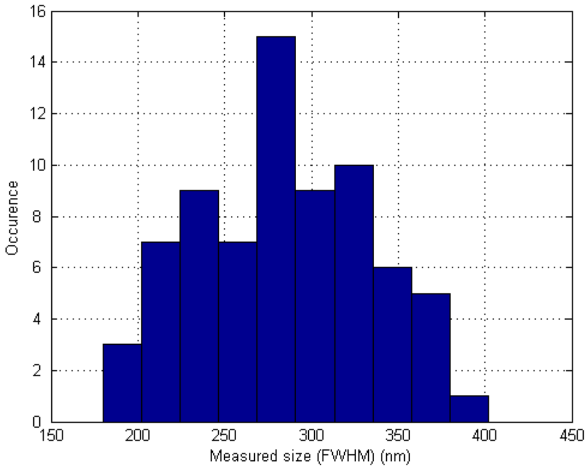

Mean Size (FWHM, nm)	283.8
Median Size (FWHM, nm)	281.5
Standard Deviation (nm)	51.6
Number of Gene Loci	72

Figure 14.13. **The size distribution of the SV40Tag gene loci measured with confocal microscopy.** 72 gene loci were evaluated and the mean size is 283.8 nm with a standard deviation of 51.6 nm.

which makes it possible to measure sizes that are far beyond the limits of conventional high-resolution fluorescence microscopy (about 600 nm in the axial direction for confocal microscopy) [128] [163].

In this work, the 2.7 kb long viral oncogene SV40Tag was fluorescently labelled and its axial extension was measured with both SMI and confocal microscopy, with the results compared in Figure 14.14. With SMI microscopy, 84 gene loci were evaluated using the Matlab based *sviewer* package, resulting in a mean size of $93.4 \pm 25.0\,nm$. The same labelled gene loci were also analysed with confocal microscopy using the newly developed model based method (the "multi-point model", [162]) which shows significantly better accuracy than threshold based methods. The mean size was $283.8 \pm 51.6\,nm$ after analysing 72 gene loci. Note that the distribution of SMI measured sizes is much narrower than that of confocal microscopy (standard deviation 25.0 nm and 51.6 nm, for SMI and confocal microscopy, respectively), revealing the significant measuring precision enhancement with SMI microscopy.

Noticing that the resolution of confocal microscopy is about 250 nm laterally and 600 nm axially, the simulated upper limit of the gene size ($119 \pm 24\,nm$) is already far below these values. Therefore we can conclude that confocal microscopy is not suitable for measuring such tiny gene size and the measurements are not accurate any more. This is also the reason that the two size distributions are not overlapping at all. By comparison, with the power of precise size determination in the range of $40 - 200\,nm$, SMI microscopy is extremely suitable for this kind of measurement, showing its application in investigating specific chromatin condensation status in the area of functional genome topology.

SMI microscopy has been used to measure the size of fluorescent beads with high accuracy in previous experiments, which was proved again in this work. The measurement of a group of $100\,nm$ diameter red fluorescent beads (excitation length $568\,nm$) gave a mean size and standard deviation of $94.58 \pm 10.29\,nm$ (in diameter, which is $66.9 \pm 7.3\,nm$ in FWHM). This value is in good agreement with the manufacturer stated size and the theoretical SMI measuring accuracy. Beads measurement is also important for calibrating the standing wave field of the microscope interferometer prior to the size measurement of the gene loci. The value acquired with the beads measurement was then entered in the fields of "*`umod`*" and "*`ref_beads`*" right after the command "`connectToDB`". The gene size measurement afterwards resulted in a mean size of $93.4\,nm$, with a standard deviation of $25.0\,nm$. Considering biological structures are usually not as bright as the fluorescent beads, have various extensions with different intensities, locate inside the cell where refraction index mismatch happens and their distances from the coverslip are also variable, the slightly larger standard deviation is within the acceptable range.

Comparing the measured gene size with the simulated data, we can be sure that the chromatin condensation state after FISH is not $30\,nm$ fibre, since the mean size $93.4 \pm 25.0\,nm$ is much more larger than the simulated $30\,nm$. This is reasonable because the protein digestion and denaturation steps in FISH will certain cause some histone loss. The standard deviation of the measured data ($25.0\,nm$) is almost the same with that of the simulated bare DNA random walk ($24\,nm$), which indicates similar order of chromatin structure. However with the smaller mean size, $93.4\,nm$ for the measurement compared with the simulated $119\,nm$, the gene loci should have a tighter compaction than bare DNA random walk, which is also reasonable since the histone loss is not likely to be complete. One thing needs to be mentioned is the copy number of the SV40Tag gene per insert site is not clear yet, though experiments to determine this have already been arranged. In this work, one copy of the gene was assumed to establish the technical platform. Nevertheless, the whole methodology is the same as established here, just the simulated parameters will change accordingly. If there are more than one copies of the gene, the simulated sizes will be larger and the measured gene condensation state after FISH will therefore prove to be more compact.

It has been reported before that methanol and acetic acid fixation of the cell and the following fluorescent *in situ* hybridisation can cause protein loss [164, 165] and certain nuclear structure distortion [166]. Recent study [30, 98] proved that this is not the case with cryo-FISH. Immunolabelling of histone H2B with $5\,nm$ gold particles imaged with electron microscope (EM) revealed that the nanostructure of euchromatin and heterochromatin was well preserved before and after cryo-FISH. Additionally, the preparation of the cryosections with the standard method used in this work preserved the cellular ultrastructure well, as shown by electron microscope imaging [107]. Therefore, it will be extremely suitable to measure the SV40Tag gene size using cryo-FISH in cryosections. Former study [155] showed that the size

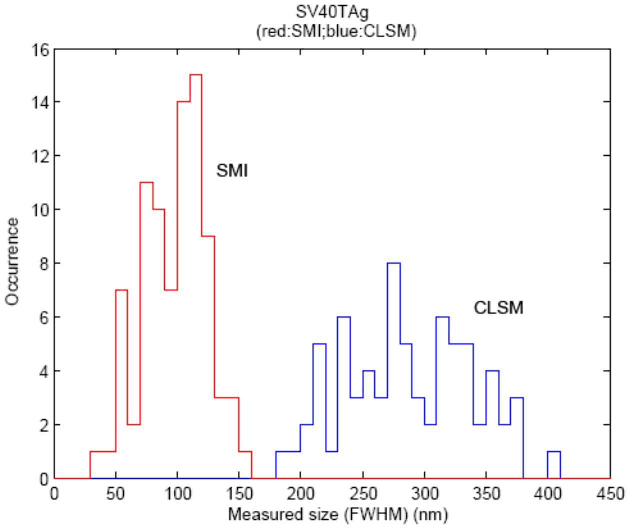

	Mean Size (FWHM, nm)	Median Size (FWHM, nm)	Standard Deviation (nm)	Number of Gene Loci
SMI	93.4	96.9	25.0	84
CLSM	283.8	281.5	51.6	72

Figure 14.14. **The comparison of the size distribution of the SV40Tag gene loci measured with SMI and Confocal microscopy.** The distribution of SMI measured sizes is much narrower than that of confocal microscopy (standard deviation 25.0 *nm* and 51.6 *nm*, for SMI and confocal microscopy, respectively), revealing the significant measuring precision enhancement with SMI microscopy.

of the same structure measured by SMI is in the same order of magnitude with that measured by EM, though the SMI measured sizes are lightly larger. This is probably due to the difficulty of detecting objects smaller than about 40 *nm* with SMI, which is not really a problem for measuring the SV40Tag gene loci, especially in comparative study, like during physiological changes and disease as planed in this work.

Part III

Conclusion and Outlook

This thesis presents the first effort to investigate genome organisation during the tumorigenesis process combining fluorescent *in situ* hybridisation and tissue cryosections. The parameters of specific genome structure measured in this work are the most precise values one can get from tissue sections so far.

Cryo-FISH and Stereological Methods Ensure the High Measuring Precision

The precision of the measurements is provided by the combination of the cryo-FISH technique and the stereological methods. Instead of single cells, thin tissue cryosections have been used in this work to enable the investigation of the genome structure within its natural context. The tissue blocks were first fixed with paraformaldehyde, which preserved the ultrastructure, then embedded in sucrose and rapidly frozen by immersion in liquid nitrogen. Cryosections (about 200 nm thick) were cut using an ultracryomicrotome, captured on sucrose drops and transferred to a glass coverslip. The cryosections have not been subjected to detergents, organic solvents, drying or high temperatures, which ensured the well preservation of nuclear ultrastructure.

Prior to fluorescence *in situ* hybridisation, the sucrose can be washed away by rinsing in PBS, yielding a thin tissue section that is not hindered by paraffin. The direct probe accessibility makes it possible to avoid harsh protein digestion before hybridisaion and the chromatin nanostructure is preserved during cryo-FISH. Besides, the use of thin cryosections significantly improved imaging resolution, especially in the z-axis, and also the ability to resolve chromosome territory organisation during interphase.

In the DAPI-stained mouse mammary tissue cryosections used in this work, the chromatin structure can be clearly distinguished. The chromatin is not evenly distributed in the nucleus. The tightly packed heterochromatin is intensely stained and gathers mainly at the periphery of the nucleus. The less compacted euchromatin stains lighter and occupies the rest of the nuclear space. The chromocenters appear as densely-stained bright points.

To extract quantitative information about the 3D genome structure from the 2D nuclear sections, stereological methods were introduced for data analysis. In the nuclear radius measurement, sequential subtraction method was used to subtract all the polar sections from the whole population of nuclear sections, leaving only the equatorial sections to represent the true size distribution of the nuclei. For calculating the volume fraction of chromosome 11, the basic stereology principle $V_V = P_P = A_A$ was applied. In this method, an appropriately designed probe, e.g., a grid of points, is used to sample a particular structure. Interactions of the probes with features of interest are noted and counted. The mean of these counts is then computed and normalized, which gives the expected value of the point fraction of the interaction, which is equal to the volume fraction of the structure. In digital images, the point fraction is equal to the area fraction of the pixels, therefore the volume fraction of the chromosome in the nucleus was estimated by the area fraction of it in the nuclear sections.

The expected value relationships of stereology are powerful because they require no assumptions about the geometry of the features being examined, as long as the probe is ***I***sotropic, ***U***niform and ***R***andom (the "***IUR***" rules). The probes, which are the grids of pixels in this work, are "***U***niformly" distributed and have no directions ("***I***sotropic") due to the nature of digital images, and the structure itself (the chromosome) and the acquisition of the images are ***R***andom, therefore the ground rules "***IUR***" are all satisfied, which makes sure that the estimation is unbiased.

The Genome-wide Chromatin Condensation State Changes during Tumorigenesis

In the nuclear volume measurements and the calculation of chromosome 11 volume and nuclear radial position, the same set of tissue cryosections were used for data evaluation. Three types of cryosections from the mammary gland of the transgenic mice were used to represent the whole tumorigenesis process. One is from the healthy mouse without any pregnancy and lactation ("normal"); the second is from the normal mammary tissue of the mouse with 5 rounds of pregnancy and lactation ("lactated"), during which the oncogene has been transcribed; and the last is from the mammary tumor of the transgenic mice ("tumor"), at which state the oncogene has been activated.

The whole genome wide chromatin condensation state is reflected from the nuclear volume which can be represented by the nuclear radius. The average nuclear radii in the cases of "lactated" ($2.35\,\mu m$) and "tumor" ($2.64\,\mu m$) are smaller than that of the "normal" case ($2.67\,\mu m$), and the differences among the three size distributions are statistically significant.

In the mammary tumor state, the distribution of the nuclear radii of the tumor cells is much wider than the other two, which indicates the loss of growth control property of tumor cells. The nuclear volumes range from $7.2\,\mu m^3$ to $356.8\,\mu m^3$. The largest volume of the nuclei in the "tumor" case is about two-fold of that in the "normal" case and about three-fold of that in the "lactated" case, indicating the existence of nuclei which have double DNA content. The extremely small nuclei in the "tumor" case, with a volume ($7.2\,\mu m^3$) only about one fifth of the smallest nuclei in the "normal" case and about one third of the smallest nuclei in the "lactated" case, implicating the existence of highly condensed nuclei, which seems to be the unique situation of malignancy.

Chromosome Volume and Nuclear Radial Position Changes are not Correlated

The volume of chromosome 11 did not stay the same during physiological changes and tumorigenesis, indicating that the chromatin condensation state is dynamic in this process. While the absolute volume of the chromosome ranges from $1.7\,\mu m^3$ to $9.9\,\mu m^3$ in the "normal" case, from $1.0\,\mu m^3$ to $4.4\,\mu m^3$

in the “lactated” case and from $0.2\,\mu m^3$ to $10.7\,\mu m^3$ in the “tumor” case, the relative volume fraction of the chromosome in the nucleus becomes smaller all the way from the case of “normal” to “tumor”, which is 5.07% for the “normal” case, 3.91% for the “lactated” case and 3.00% for the “tumor” case. It is very likely that the genes on chromosome 11 had different transcriptional activities in various physiological states, which caused the relative volume changes in different states. The measured volume fractions of chromosome 11 in all the three cases are different from the genomic size fraction of the chromosome in the whole genome (4.62%), which means the chromatin distribution in the nucleus is uneven.

Different from the volume changes, the distributions of chromosome 11 nuclear radial positions remained unchanged in the tumorigenesis process. In the three cases investigated in this work, chromosome 11 always located in the interior of the cell nuclei (peak value at 55%-65% of the nuclear radius). This result is in agreement with the gene density related chromosome radial positioning theory, since chromosome 11 is the second most gene-dense chromosome in the mouse karyotype. Interestingly, similar results from cultured cells have also been report before. Dietzel and colleagues analysed the radial distribution of several mouse chromosomes in different cell types using 3D-FISH [145], and the results showed that chromosome 11 always located much more internally than all other chromosomes in mouse lymphocyte, fibroblast and embryonic stem cell nuclei. It seems that the nuclear position of chromosome 11 is conserved in mouse cells.

The Preliminary Results Regarding the Viral Oncogene SV40Tag

The activity of the viral oncogene SV40Tag varies in different physiological states of the cells. The preliminary co-hybrdisation of SV40Tag and chromosome 11 in the mammary tumor cryosection implied that the oncogene located at the nuclear periphery and mostly out of the chromosome territory when the gene is activated, although only the statistical results from large number of nuclear profiles in different states can really give a conclusion.

The methodology for analysing the oncogene’s extension was established with a mouse fibroblast cell line (C57SV) transformed with SV40 DNA. The gene’s axial extension was measured with the spatially modulated illumination (SMI) microscopy and evaluated with a Matlab algorithm which aims to automatically extract information about the object size and position from the axial profile taken through the object.

In this work, the $2.7\,kb$ long viral oncogene SV40Tag was fluorescently labelled and 84 gene loci were evaluated, resulting in a mean size of $93.4 \pm 25.0\,nm$, which is in the range of the simulated $30\,nm$ ($30\,nm$ fibre) to $119 \pm 24\,nm$ (bare DNA random walk).

Comparing the measured gene size with the simulated data, we can be sure that the chromatin condensation state after FISH is not $30\,nm$ fibre, which is due to the histone loss caused by the protein digestion and denaturation steps in FISH. The standard deviation of the measured data

(25.0 nm) is almost the same with that of the simulated bare DNA random walk (24 nm), which indicates similar order of chromatin structure. However with the smaller mean size, 93.4 nm for the measurement compared with the simulated 119 nm, the gene loci should have a tighter compaction than bare DNA random walk, which is reasonable since the histone loss is not likely to be complete. Thinking of the nuclear ultrastructure preservation, it will be extremely suitable to measure the SV40Tag gene size using cryo-FISH and SMI microscopy in cryosections.

Outlook

The methodology established in this work can be extended to the investigation of the nuclear organisation of all the chromosomes, which will then provide an overall concept of the dynamic of genome structure during tumorigenesis. The multicolorFISH (M-FISH) method can be used for this purpose, which allows the visualisation of all chromosomes in different colours within one hybridisation. Also knowing the gene expression profile on each chromosome can help to better interpret the relationship between gene activity and the spatial genome organisation.

Mammary tissue typically contains cuboidal epithelial cells, myoepithelial cells as well as a thin layer of fibroblast cells. In the tissue section, some blood cells and lymphocytes can also exist. The existence of the non-epithelial cells can cause errors in the genome structure study, since the genome organisation is tissue- and cell type- specific. According to the “IUR” rules of stereological methods, the images of all the nuclei have been acquired to ensure the “random” rule. This is acceptable due to the fact that the vast majority of the mammary tissue is epithelial cells, but ideally an antibody should be used to label the epithelial cells, to make sure the genome structure study is carried out strictly within one single cell type.

Due to several practical difficulties, only the preliminary experiments regarding the nuclear position and condensation state changes of the oncogene SV40Tag during the tumorigenesis has been done. Statistics with the three different groups of cryosections is required to draw conclusion of the results and hypothesis revealed by the preliminary experiments, which should be the major topic of the proceeding projects.

Although the structure parameters presented in this work are already the most precise measurements using tissue sections so far, the precision can be enhanced to a higher level by including larger amount of nuclear profiles and using the super-resolution microscopy. The newly developed localization nanoscopy combining spectral precision distance microscopy (SPDM) in the Cremer group allows resolution in the 10-nm range [167]. This technique is based on precise object localization after the optical isolation of single signals, and it is ready to be applied to this study as soon as there is proper probes to label the mouse genome.

Part IV

Appendices

Appendix A

The Measured Nuclear Section Radii of the Cryosections from the "Normal" Mouse

Various nuclear sections can be generated from the cutting process of the cryosections, from polar sections to equatorial sections. The polar section from the large nucleus can have the same size with the equatorial section from the small nucleus. Therefore, to calculate the nuclear radius distribution of certain cryosections, a method which can extract all the equatorial sections from the whole population to represent the true size distribution is required. Sequential subtraction method was introduced for the exact purpose.

In this work, the calculating process of the radius distribution of the nuclei from the "normal" mammary gland cryosections was used as an example to demonstrate this method (see Section 9.1). The original data of all the measured nuclear section radii was listed in the table here. The whole nucleus was first measured by "Image J - Analyze - Set Measurements - Area", resulted in a area value in pixel. Since all the image acquisition used a pixel size of $65.5\,nm$, the area in pixel was expressed in μm^2 by multiplying 0.0655^2. Then the area value was translated into equivalent radius by the formula $r = \sqrt{\frac{A}{\pi}}$, where r is the equivalent section radius and A is the section area.

In the case of the cryosections from the normal mouse mammary gland, as observed in the table, the minimum and maximum radius of the nuclear sections was observed to be $0.9\,\mu m$ and $3.6\,\mu m$, respectively. Then the nuclear section radii were grouped into different size categories in this size range. How many values fell into each size category was calculated and listed in Table 9.1, and the rest of the calculations were explained in Section 9.1.

Table A.1: The Nuclear Section Radii of the Cryosections from the "Normal" Mouse.

Nuclear Sections	Area (pixel)	Area (μm^2)	Radius (μm)
Normal_1	3244	13.9	2.1
Normal_2	3837	16.5	2.3
Normal_3	2867	12.3	2.0
Normal_4	2750	11.8	1.9
Normal_5	3480	14.9	2.2
Normal_6	6587	28.3	3.0
Normal_7	5984	25.7	2.9
Normal_8	1634	7.0	1.5
Normal_9	3774	16.2	2.3
Normal_10	5003	21.5	2.6

Normal_11	786	3.4	1.0
Normal_12	2242	9.6	1.7
Normal_13	2950	12.7	2.0
Normal_14	6806	29.2	3.0
Normal_15	3832	16.4	2.3
Normal_16	1109	4.8	1.2
Normal_17	3877	16.6	2.3
Normal_18	1660	7.1	1.5
Normal_19	2498	10.7	1.8
Normal_20	3412	14.6	2.2
Normal_21	3241	13.9	2.1
Normal_22	1308	5.6	1.3
Normal_23	2143	9.2	1.7
Normal_24	1398	6.0	1.4
Normal_25	5275	22.6	2.7
Normal_26	3556	15.3	2.2
Normal_27	6364	27.3	2.9
Normal_28	5520	23.7	2.7
Normal_29	3945	16.9	2.3
Normal_30	2663	11.4	1.9
Normal_31	4608	19.8	2.5
Normal_32	1549	6.6	1.5
Normal_33	2680	11.5	1.9
Normal_34	2618	11.2	1.9
Normal_35	1423	6.1	1.4
Normal_36	3905	16.8	2.3
Normal_37	4710	20.2	2.5
Normal_38	3549	15.2	2.2
Normal_39	1622	7.0	1.5
Normal_40	1144	4.9	1.2
Normal_41	2224	9.5	1.7
Normal_42	2984	12.8	2.0
Normal_43	2074	8.9	1.7
Normal_44	3863	16.6	2.3
Normal_45	711	3.1	1.0
Normal_46	4442	19.1	2.5
Normal_47	4684	20.1	2.5
Normal_48	3363	14.4	2.1
Normal_49	7371	31.6	3.2
Normal_50	4059	17.4	2.4
Normal_51	7130	30.6	3.1
Normal_52	3396	14.6	2.2
Normal_53	4584	19.7	2.5
Normal_54	4463	19.1	2.5
Normal_55	9100	39.0	3.5

Normal_56	5222	22.4	2.7
Normal_57	5148	22.1	2.7
Normal_58	1225	5.3	1.3
Normal_59	1753	7.5	1.5
Normal_60	1866	8.0	1.6
Normal_61	1028	4.4	1.2
Normal_62	3176	13.6	2.1
Normal_63	2869	12.3	2.0
Normal_64	2864	12.3	2.0
Normal_65	3580	15.4	2.2
Normal_66	843	3.6	1.1
Normal_67	6741	28.9	3.0
Normal_68	4153	17.8	2.4
Normal_69	4760	20.4	2.5
Normal_70	6656	28.6	3.0
Normal_71	3558	15.3	2.2
Normal_72	1642	7.0	1.5
Normal_73	609	2.6	0.9
Normal_74	2862	12.3	2.0
Normal_75	5143	22.1	2.7
Normal_76	1206	5.2	1.3
Normal_77	1361	5.8	1.4
Normal_78	5881	25.2	2.8
Normal_79	2730	11.7	1.9
Normal_80	1397	6.0	1.4
Normal_81	2682	11.5	1.9
Normal_82	7029	30.2	3.1
Normal_83	1486	6.4	1.4
Normal_84	3446	14.8	2.2
Normal_85	2257	9.7	1.8
Normal_86	1279	5.5	1.3
Normal_87	1008	4.3	1.2
Normal_88	1242	5.3	1.3
Normal_89	3366	14.4	2.1
Normal_90	2004	8.6	1.7
Normal_91	750	3.2	1.0
Normal_92	2786	12.0	2.0
Normal_93	1978	8.5	1.6
Normal_94	5060	21.7	2.6
Normal_95	8470	36.3	3.4
Normal_96	3549	15.2	2.2
Normal_97	2724	11.7	1.9
Normal_98	3576	15.3	2.2
Normal_99	1558	6.7	1.5
Normal_100	2356	10.1	1.8

Normal_101	5209	22.3	2.7
Normal_102	6065	26.0	2.9
Normal_103	2042	8.8	1.7
Normal_104	7297	31.3	3.2
Normal_105	5954	25.5	2.9
Normal_106	5527	23.7	2.7
Normal_107	7902	33.9	3.3
Normal_108	3140	13.5	2.1
Normal_109	1183	5.1	1.3
Normal_110	2652	11.4	1.9
Normal_111	6809	29.2	3.0
Normal_112	7218	31.0	3.1
Normal_113	5851	25.1	2.8
Normal_114	1663	7.1	1.5
Normal_115	1776	7.6	1.6
Normal_116	997	4.3	1.2
Normal_117	4625	19.8	2.5
Normal_118	3463	14.9	2.2
Normal_119	1715	7.4	1.5
Normal_120	1281	5.5	1.3
Normal_121	1589	6.8	1.5
Normal_122	8522	36.6	3.4
Normal_123	4469	19.2	2.5
Normal_124	5906	25.3	2.8
Normal_125	8611	36.9	3.4
Normal_126	3060	13.1	2.0
Normal_127	8488	36.4	3.4
Normal_128	9487	40.7	3.6
Normal_129	5873	25.2	2.8
Normal_130	3974	17.0	2.3
Normal_131	7066	30.3	3.1
Normal_132	2140	9.2	1.7
Normal_133	736	3.2	1.0
Normal_134	5133	22.0	2.6
Normal_135	4597	19.7	2.5
Normal_136	7534	32.3	3.2
Normal_137	6129	26.3	2.9

Appendix B

The Radius Ratio Distributions of the Three Groups of Nuclear Sections

Not all the cell nuclei from the mouse mammary gland are spherical. In fact, most of them are ellipsoids. The radius ratio of the cell nuclear sections from all the three classes of cryosections was evaluated with Image J, through the command "Analyze - Set Measurements - Fit Ellipse". This command measures the major and minor axes of the fitted ellipse in pixel, and the ratio between them is the radius ratio which represents the shape of the nuclear section. The results were summarized in the three charts below.

Although in principle it is possible to use plane probes to determine both the size and the shape of the objects, the precondition for this measurement, which is the shape of all the objects is the same, is not met with the nuclear sections examined in this work. Theoretically, a two-dimensional histogram of counts of both area and eccentricity parameters can be constructed to determine both the size and the shape distributions, but in this case it will result in a very sparse distribution of the bins which causes significant statistical error, making it also not feasible. Therefore, in this work, the cell nuclei were approximated as spheres, which is an appropriate descriptor with the given conditions.

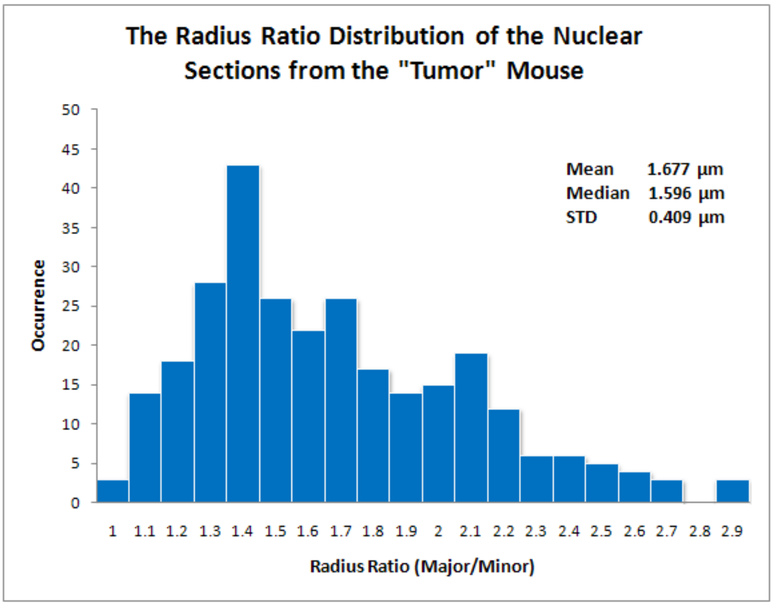

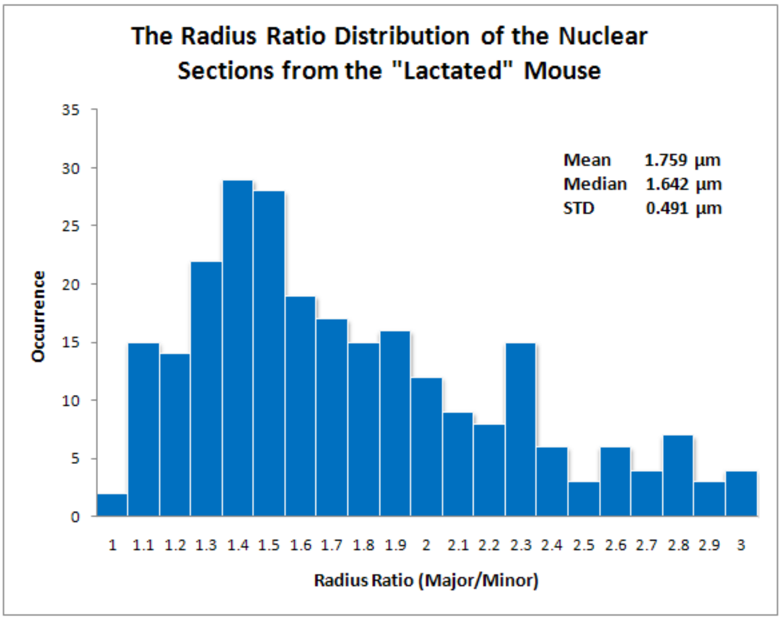
The Radius Ratio Distribution of the Nuclear Sections from the "Lactated" Mouse
Occurrence
35
30
25
20
15
10
5
0
Mean 1.759 µm
Median 1.642 µm
STD 0.491 µm
1
1.1
1.2
1.3
1.4
1.5
1.6
1.7
1.8
1.9
2
2.1
2.2
2.3
2.4
2.5
2.6
2.7
2.8
2.9
3
Radius Ratio (Major/Minor)

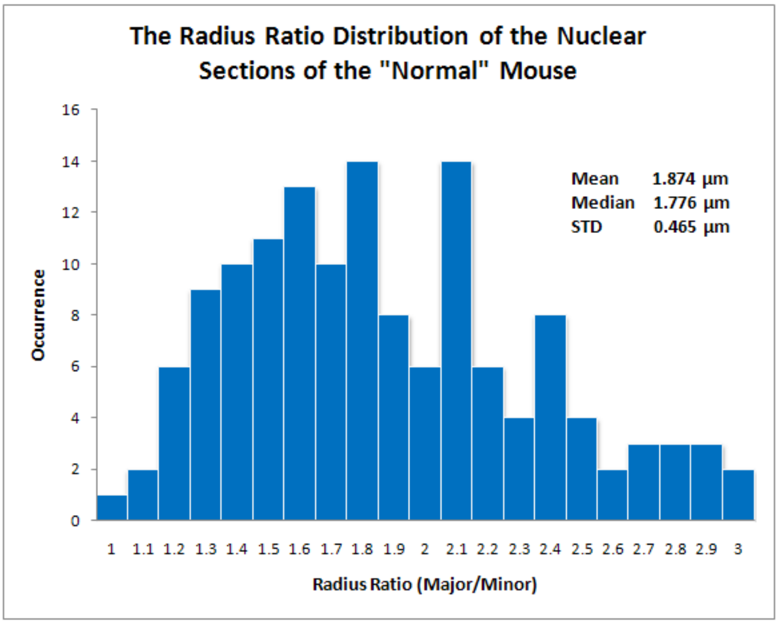
The Radius Ratio Distribution of the Nuclear Sections of the "Normal" Mouse
Occurrence
16
14
12
10
8
6
4
2
0
Mean 1.874 µm
Median 1.776 µm
STD 0.465 µm
1
1.1
1.2
1.3
1.4
1.5
1.6
1.7
1.8
1.9
2
2.1
2.2
2.3
2.4
2.5
2.6
2.7
2.8
2.9
3
Radius Ratio (Major/Minor)

Appendix C

SV40Tag Gene Vector Construction and Sequence

The pBS-Tag plasmid usd in this work for making probes for the *in situ* hybridisation was constructed by Dr. Anne Peaston from the Jackson Laboratory. The SV40Tag gene was ligated into pBlueScript (pBS) and the ligated product was transformed into DH5α *E.coli* bacteria. The plasmid is resistant to ampicillin.

Digesting the plasmid with Kpn1 and Xba1 restriction enzymes results in two bands on 1% agarose gel. The 2.9 kb band is the pBS vector and the 2.7 kb band is the SV40Tag gene. The sequence of the SV40Tag gene is from Genbank AF316141 strain H38 and confirmed in the pBS-Tag plasmid.

Sequence of the Tag gene (about 2.7kb):

```
GGATCCAGACATGATAAGATACATTGATGAGTTTGGACAAACCACAACTAGAATGCAGT
GAAAAAAATGCTTTATTTGTGAAATTTGTGATGCTATTGCTTTATTTGTAACCATTATA
AGCTGCAATAAACAAGTTAACAACAACAATTGCATTCATTTTATGTTTCAGGTTCAGGG
GGAGGTGTGGGAGGTTTTTTAAAGCAAGTAAAACCTCTACAAATGTGGTATGGCTGATT
ATGATCATGAACAGACTGTGAGGACTGAGGGGCCTGAAATGAGCCTTGGGACTGTGAAT
CAATGCCTGTTTCATGCCCTGAGTCTTCCATGTTCTTCTCCCCACCATCTTCATTTTTA
TCAGCATTTTCCTGGCTGTCTTCATCATCATCATCACTGTTTCTTAGCCAATCTAAAAC
TCCAATTCCCATAGCCACATTAAACTTCATTTTTTGATACACTGACAAACTAAACTCTT
TGTCCAATCTCTCTTTCCACTCCACAATTCTGCTCTGAATACTTTGAGCAAACTCAGCC
ACAGGTCTGTACCAAATTAACATAAGAAGCAAAGCAATGCCACTTTGAATTATTCTCTT
TTCTAACAAAAACTCACTGCGTTCCAGGCAATGCTTTAAATAATCTTTGGGCCTAAAAT
CTATTTGTTTTACAAATCTGGCCTGCAGTGTTTTAGGCACACTGTACTCATTCATGGTG
ACTATTCCAGGGGGAAATATTTGAGTTCTTTTATTTAGGTGTTTCTTTTCTAAGTTTAC
CTTAACACTGCCATCCAAATAATCCCTTAAATTGTCCAGGTTATTAATTCCCTGACCTG
AAGGCAAATCTCTGGACTCCCCTCCAGTGCCCTTTACATCCTCAAAAACTACTAAAAAC
TGGTCAATAGCTACTCCTAGCTCAAAGTTCAGCCTGTCCAAGGGCAAATTAACATTTAA
AGCTTTCCCCCCACATAATTCAAGCAAAGCAGCTGCTAATGTAGTTTTACCACTATCAA
TTGGTCCTTTAAACAGCCAGTATCTTTTTTTAGGAATGTTGTACACCATGCATTTTAAA
AAGTCATACACCACTGAATCCATTTTGGGCAACAAACAGTGTAGCCAAGCAACTCCAGC
CATCCATTCTTCTATGTCAGCAGAGCCTGTAGAACCAAACATTATATCCATCCTATCCA
AAAGATCATTAAATCTGTTTGTTAACATTTGTTCTCTAGTTAATTGTAGGCTATCAACC
CGCTTTTTAGCTAAAACAGTATCAACAGCCTGTTGGCATATGGTTTTTTGGTTTTTGCT
GTCAGCAAATATAGCAGCATTTGCATAATGCTTTTCATGGTACTTATAGTGGCTGGGCT
GTTCTTTTTTAATACATTTTAAACACATTTCAAAACTGTACTGAAATTCCAAGTACATC
CCAAGCAATAACAACACATCATCACATTTTGTTTCCATTGCATACTCTGTTACAAGCTT
CCAGGACACTTGTTTAGTTTCCTCTGCTTCTTCTGGATTAAAATCATGCTCCTTTAACC
CACCTGGCAAACTTTCCTCAATAACAGAAAATGGATCTCTAGTCAAGGCACTATACATC
AAATATTCCTTATTAACCCCTTTACAAATTAAAAAGCTAAAGGTACACAATTTTTGAGC
ATAGTTATTAATAGCAGACACTCTATGCCTGTGTGGAGTAAGAAAAAACAGTATGTTAT
GATTATAACTGTTATGCCTACTTATAAAGGTTACAGAATATTTTTCCATAATTTTCTTG
TATAGCAGTGCAGCTTTTTCCTTTGTGGTGTAAATAGCAAAGCAAGCAAGAGTTCTATT
ACTAAACACAGCATGACTCAAAAAACTTAGCAATTCTGAAGG:AAAGTCCTTGGGGTCT
TCTACCTTTCTCTTCTTTTTTGGAGGAGTAGAATGTTGAGAGTCAGCAGTAGCCTCATC
ATCACTAGATGGCATTTCTTCTGAGCAAAACAGGTTTTCCTCATTAAAGGCATTCCACC
ACTGCTCCCATTCATCAGTTCCATAGGTTGGAATCTAAAATCCACAAACAATTAGAATC
AGTAGTTTAACACATTATACACTTAAAAATTTTATATTTACCTTAGAGCTTTAAATCTC
TGTAGGTAGTTTGTCCAATTATGTCACACCACAGAAGTAAGGTTCCTTCACAAAGATCA
AGTCCAAACCACATTCTAAAGCAATCGAAGCAGTAGCAATCAACCCACACAAGTGGATC
TTTCCTGTATAATTTTCTATTTTCATGCTTCATCCTCAGTAAGCACAGCAAGCATATGC
AGTTAGCAGACATTTTCTTTGCACACTCAGGCCATTGTTTGCAGTACATTGCATCAACA
CCAGGATTTAAGGAAGAAGCAAATACCTCAGTTGCATCCCAGAAGCCTCCAAAGTCAGG
TTGATGAGCATATTTTACTCCATCTTCCATTTTCTTGTACAGAGTATTCATTTTCTTCA
TTTTTTCTTCATCTCCTCCTTTATCAGGATGAAACTCCTTGCATTTTTTTAAATATGCC
TTTCTCATCAGAGGAATATTCCCCCAGGCACTCCTTTCAAGACCTAGAAGGTCCATTAG
CTGCAAAGATTCCTCTCTGTTTAAAACTTTATCCATCTTTGCAAAGCTTTTTGCAAAAG
CCTAGGCCTC
```

Appendix D

Beads Preparation for Calibration Purpose

$100\,nm$ diameter red fluorescent beads (excitation wavelength $568\,nm$, Molecular Probes, Invitrogen) were used for calibrating the standing wave field of the SMI setup before the gene size measurement. The beads from the manufacturer need to be diluted to a rate which makes sure the signals are well separated and also enough beads are in the field of view to obtain good statistics. In this work the beads were diluted to 1:5000. Usually the beads are diluted in 100% ethanol, so they can be distributed more uniformly and dry faster.

Protocol:

1. Dilute $1\,\mu l$ $100\,nm$ red fluorescent beads into $499\,\mu l$ 100% ethanol. Mix thoroughly and place in an ultrasound bath for $10\,min$ to break up the clusters.
2. Add $10\,\mu l$ well-mixed solution from last step into $90\,\mu l$ 100% ethanol. Mix thoroughly and place in an ultrasound bath for another $10\,min$ to break up any clusters. Now the beads are diluted into 1:5000.
3. Pipette $5\,\mu l$ of the diluted beads solution onto the coverslip (the same type as used for the cell specimens) and spread with another coverslip.
4. Air dry at room temperature for about $5\,min$.
5. Mount on the slide using the same embedding medium as used for the cell specimens.

List of Abbreviations

- **FC**: fibrillar centre
- **DFC**: dense fibrillar component
- **GC**: granular component
- **NOR**: nucleolar organiser region
- **snRNP**: small nuclear ribonucleoprotein
- **snoRNP**: small nucleolar ribonucleoprotein
- **SMN**: survival of motor neuron
- **PML bodies**: promyelocytic leukaemia bodies
- **PNC**: perinucleolar compartment
- **FISH**: fluorescent in situ hybridisation
- **CT**: chromosome territory
- **GFP**: green fluorescent protein
- **DAPI**: 4,6-diamidino-2-phenylindole
- **FITC**: fluorescein isothiocyanate
- **WAP**: whey acidic protein
- **SV40**: Simian virus 40
- **Tag**: T antigen, large tumor antigen
- **DMEM**: Dulbecco's modified Eagle's medium
- **EDTA**: ethylenediaminetetraacetic acid
- **PBS**: phosphate buffered saline
- **D-PBS**: Dulbecco's phosphate buffered saline
- **HCl**: hydrogen chloride
- **SSC**: saline-sodium citrate
- **RNase**: ribonuclease
- **RT**: room temperature
- **MAA**: methanol and acetic acid
- **KCl**: potassium chloride
- **PSF**: point spread function
- **FWHM**: full width at half maximum
- **CLSM**: confocal laser scanning microscopy
- **PMT**: photomultiplier tube
- **NA**: numerical aperture
- **STED**: stimulated emission depletion microscopy
- **SMI**: spatially modulated illumination microscopy
- **CCD**: charge-coupled device
- **AID**: axial intensity distribution
- **CLT**: central limit theorem
- **ANOVA**: analysis of variance
- **CDF**: cumulative distribution function

- **PFA**: paraformaldehyde
- **EM**: electron microscope

List of Figures

1.1 **The major nuclear compartments of a mammalian cell nucleus.** The nucleus contains distinct compartments which are functionally organised. The nucleus is enclosed by the nuclear envelope, with nuclear pores inserted in it which serve in the transit of materials between the nucleus and cytoplasm. On the inner face of the nuclear envelope lies a meshwork of intermediate filaments called nuclear lamina. The chromatin in the interphase nucleus is organised into distinct chromosome territories. There are also a number of non-membrane bound compartments, also known as subnuclear bodies, including the nucleolus, Cajal bodies, PML bodies, nuclear speckles and others. The subnuclear bodies have all been reported with distinctive functions, which further proves that the nucleus is not a uniform mixture but organised into functional subdomains. . . 3

1.2 **Chromosome territories in the chicken cell nucleus.** a. 4,6-diamidino-2-phenylindole (DAPI)-stained, diploid, chicken metaphase spread with macro- and microchromosomes. b. The same metaphase spread after multicolour fluorescence *in situ* hybridisation with pseudocoloured chromosomes. Chicken chromosome paint probes (image courtesy of Johannes Wienberg) were labelled by a combinatorial scheme with oestradiol (1, 4, 5, 6), digoxigenin (2, 4, 6, Z) and biotin (3, 5, 6, Z). c. Oestradiol- and digoxigenin-labelled probes were detected using secondary antibodies labelled with Cy3 and fluorescein isothiocyanate (FITC); biotinylated probes were detected with Cy5-conjugated streptavidin. d. Mid-plane light optical section through a chicken fibroblast nucleus shows mutually exclusive chromosome territories (CTs) with homologous chromosomes seen in separate locations. (Note that only one of the two CTs for each of 4 and 6 is displayed in this section.) (Image courtesy of F. Habermann.) [29] 6

1.3 **24-colour 3D FISH representation and classification of chromosomes in a human G0 fibroblast nucleus.** A. deconvoluted mid-plane nuclear section recorded by wide-field microscopy in eight channels: one channel for DAPI (DNA counterstain) and seven channels for the following fluorochromes: diethylaminocoumarin (Deac), Spectrum Green (SG), and the cyanine dyes Cy3, Cy3.5, Cy5, Cy5.5, and Cy7. Each channel represents the painting of a CT subset with the respective fluorochrome. RGB images of the 24 differently labelled chromosome types (1–22, X, and Y) were produced by superposition of the seven channels (bottom right). (B) False colour representation of all CTs visible in this mid-section after classification with the program goldFISH. (C) 3D reconstruction of the complete CT arrangement in the nucleus viewed from different angles. (D) Simulation of a human fibroblast model nucleus according to the SCD model. The first image shows 46 statistically placed rods representing the 46 human chromatids. The next three images simulate the decondensation process and show the resulting CT arrangement obtained after different numbers of Monte Carlo relaxation steps (200, 1,000, and 400,000). [31] 7

2.1 **The transgenic mouse model. (a)** The construction of the mouse model. The hybrid gene composed of the WAP gene (a milk protein encoding gene) promoter and the SV40 Tag coding region was injected into the zygote of the C57BL/6J mouse. The SV40 Tag gene was transcribed during mid to late pregnancy and during lactation when the WAP gene promoter was activated. After several rounds of pregnancy and lactation, mammary abnormalities were observed and finally developed into papillary and then solid carcinoma. **(b)** The DNA FISH result of the SV40Tag gene in the cells derived from the transgenic mouse. The arrows indicate the SV40Tag gene loci which are located on chromosome 11 according to Giemsa banding. This image was provided by Dr. Anne Peaston in the Jackson Laboratory. 13

3.1 **Tokuyasu cryosectioning.** A. Cells or tissues go through chemical fixation, sucrose embedding and freezing in liquid nitrogen, before thin sections are cut by ultracryomicrotomy. Frozen sections are collected on sucrose drops, transferred to a solid support (glass coverslip or plastic coated metal grids). The sucrose will be washed away before labelling with antibodies or nucleic acid probes. The different cellular profiles present in a cryosection (along red lines: S1 − 4) originate from different cells in the tissue and represent the different parts of the nucleus. Pale yellow, cytoplasm; blue, nucleus; aqua, nucleoli; green, splicing speckles. B. Tokuyasu cryosections are obtained from cells fixed in conditions that preserve cell ultrastructure. HeLa cells were fixed as for cryosectioning, stained and Epon-embedded [96]; imaging by electron microscopy shows good preservation of membrane integrity, organelles (e.g. mitochondria) and nucleolus. Bar 500 nm. C. Thin cryosections provide optimal imaging condition for high resolution and contrast on fluorescence microscopes. 3D stacks were collected from whole HeLa cells or cryosections stained with TOTO-3, a nucleic acid dye. The images are adapted from [98]. 16

5.1 **Schematic show of the light path of the epifluorescence microscope.** [111] 28

5.2 **Image formation in a confocal microscope (XZ slice).** The PSF weighted with the amplitude of the object at every point forms the image of the object. (Wikipedia) 29

5.3 **Airy patterns and the limit of resolution.** [117] 29

5.4 **The light path of the confocal laser scanning microscope.**[114] 31

5.5 **Experimental setup of the SMI microscope. (a)** The sample is positioned between the two objectives (OL1, OL2) using a 3-axis (x,y,z) stepper motor stage for coarse movements and a 2-axis (y,z) piezo stage for fine control and object scanning. The fluorescence from the sample is collected by the right hand objective (OL1) and imaged on the CCD camera. [130] **(b)** Two laser beams propagate in opposite directions and interfere in the optical axial direction between the two opposing objectives, creating a standing wave field with intensity modulation along the optical axis. 33

5.6 **Scheme of the extraction of the modulation contrast R.** The modulation contrast R is equal to the ratio of the amplitude of the inner and outer envelope (dashed line) of the AID (solid line), from which the axial object size can be calculated. [136] 34

5.7 **Relationship between object diameter and modulation depth for a spherical object.** This simulation assums a refractive index of 1.47, complete interference and an angle of 0° between the two laser beams. The modulation depth decreases monotonically with increasing object size up to around 240nm, after which a low amplitude ringing is seen. In the region from 40nm to around 200nm, this relationship is one to one and can be inverted to obtain a mapping from measured object modulation depth to object size. [137] 34

6.1 **Sectioning features in a three dimensional space with a place.** The area intersection with a volume (red), the line intersection with a surface (blue) and the point intersection with a linear feature (green) are shown. [106] 36

6.2 **Probe construction.** A grid of lines is superimposed on a plane section through the microstructure, and the interactions of the probes with features of interest in the sample will be noted and counted. [106] 38

6.3 **Different size circles can be generated by sectioning of a sphere.** [106] 39

6.4 **Schematic show of how to obtain the frequency (f) of sections whose radius falls into $[r_i, r_{i+1}]$ in a sphere with radius R.** [107] 40

8.1 **Nucleus staining (DAPI) of mouse mammary gland tissue sections**. **(a)** Part of a paraformaldehyde (PFA) fixed paraffin embedded mouse mammary gland tissue section. The image is from [139]; **(b)** Part of a PFA fixed thin cryosection (200 nm in thickness) from the normal mammary gland of the transgenic mouse which has been through 5 rounds of pregnancy and lactation. The image was taken in the Nikon Imaging Center in Heidelberg with Nikon C1Si-CLEM spectral imaging confocal laser scanning system, with NA1.4 60x oil immersion objective. Scale bar: 5 μm. Not only the nuclear structure was preserved using cryosections, the resolution has also been enhanced due to sectioning. The basic features of genome organisation (nuclear envelope, heterochromatin, euchromatin, chromocenters) can be clearly recognized in the cryosection (b), whereas it is all blurred in the paraffin-embedded section (a). **(c)** and **(d)** are the zooming in of the selected area in (a) and (b), respectively. From Figure (d), one can see the chromatin are not evenly distributed in the nucleus. The tightly packed heterochromatin is intensely stained and gathers mainly at the periphery of the nucleus. The less compacted euchromatin stains lighter and occupies the rest of the nuclear space. The bright points are densely stained chromatin called chromocenters, which are aggregation of heterochromatin containing telomeric DNA and telomerase activity. The scale bar in (d) is 5 μm. 48

9.1 **The 3D nuclear radius distributions and the summary of the basic statistics of the three cases.** The average nuclear radii in the cases of “lactated” and “tumor” are smaller than that of the “normal” case, and the three size distributions are statistically different. The distribution of the radii of the “tumor” case is much wider than the other two, which indicates the loss of growth control of tumor cells. 54

9.2 **The nuclear volume distributions of the three cell populations.** The table below lists the equivalent average nuclear volumes based on the average nuclear radii. The differences among the three distributions are statistically significant as revealed by ANOVA test ($p < 0.0001$). 55

10.1 **Whole chromosome painting results of chromosome 11 with the mammary gland cryosection from the “lactated” mouse.** **(a)** The nuclei were counterstained with DAPI. The staining shows the basic chromatin organisation, which is heterochromatin gathers mainly at the periphery of the nucleus and euchromatin more at the interior of the nucleus. Chromocenters (aggregations of heterochromatin) are brightly stained. **(b)** Chromosome 11 which were labelled by the Cy3 conjugated chromosome 11 painting probe. **(c)** The merge of the two channels. Not all the nuclei in this plane have chromosome 11 signals but about one third of them, which is reasonable concerning the sectioning process. The images were taken in the Nikon Imaging Center in Heidelberg with Nikon C1Si-CLEM spectral imaging confocal laser scanning system, with NA1.4 60x oil immersion objective. Scale bar: 5 μm. 60

11.1 **The cell used for the demonstration of the segmentation process.** A cell from the mammary gland tissue cryosection of lactated mouse is shown here. The nucleus was counterstained with DAPI and the chromosome 11 in this section was labelled with Cy3. The images were taken in the Nikon Imaging Center in Heidelberg with Nikon C1Si-CLEM spectral imaging confocal laser scanning system, with NA1.4 60x oil immersion objective. Scale bar: $1\,\mu m$. . . 62

11.2 **The segmentation process of the chromosome territory and the nucleus.** The threshold value for the chromosome territory (a) was manually defined to make sure that the entire chromosome territory was selected but not the blurring and the nuclear background, which resulted in the binary image shown in b. The segmentation for the nucleus (c) was more complicated due to the unevenly distribution nature of the chromatin. The first step was to set a threshold which ensured the proper selection of the nuclear boundary (d), then an additional step was applied, which was done by “Image J - Process - Binary - Fill Holes”. The selected “hole” area which are sets of “1” values were converted to “0”s and combined with the original image by this operation, then the whole nucleus was properly converted to a binary image (e). 63

11.3 **The segmentation result.** After separate segmentation of the chromosome and the nucleus, the binary images were merged by “Image J - Image - Color - RGB Merge” to give the left image, which will be used as masks for the original image (right) in various measurements afterwards. 64

11.4 **Dividing the nuclear profile into concentric shells.** The matlab script calculated the axial position of the section and divided the nucleus into concentric shells according to it. The shape of the shells was adjusted by the shape of the original nucleus. The pixel numbers of both channels were measured and used as the base of calculation for chromosome volume and radial position. 65

11.5 **The distributions of chromosome 11 volumes.** The exact values (volumes) at the two ends of the distributions are marked besides the data series. 66

11.6 **The plots of the cumulative distribution function (CDF) for the chromosome 11 volume data in Figure 11.5.** The differences among the distributions are statistically significant at the 5% level, as revealed by Kolmogorov-Smirnov test. 68

12.1 **The comparison of 3D nuclear radial positions of chromosome 11 during tumorigenesis.** 74

12.2 **Sizes and gene densities of mouse chromosomes.** The bars indicate the genomic sizes of the chromosomes. The distance of the square to the x-axis is scaled according to the gene density of each chromosome, with the value highlighted inside the square. The gene density is expressed as genes/Mbp. The source data are listed in the table below, which are the exact chromosome size and gene density of each chromosome of the mouse karyotype. For a diploid cell from the female C57BL/6J mouse, the total length of all the chromosomes is about $5280\,Mbp$, from which 4.62% is chromosome 11. The data is based on the NCBI Build 37.1 (the latest) mouse assembly (April 2007, strain C57BL/6J) [146]. 75

13.1 **The co-hybridisation results of SV40Tag and chromosome 11. (a)** Part of the mouse mammary tumor cryosection. The nuclei are visible due to green autofluorescence. The chromosome 11 territories were labelled with Cy3-conjugated DNA probes (purchased from Cambio, UK) and the SV40Tag gene was labelled with Alexa488-conjugated probes made by nick translation. The white arrows point out several typical nuclear profiles, including nuclei with both the chromosome painting signal and the SV40Tag gene signal which locates at the nuclear periphery, nucleus with one chromosome painting signal and nucleus with two chromosome painting signals. The image was taken in the Nikon Imaging Center at University Heidelberg, with an Nikon Eclipse 90i upright automated epifluorescence microscope, and the image has been adjusted in brightness and contrast for demonstration purpose. Scale bar: $10\,\mu m$. **(b) (c) (d) (e)** are individual nuclear profiles from the same cryosection, which shows the four typical co-hybridisation results: with the chromosome painting signal and two SV40 gene signals (arrows), with the chromosome painting signal and one SV40 gene signal which loops out of the chromosome territory (arrow), with only the chromosome painting signal (one chromosome) and with two chromosome painting signals, respectively. 78

14.1 **A screenshot of the interactive data viewer (the “sviewer”) when analysing the SV40Tag gene locus.** The x-y, x-z and y-z sections of the object image were displayed, where a typical modulation pattern in the z direction can be observed. Also the fit curve of the axial intensity distribution and the fitted parameters have been shown. 83

14.2 **The major chromatin structures during chromosome condensation.** The lowest level of organisation is the nucleosome, where two superhelical turns of DNA (a total of 165 base pairs) are wound around the outside of a histone octamer. Nucleosomes are connected to one another by short stretches of linker DNA and this is called the “beads-on-a-string” structure. The diameter of the string is about $11\,nm$. At the next level of organisation the string of nucleosomes coils into a fibre which is about $30\,nm$ in diameter, and these fibres are then further folded into higher-order structures. At levels of structure beyond the nucleosome the details of folding are still uncertain. [158] 84

14.3 **Simulation of 2700 *bp* bare DNA doing random walk in a relatively restricted nuclear space using the worm-like chain model.** The upper image is a typical structure of this simulation (axes in nanometer) and the lower one shows the measured size distribution of the structure after 100 times random repeats. The measured mean size of the structure is 119 *nm* with a standard deviation of 24 *nm*. (The simulation was carried out by David Baddeley.) 86

14.4 **Simulation of the SV40Tag gene (2700 *bp*) in the 30 *nm* fibre state using the worm-like chain model.** Knowing the "gene density" of the 30 *nm* fibre state is 105 *bp*/*nm*, the 30 *nm* chromatin polymer formed by 2700 *bp* DNA is about 26 *nm* in length, which is unlikely to be further compacted in the higher order chromatin condensation process. The axes are in nanometer. (The simulation was carried out by David Baddeley.) 87

14.5 **The definition of full width at half maximum (FWHM).** It is an expression of the extent of a function, which is given by the distance between points on the function at which the function reaches half its maximum value. (Wikipedia) 87

14.6 **The analysis output of a 100nm beads sample evaluated by the *sviewer* package.** The image of the beads was taken at 568 *nm* excitation and it was the maximum intensity projection of the image stack along the z-axis (upper panel, left), accompanying with the colour coded representation of the size estimation (upper panel, right). In the colour map black means the object is larger than about 230 *nm* which is too large for a fit and purple means the signal to noise ratio of the image is too low for that. In the lower panel is the size distribution of the measured beads and some basic statistics. Note that the measured diameter of the beads sample is 94.58 ± 10.29 *nm* which is in good agreement with the manufacturer stated size and shows the high reproducibility and precision of SMI size measurement. 89

14.7 **A mouse fibroblast cell nucleus (C57SV cell line) recorded with SMI microscopy.** The image stack was acquired using the standard SMI setup in the lab equipped with 100×, NA1.4 oil immersion objectives from the Leica Microsystems, at excitation wavelength 568 *nm*, taking optical sections with an axial step size of 40 *nm*. The image presented is the maximum intensity z-projection of the image stack. The nucleus was visible due to low-level autofluorescence and the SV40Tag gene was labelled with Alexa 568 conjugated FISH probe. 90

14.8 **The analysis output of the SV40Tag gene loci in the cell of Figure 14.7 obtained by the *sviewer* package.** The image of the gene loci and the corresponding colour map of the size estimation are shown, together with the basic statistics of two size parameters, though what is more important for the final analysis is the individual size of every gene locus (not displayed here). 90

14.9 **The crucial steps in data evaluation.** (a) shows the result of the command "`ofind3`". A single gene locus was identified by the multi-thresholding method. The sensitivity of the object detection can be changed manually. (b) The identified locus was analysed by the automated fitting procedure named "`dofits`". The modulation depth can be calculated from the fitting curve, which was then interpolated into the calibration curve (Figure 5.7) by Matlab to extract the size value. In this case, the fitted size of the gene locus was 115.03 nm. . 91

14.10 **The size distribution of the SV40Tag gene loci measured by SMI microscopy.** 84 gene loci were evaluated and the mean size is 93.4 nm with a standard deviation of 25.0 nm. 91

14.11 **The multi-point model. Left:** The object is approximated by a small number of discrete points (10 points are used here) which are convolved with the microscope PSF to give the image. The lateral and axial PSFs can be determined by calibration objects like fluorescent beads. **Right:** The mean distance of the fitted points to the object centre is taken as the size parameter which can be transformed into the FWHM of a matching Gaussian. [162] 92

14.12 **Using the multi-point model to evaluate the SV40Tag gene size.** Two methanol and acetic acid fixed mouse fibroblast cells (C57SV cell line) are shown in the upper panel. The image was acquired with a Leica TCS NT Confocal Laser Scanning Microscope (CLSM) equipped with a PlanApo 63x, NA= 1.4 oil immersion objective. The image presents the maximum intensity z-projection of the image stack taken through the optical axis with an axial step size of 203nm. The nucleus was counterstained with To-Pro-3 iodide and the SV40Tag gene was labelled with Alexa 568 conjugated FISH probe. The lower panel is the SV40Tag gene loci images (left) and the corresponding 10 points fit (right). All the parameters needed for the gene size and shape estimation are listed. 93

14.13 **The size distribution of the SV40Tag gene loci measured with confocal microscopy.** 72 gene loci were evaluated and the mean size is 283.8 nm with a standard deviation of 51.6 nm. 94

14.14 **The comparison of the size distribution of the SV40Tag gene loci measured with SMI and Confocal microscopy.** The distribution of SMI measured sizes is much narrower than that of confocal microscopy (standard deviation 25.0 nm and 51.6 nm, for SMI and confocal microscopy, respectively), revealing the significant measuring precision enhancement with SMI microscopy. 96

Acknowledgement

I would like to thank my supervisor, Prof. Christoph Cremer, for giving me this opportunity to explore the unique field of biophysics, and also for the help, support and trust he gave me during this work.

This thesis would not have been possible without the help of Dr. Anne Peaston, who didn't only initialize this project with us, but also have provided important materials and inspiring suggestions all the time. I am most grateful to Dr. Ana Pombo and Dr. Miguel Branco, for their kind support regarding to the cryo-FISH technique and the relative data analysis. I also would like to thank Prof. Stefan Wölfl and Prof. Harald Herrmann-Lerdon for their valuable advices in the TAC meetings.

I owe my deepest gratitude to my beloved husband, Hongwei Zhang, and my dear parents, for the continuous love they gave me all the way in my life. They have been with me through all the difficulties during this time like they always did. Without their support and encouragements none of this would have been possible.

I am indebted to Dr. Claudia Batram and Dr. Thibaud Jegou who helped me with the experiments at the very beginning of my work, and Dr. David Baddeley for his detailed instruction of the data analysis software. I thank Patrick Müller and Yanina Weiland for the useful discussions during the experiments, and Dr. Roman Amberger, Dr. Paul Lemmer, Manuel Gunkel and Gerrit Best for their help regarding microscopy and data analysis. I am grateful to Prof. Victor Sourjik and Hui Li in the Sourjik lab for their kind support during the probe preparation and their valuable suggestions for my work. I also would like to thank all the former and current members of the Cremer group, with some of them I have already mentioned, for their help and the enjoyable time we shared together.

I thank Ms. Rosemarie Eidsness and Mrs. Margund Bach for their kindness, help and encouragements during my work.

I especially would like to thank the Athenaeum Foundation and the Cremer group for financial support.

Last, but by no means least, I thank all my friends here in Germany and those who are far far away in China, for their love and support all the time.

Bibliography

[1] Lanctôt C, Cheutin T, Cremer M, Cavalli G, Cremer T. (2007) Dynamic genome architecture in the nuclear space: regulation of gene expression in three dimensions. Nat Rev Genet. 8(2):104-115.

[2] Stoffler, D., Fahrenkrog, B. and Aebi, U. (1999) The nuclear pore complex: from molecular architecture to functional dynamics. Curr. Opin. Cell Biol. 11: 391-401.

[3] Sexton, T., Schober, H., Fraser, P. and Gasser, S. M. (2007) Gene regulation through nuclear organization. Nature Struct. Mol. Biol. 14: 1049-1055.

[4] Joanna M. Bridger, Nicole Foeger, Ian R. Kill and Harald Herrmann. (2007) The Nuclear Lamina: both a structural framework and a platform for genome organization. FEBS Journal 274: 1354-1361.

[5] Wiesel N, Mattout A, Melcer S, Melamed-Book N, Herrmann H, Medalia O, Aebi U, Gruenbaum Y. (2008) Laminopathic mutations interfere with the assembly, localization, and dynamics of nuclear lamins. Proc Natl Acad Sci USA. 105(1):180-185.

[6] Taddei, A., Hediger, F., Neumann, F.R. & Gasser, S.M. (2004) The function of nuclear architecture: a genetic approach. Annu. Rev. Genet. 38: 305-345.

[7] Ye, Q., Callebaut, I., Pezhman, A., Courvalin, J.C. & Worman, H.J. (1997) Domain-specific interactions of human HP1-type chromodomain proteins and inner nuclear membrane protein LBR. J. Biol. Chem. 272: 14983-14989.

[8] Shumaker, D.K. et al. (2006) Mutant nuclear lamin A leads to progressive alterations of epigenetic control in premature aging. Proc. Natl. Acad. Sci. USA 103: 8703-8708.

[9] Malhas, A., Lee, C.F., Sanders, R., Saunders, N.J. & Vaux, D.J. (2007) Defects in lamin B1 expression or processing affect interphase chromosome position and gene expression. J. Cell Biol. 176: 593-603.

[10] Gilbert, N., Gilchrist, S. & Bickmore, W.A. (2005) Chromatin organization in the mammalian nucleus. Int. Rev. Cytol. 242: 283-336.

[11] Spector, D. L. (1993) Macromolecular domains within the cell nucleus. Annu. Rev. Cell Biol. 9: 265-315.

[12] Weipoltshammer K, Schofer C, Almeder M, Philimonenko VV, Frei K, Wachtler F, Hozak P. (1999) Intranuclear anchoring of repetitive DNA sequences: centromeres, telomeres, and ribosomal DNA. J Cell Biol 147:1409-1418.

[13] Sullivan GJ, Bridger JM, Cuthbert AP, Newbold RF, Bickmore WA, McStay B. (2001) Human acrocentric chromosomes with transcriptionally silent nucleolar organizer regions associate with nucleoli. EMBO J 20:2867-2874.

[14] Miroslav Dundr and Tom Misteli. (2001) Functional architecture in the cell nucleus. Biochem. J. 356: 297-310.

[15] Gall, J. G. (2000) Cajal bodies: the first 100 years. Annu. Rev. Cell Dev. Biol. 16: 273-300.

[16] Matera, A. G. (1999) Nuclear bodies: multifaceted subdomains of the interchromatin space. Trends Cell Biol. 9: 302-309.

[17] Maul, G. G., Negorev, D., Bell, P. and Ishov, A. M. (2000) Review: properties and assembly mechanisms of ND10, PML bodies, or PODs. J. Struct. Biol. 129:278-287.

[18] Schul, W., Groenhout, B., Koberna, K., Takagaki, Y., Jenny, A., Manders, E. M., Raska, I., van Driel, R. and de Jong, L. (1996) The RNA 3' cleavage factors CstF 64 kDa and CPSF 100 kDa are concentrated in nuclear domains closely associated with coiled bodies and newly synthesized RNA. EMBO J. 15: 2883-2892.

[19] D.L. Spector. (2001) Nuclear domains. J. Cell Sci. 114: 2891-2893.

[20] Lamond AI, Spector DL. (2003) Nuclear speckles: a model for nuclear organelles. Nat. Rev. Mol. Cell Biol. 4 (8): 605-12.

[21] Korie E. Handwerger and Joseph G. Gall. (2006). Subnuclear organelles: new insights into form and function. TRENDS in Cell Biology 16 (1): 19-26.

[22] Pombo A, Cuello P, Schul W, Yoon J, Roeder R, Cook P, Murphy S. (1998) Regional and temporal specialization in the nucleus: a transcriptionally active nuclear domain rich in PTF, Oct1 and PIKA antigens associates with specific chromosomes early in the cell cycle. EMBO J 17 (6): 1768-1778.

[23] Saurin, A. J., Shiels, C., Williamson, J., Satijn, D. P., Otte, A. P., Sheer, D. and Freemont, P. S. (1998) The human polycomb group complex associates with pericentromeric heterochromatin to form a novel nuclear domain. J. Cell Biol. 142: 887-898.

[24] Huang, S. (2000) Review: perinucleolar structures. J. Struct. Biol. 129: 233-240.

[25] C. Cremer, C. Zorn, T. Cremer. (1974) An ultraviolet laser microbeam for 257 nm. Microsc. Acta 75: 331-337.

[26] C. Zorn, T. Cremer, C. Cremer, J. Zimmer. (1976) Laser-uv-micro-irradiation of interphase nuclei and posttreatment with caffeine: A new approach to establish the arrangement of interphase chromosomes. Hum. Genet. 35: 83-89.

[27] Lichter P, Cremer T, Tang CJ, Watkins PC, Manuelidis L, Ward DC. (1988) Rapid detection of human chromosome 21 aberrations by in situ hybridization. Proc Natl Acad Sci USA 85: 9664-9668.

[28] Cremer T, Lichter P, Borden J, Ward DC, Manuelidis L. (1988) Detection of chromosome aberrations in metaphase and interphase tumor cells by in situ hybridization using chromosome-specific library probes. Hum Genet 80:235-246.

[29] Cremer T, Cremer C. (2001) Chromosome territories, nuclear architecture and gene regulation in mammalian cells. Nat Rev Genet 2:292-301.

[30] Branco MR, Pombo A. (2006) Intermingling of chromosome territories in interphase suggests role in translocations and transcription-dependent associations. PLoS Biol 4(5): e138. DOI: 10.1371/journal.pbio.0040138.

[31] Bolzer A, Kreth G, Solovei I, Koehler D, Saracoglu K, et al. (2005) Three-dimensional maps of all chromosomes in human male fibroblast nuclei and prometaphase rosettes. PLoS Biol 3(5): e157. DOI: 10.1371/journal.pbio.0030157.

[32] Robinett CC, Straight A, Li G, Willhelm C, Sudlow G, Murray A, Belmont AS. (1996) In vivo localization of DNA sequences and visualization of large-scale chromatin organization using lac operator/repressor recognition. J Cell Biol 135:1685-1700.

[33] Belmont AS, Straight AF. (1998) In vivo visualization of chromosomes using lac operator-repressor binding. Trends Cell Biol 8:121-124.

[34] Zink, D. et al. (1998) Structure and dynamics of human interphase chromosome territories in vivo. Hum. Genet. 102: 241-251.

[35] Manders, E. M., Kimura, H. & Cook, P. R. (1999) Direct imaging of DNA in living cells reveals the dynamics of chromosome formation. J. Cell Biol. 144: 813-821.

[36] Cremer, T., Kreth, G., Koester, H., Fink, R.H.A., Heintzmann, R., Cremer, M., Solovei, I., Zink, D., Cremer, C. (2000) Chromosome territories, interchromatin domain compartment, and nuclear matrix: an integrated view of the functional nuclear architecture. Crit. Rev. Eukaryot. Gene Expr. 12 (2): 179-212.

[37] Dillon, N., and Festenstein, R. (2002) Unravelling heterochromatin: competition between positive and negative factors regulates accessibility. Trends Genet. 18: 252-258.

[38] Cheutin, T., Gorski, S.A., May, K.M., Singh, P.B., and Misteli, T. (2004) In vivo dynamics of Swi6 in yeast: Evidence for a stochastic model of heterochromatin. Mol. Cell. Biol. 24: 3157-3167.

[39] Cheutin, T., McNairn, A.J., Jenuwein, T., Gilbert, D.M., Singh, P.B., and Misteli, T. (2003) Maintenance of stable heterochromatin domains by dynamic HP1 binding. Science 299: 721-725.

[40] Festenstein, R., Pagakis, S.N., Hiragami, K., Lyon, D., Verreault, A., Sekkali, B., and Kioussis, D. (2003) Modulation of heterochromatin protein 1 dynamics in primary Mammalian cells. Science 299: 719-721.

[41] Tom Misteli. (2007) Beyond the Sequence: Cellular Organization of Genome Function. Cell 128: 787-800.

[42] Ye, Q., Hu, Y. F., Zhong, H., Nye, A. C., Belmont, A. S. and Li, R. (2001) BRCA1-induced large-scale chromatin unfolding and allele-specific effects of cancer-predisposing mutations. J. Cell Biol. 155: 911-921.

[43] Nye, A. C., Rajendran, R. R., Stenoien, D. L., Mancini, M. A., Katzenellenbogen, B. S. and Belmont, A. S. (2002) Alteration of largescale chromatin structure by estrogen receptor. Mol. Cell. Biol. 22: 3437-3449.

[44] Dietzel S, Zolghadr K, Hepperger C, Belmont AS. (2004) Differential large-scale chromatin compaction and intranuclear positioning of transcribed versus non-transcribed transgene arrays containing beta-globin regulatory sequences. J Cell Sci. 117: 4603-14.

[45] Chubb, J.R., and Bickmore, W.A. (2003) Considering nuclear compartmentalization in the light of nuclear dynamics. Cell 112: 403-406.

[46] Cremer, T., Cremer, M., Dietzel, S., Muller, S., Solovei, I., and Fakan, S. (2006) Chromosome territories - a functional nuclear landscape. Curr. Opin. Cell Biol. 18: 307-316.

[47] van Driel, R., Fransz, P.F., and Verschure, P.J. (2003) The eukaryotic genome: a system regulated at different hierarchical levels. J. Cell Sci. 116: 4067-4075.

[48] Fraser, P. (2006) Transcriptional control thrown for a loop. Curr. Opin. Genet. Dev. 16: 490-495.

[49] Volpi, E.V., Chevret, E., Jones, T., Vatcheva, R., Williamson, J., Beck, S., Campbell, R.D., Goldsworthy, M., Powis, S.H., Ragoussis, J., et al. (2000) Large-scale chromatin organization of the major histocompatibility complex and other regions of human chromosome 6 and its response to interferon in interphase nuclei. J. Cell Sci. 113: 1565-1576.

[50] Williams, R.R., Broad, S., Sheer, D., and Ragoussis, J. (2002) Subchromosomal positioning of the epidermal differentiation complex (EDC) in keratinocyte and lymphoblast interphase nuclei. Exp. Cell Res. 272: 163-175.

[51] Chambeyron, S., and Bickmore, W.A. (2004) Chromatin decondensation and nuclear reorganization of the HoxB locus upon induction of transcription. Genes Dev. 18: 1119-1130.

[52] Palstra, R.J., Tolhuis, B., Splinter, E., Nijmeijer, R., Grosveld, F., and de Laat, W. (2003) The beta-globin nuclear compartment in development and erythroid differentiation. Nat. Genet. 35: 190-194.

[53] Murrell, A., Heeson, S., and Reik, W. (2004) Interaction between differentially methylated regions partitions the imprinted genes Igf2 and H19 into parent-specific chromatin loops. Nat. Genet. 36: 889-893.

[54] Ferreira, J., Paolella, G., Ramos, C., and Lamond, A.I. (1997) Spatial organization of large-scale chromatin domains in the nucleus: A magnified view of single chromosome territories. J. Cell Biol. 139, 1597-1610.

[55] Sadoni, N., Langer, S., Fauth, C., Bernardi, G., Cremer, T., Turner, B.M., and Zink, D. (1999) Nuclear organization of mammalian genomes. Polar chromosome territories build up functionally distinct higher order compartments. J. Cell Biol. 146: 1211-1226.

[56] Croft JA, Bridger JM, Boyle S, Perry P, Teague P, Bickmore WA. (1999) Differences in the localization and morphology of chromosomes in the human nucleus. J Cell Biol 145:1119-1131.

[57] Morton, N.E. (1991) Parameters of the human genome. Proc. Natl. Acad. Sci. USA. 88:7474-7476.

[58] Cremer M, Kupper K, Wagler B, Wizelman L, von Hase J, Weiland Y, Kreja L, Diebold J, Speicher MR, Cremer T. (2003) Inheritance of gene density-related higher order chromatin arrangements in normal and tumor cell nuclei. J Cell Biol 162: 809-820.

[59] Boyle S, Gilchrist S, Bridger JM, Mahy NL, Ellis JA, Bickmore WA. (2001) The spatial organization of human chromosomes within the nuclei of normal and emerin-mutant cells. Hum Mol Genet 10:211-219.

[60] Tanabe H, Muller S, Neusser M, von Hase J, Calcagno E, Cremer M, Solovei I, Cremer C, Cremer T. (2002a) Evolutionary conservation of chromosome territory arrangements in cell nuclei from higher primates. Proc Natl Acad Sci USA 99:4424-4429.

[61] Tanabe H, Kupper K, Ishida T, Neusser M, Mizusawa H. (2005) Inter- and intra-specific gene-density-correlated radial chromosome territory arrangements are conserved in Old World monkeys. Cytogenet Genome Res 108:255-261.

[62] Habermann FA, Cremer M, Walter J, Kreth G, von Hase J, Bauer K, Wienberg J, Cremer C, Cremer T, Solovei I. (2001) Arrangements of macro- and microchromosomes in chicken cells. Chromosome Res 9:569-584.

[63] Tanabe H, Habermann FA, Solovei I, Cremer M, Cremer T. (2002b) Non-random radial arrangements of interphase chromosome territories: evolutionary considerations and functional implications. Mutat Res 504:37-45.

[64] Sun HB, Shen J, Yokota H. (2000) Size-dependent positioning of human chromosomes in interphase nuclei. Biophys J 79:184-190.

[65] Emmerich P, Loos P, Jauch A et al. (1989) Double in situ hybridization in combination with digital image analysis: a new approach to study interphase chromosome topography. Exp Cell Res 181: 126-140.

[66] Popp S, Scholl HP, Loos P et al. (1990) Distribution of chromosome 12 and

X centric heterochromatin in the interphase nucleus of cultured human cells. Exp Cell Res 189: 1-12.

[67] Höfers C, Baumann P, Hummer G, Jovin T, Arndt-Jovin D. (1993) The localization of chromosome domains in human interphase nuclei. Three-dimensional distance determinations of fluorescence in situ hybridization signals from confocal laser scanning microscopy. Bioimaging 1: 96-106.

[68] Cremer M, von Hase J, Volm T, Brero A, Kreth G, Walter J, Fischer C, Solovei I, Cremer C, Cremer T. (2001) Non-random radial higher-order chromatin arrangements in nuclei of diploid human cells. Chromosome Res 9:541-567.

[69] Habermann FA, Cremer M, Walter J, Kreth G, von Hase J, Bauer K, Wienberg J, Cremer C, Cremer T, Solovei I. (2001) Arrangements of macro- and microchromosomes in chicken cells. Chromosome Res 9:569-584.

[70] Meaburn K. (2005) The role of nuclear architecture in genomic stability. PhD thesis, Brunel University.

[71] Bridger JM, Boyle S, Kill IR, Bickmore WA. (2000) Re-modelling of nuclear architecture in quiescent and senescent human fibroblasts. Curr Biol 10: 149-152.

[72] Kosak, S.T. et al. (2002) Subnuclear compartmentalization of immunoglobulin loci during lymphocyte development. Science 296: 158-162.

[73] Williams, R.R. et al. (2006) Neural induction promotes large-scale chromatin reorganisation of the Mash1 locus. J. Cell Sci. 119: 132-140.

[74] Chuang, C.H. et al. (2006) Long-range directional movement of an interphase chromosome site. Curr. Biol. 16: 825-831.

[75] Hewitt, S.L., High, F.A., Reiner, S.L., Fisher, A.G. and Merkenschlager, M. (2004) Nuclear repositioning marks the selective exclusion of lineage-inappropriate transcription factor loci during T helper cell differentiation. Eur. J. Immunol. 34: 3604-3613.

[76] Ragoczy, T., Bender, M.A., Telling, A., Byron, R. and Groudine,M. (2006) The locus control region is required for association of the murine beta-globin locus with engaged transcription factories during erythroid maturation. Genes Dev. 20: 1447-1457.

[77] Taddei, A. et al. (2006) Nuclear pore association confers optimal expression levels for an inducible yeast gene. Nature 441: 774-778.

[78] Cabal, G.G. et al. (2006) SAGA interacting factors confine sub-diffusion of transcribed genes to the nuclear envelope. Nature 441: 770-773.

[79] Dieppois, G., Iglesias, N. and Stutz, F. (2006) Cotranscriptional recruitment to the mRNA export receptor Mex67p contributes to nuclear pore anchoring of activated genes. Mol. Cell. Biol. 26: 7858-7870.

[80] Keenan, S.J., J. Diamond, W.G. McCluggage, H. Bharucha, D. Thompson, P.H. Bartels, and P.W. Hamilton. (2000) An automated machine vision system for the histological grading of cervical intraepithelial neoplasia (CIN). J. Pathol. 192: 351-362.

[81] Parada LA, McQueen PG, Munson PJ, Misteli T. (2002) Conservation of relative chromosome positioning in normal and cancer cells. Curr Biol 12: 1692-1697.

[82] Cremer M, Kupper K, Wagler B, Wizelman L, von Hase J, Weiland Y, Kreja L, Diebold J, Speicher MR, Cremer T. (2003) Inheritance of gene density-related higher order chromatin arrangements in normal and tumor cell nuclei. J Cell Biol 162: 809-820.

[83] Zink , D. , A.H. Fische, and J.A. Nickerson. (2004) Nuclear structure in cancer cells. Nat. Rev. Cancer. 4: 677-687.

[84] Sarkar , R., A. Guffei, B.J. Vermolen, Y. Garini, and S. Mai. (2007) Alterations of centromere positions in nuclei of immortalized and malignant mouse lymphocytes. Cytometry A. 71: 386-392.

[85] Chuang , T.C. , S. Moshir, Y. Garini, A.Y. Chuang, I.T. Young, B. Vermolen, R. van den Doel, V. Mougey, M. Perrin, M. Braun, et al. (2004) The threedimensional organization of telomeres in the nucleus of mammalian cells. BMC Biol. 2: 12.

[86] Wiech , T., S. Timme, F. Riede, S. Stein, M. Schuricke, C. Cremer, M. Werner, M. Hausmann, and A. Walch. (2005) Human archival tissues provide a valuable source for the analysis of spatial genome organization. Histochem. Cell Biol. 123: 229-238.

[87] Margaret R. Hüsler, Kristin A. Kotopoulis, John P. Sundberg, Barabara J. Tennent, Sabine V. Kunig and Barabara B. Knowles. (1998) Lactation-induced WAP-SV40 Tag Transgene Expression in C57BL/6J Mice Leads to Mammary Carcinoma. Transgenic Research 7: 253-263.

[88] Hai-Ning Zhen, Xiang Zhang, Xing-Yao Bu, Zhi-Wen Zhang, Wen-Jin Huang, Ping Zhang, Jing-Wen Liang, Xi-Ling Wang. (2000) Expression of the simian virus 40 large tumor antigen (Tag) and formation of Tag-p53 and Tag-pRb complexes in human brain tumors. Cancer 86(10):2124-2132.

[89] Fanning, E. and Knippers, R. (1992) Structure and function of simian virus 40 large tumor antigen. Annu. Rev. Biochem. 61:55-85.

[90] Monini P, Delellis L, Barbanti-Brodano G. Association of BK and JC human polyomaviruses and SV40 with human tumors. In: Barbanti-Brodano M, Bendinelli M, Friedman H, editors. DNA tumor viruses. Oncogenic mechanisms. New York, NY: Plenum Press, Inc. 1995:27-73.

[91] Carbone M, Rizzo P, Pass HI. (1997) Simian virus 40, polio vaccines and human tumors: a review of recent developments. Oncogene. 15:1877-88.

[92] Martini F, Iaccheri L, Lazzarin L, Carinci P, Corallini A, Gerosa M, et al. (1996) SV40 early region and large T antigen in human brain tumors, peripheral blood cells, and sperm fluids from healthy individuals. Cancer Res. 56:4820-4825.

[93] Knowles BB, Koncar M, Pfizenmaier K, Solter D, Aden DP, Trinchieri G. (1979) Genetic control of the cytotoxic T cell response to SV40 Tumor-associated specific antigen. The journal of Immunology. 122:1798-1806.

[94] Lelievre SA, Weaver VM, Nickerson JA, Larabell CA, Bhaumik A, Petersen OW, Bissell MJ. (1998) Tissue phenotype depends on reciprocal interactions between the extracellular matrix and the structural organization of the nucleus. Proc Natl Acad Sci USA 95:14711-14716.

[95] Tokuyasu KT. (1973) A technique for ultracryotomy of cell suspensions and tissues. J Cell Biol 57:551-565.

[96] Guillot PV, Xie SQ, Hollinshead M, Pombo A. (2004) Fixationinduced redistribution of hyperphosphorylated RNA polymerase II in the nucleus of human cells. Exp Cell Res 295:460-468.

[97] Branco MR, Xie SQ, Martin S, Pombo A. (2005) Correlative microscopy using Tokuyasu cryosections: applications for immunolabeling and in situ hybridization. In: Stephens D (ed) Cell imaging. Scion Publishing. 201-217.

[98] Pombo A. (2007) Advances in imaging the interphase nucleus using thin cryosections. Histochem Cell Biol. 128: 97-104.

[99] Jeffrey M. Levsky and Robert H. Singer. (2003) Fluorescence in situ hybridization: past, present and future. Journal of Cell Science 116 (14): 2833-2838.

[100] Schwarz-Finsterle, J., S. Stein, C. Grossmann, E. Schmitt, H. Schneider, L. Trakhtenbrot, G. Rechavi, N. Amariglio, et al. (2005) COMBO-FISH for focussed fluorescence labelling of gene domains: 3D-analysis of the genome architecture of abl and bcr in human blood cells. Cell Biol. Int. 29:1038-1046.

[101] Brown, K.E., S.S. Guest, S.T. Smale, K. Hahm, M. Merkenschlager, and A.G. Fisher. (1997) Association of transcriptionally silent genes with Ikaros complexes at centromeric heterochromatin. Cell 91:845-854.

[102] Speicher, M.R., S. Gwyn Ballard, and D.C. Ward. (1996) Karyotyping human chromosomes by combinatorial multi-fluor FISH. Nat. Genet. 12:368-375.

[103] Solovei, I., A. Cavallo, L. Schermelleh, F. Jaunin, C. Scasselati, D. Cmarko, C. Cremer, S. Fakan, and T. Cremer. (2002) Spatial preservation of nuclear chromatin architecture during three-dimensional fluorescence in situ hybridization (3D-FISH). Exp. Cell Res. 276:10-23.

[104] Emanuela V. Volpi and Joanna M. Bridger. (2008) FISH glossary: an overview of the fluorescence in situ hybridization technique. BioTechniques 45:385-409.

[105] *QIAprep*® Miniprep Handbook. (2006) Second Edition, www.qiagen.com.

[106] John C. Russ, Robert T. Dehoff. (1999) Practical Stereology (2nd ed.). Plenum Press, New York.

[107] M. R. Branco, T. Branco, F. Ramirez, and A. Pombo. (2008) Changes in chromosome organization during pha-activation of resting human lymphocytes measured by cryo-FISH. Chromosome research 16(3):413-426.

[108] J. D. Gibbons. (1985) Nonparametric Methods for Quantitative Analysis, 2nd Edition. American Sciences Press, Columbus, OH.

[109] Spring KR, Davidson MW. Introduction to Fluorescence Microscopy. Nikon MicroscopyU. http://www.microscopyu.com/articles/fluorescence/fluorescenceintro.html.

[110] The Fluorescence Microscope. Microscopes-Help Scientists Explore Hidden Worlds. The Nobel Foundation. http://nobelprize.org/educational_games/physics/microscopes/fluorescence/.

[111] http://web.uvic.ca/ail/techniques/epi-fluorescence.html

[112] Pawley JB (editor). (2006) Handbook of Biological Confocal Microscopy (3rd ed.). Berlin: Springer.

[113] A. R. Hibbs. (2004) Confocal Microscopy for Biologists, New York: Kluwer Academic.

[114] www.zeiss.de

[115] M. Born and E. Wolf. (1999) Principles of Optics. New York: Cambridge University Press.

[116] E. H. K. Stelzer. (1997) Contrast, Resolution, Pixelation, Dynamic range, and Signal-to-Noise Ratio: Fundamental Limits to Resolution in Fluorescence Light Microscopy. Journal of Microscopy. 189: 15-24.

[117] http://www.microscopyu.com/articles/formulas/formulasresolution.html

[118] K. R. Spring and S. Inoué. (1997) Video Microscopy: The Fundamentals, New York: Plenum Press.

[119] E. Abbe. (1873) Beiträge zur theorie des mikroskops und der mikroskopischen wahrnehmung, Arch. f. mikr. Anat. 8 (9): 413-468.

[120] L. Rayleigh. (1879) Investigations in optics with special reference to the

spectroscope, 1: resolving, or separating power of optical instruments. Philosophical Magazine. Reprinted in: Scientific Papers of Lord Rayleigh 1(8).

[121] AW Jones, J. Bland-Hawthorn, and PL Shopbell. (1995) Towards a General Definition for Spectroscopic Resolution. Astronomical Data Analysis Software and Systems IV 77.

[122] E. H. K. Stelzer. (2000) Practical Limits to Resolution in Fluorescence Light Microscopy, in R. Yuste, F. Lanni, A. Konnerth (eds.), Imaging Neurons: A Laboratory Manual. New York: Cold Spring Harbor Press. 12.1-12.9.

[123] J. E. N. Jonkman and E. H. K. Stelzer. (2002) Resolution and Contrast in Confocal and Two-Photon Microscopy, in A. Diaspro (ed.), Confocal and Two-Photon Microscopy: Foundations, Applications, and Advances. New York: Wiley-Liss, 101-125.

[124] S. W. Hell and E. H. K. Stelzer. (1992) Fundamental improvement of resolution with a 4pi-confocal fluorescence microscope using two-photon excitation. Opt. Commun. 93: 277-282.

[125] S. W. Hell, S. Lindek, C. Cremer, and E. H. K. Stelzer. (1994) Measurement of 4pi-confocal point spread function proves 75 nm axial resolution. Appl. Phys. Lett. 64(11): 1335-1337.

[126] T.A. Klar, S. Jakobs, M. Dyba, A. Egner, and S.W. Hell. (2000) Fluorescence microscopy with diffraction resolution barrier broken by stimulated emission. Proceedings of the National Academy of Science. 97(15): 8206-8210.

[127] Donnert, G., et al. (2006). Macromolecular-scale resolution in biological fluorescence microscopy. PNAS 103: 11440-11445.

[128] Antonio Virgilio Failla, Benno Albrecht, Udo Spöri, Andreas Schweitzer, Alexander Kroll, Georg Hildenbrand, Margund Bach, and Christoph Cremer. (2003) Nanostructure analysis using spatially modulated illumination microscopy. ComPlexUs 1:77-88.

[129] Christian Wagner, Udo Spöri, Christoph Cremer. (2005) High-precision SMI microscopy size measurements by simultaneous frequency domain reconstruction of the axial point spread function. Optik 116: 15-21.

[130] D. Baddeley, C. Batram, Y. Weiland, C. Cremer, U.J. Birk. (2007) Nano-structure analysis using Spatially Modulated Illumination microscopy. Nature Protocols 2: 2640-2646.

[131] Bailey B, Farkas D, Taylor D, Lanni F. (1993) Enhancement of axial resolution in fluorescence microscopy by standing-wave excitation. Nature 366: 44-48.

[132] Schneider B,Albrecht B, Jaeckle P,Neofotistos D, Söding S, Jäger Th, Cremer C. (2000) Nanolocalization measurements in spatially modulated illumination microscopy using two coherent illumination beams. Proc SPIE 3921: 321-330.

[133] Gustafsson MGL,Agard DA, Sedat JW. (1995) Sevenfold improvement of axial resolution in 3D widefield microscopy using two objective lenses. Proc SPIE 2412:147-156.

[134] Albrecht B, Failla AV,Heintzmann R, Cremer C. (2001) Spatially modulated illumination microscopy: Online visualization of intensity distribution and prediction of nanometer precision of axial distance measurements by computer simulations. J Biomed Opt 6:292-299.

[135] Albrecht B, Failla AV, Schweitzer A, Cremer C. (2002) Spatially modulated illumination microscopy allows axial distance resolution in the nanometer range. Appl Opt 41:80-87.

[136] H. Mathée, D. Baddeley, C. Wotzlaw, J. Fandrey, C. Cremer, U. Birk. (2006) Nanostructure of specific chromatin regions and nuclear complexes. Histochem Cell Biol 125: 75-82.

[137] D. Baddeley. (2007) Precision Measurements with SMI and 4Pi Microscopy. Ph.D. thesis, University of Heidelberg.

[138] C. Wagner. (2004) Neue Methoden zur Größen und Formbestimung von fluoreszierenden Nanostrukturen unter Verwendung der SMI-Mikroskopie. Ph.D. thesis, Universität Heidelberg.

[139] www.abcam.com

[140] Olga V. Zatsepina, Oxana O. Zharskaya, Andrei N. Prusov. (2008) Isolation of the Constitutive Heterochromatin from Mouse Liver Nuclei. In: R. Hancock (ed.) The Nucleus: Volume 1: Nuclei and Subnuclear Components. Humana Press, 169-180.

[141] Dmitriev P.V., Prusov A.N., Petrov A.V., Dontsova O.A., Zatsepina O.V., Bogdanov A.A. (2002) Mouse Chromocenters Contain Associated Telomeric DNA and Telomerase Activity. Doklady Biological Sciences, 383: 171-174(4).

[142] Soille, P. (1999) Morphological Image Analysis: Principles and Applications, Springer-Verlag, 173-174.

[143] Cremer M, von Hase J, Volm T et al. (2001) Non-random radial higher-order chromatin arrangements in nuclei of diploid human cells. Chromosome Res 9: 541-567.

[144] Parada L, McQueen P, Misteli T. (2004) Tissue-specific spatial organization of genomes. Genome Biology. 7(5): R44.

[145] R. Mayer, A. Brero, J. von Hase, T. Schroeder, T. Cremer and S. Dietzel. (2005) Common themes and cell type specific variations of higher order chromatin arrangements in the mouse. BMC Cell Biol 6: 44.

[146] The mouse data is based on the NCBI Build 37.1 (the latest) mouse assembly (April 2007, strain C57BL/6J). www.ncbi.nlm.nih.gov.

[147] Dernburg, A. F. et al. (1996) Perturbation of nuclear architecture by long-distance chromosome interactions. Cell 85, 745-759.

[148] Csink, A. K. & Henikoff, S. (1998) Large-scale chromosomal movements during interphase progression in Drosophila. J. Cell Biol. 143, 13-22.

[149] Brown KE, Guest SS, Smale ST, Hahm K, Merkenschlager M, Fisher AG. (1997) Association of transcriptionally silent genes with Ikaros complexes at centromeric heterochromatin. Cell 91, 845-854.

[150] Schübeler D, Francastel C, Cimbora DM, Reik A, Martin DI, Groudine M. (2000) Nuclear localization and histone acetylation: a pathway for chromatin opening and transcriptional activation of the human β-globin locus. Genes Dev. 14, 940-950.

[151] Iborra, F.J., and Cook, P.R. (1998) The size of sites containing SR proteins in human nuclei: problems associated with characterizing small structures by immunogold labelling. J. Histochem. Cytochem. 46: 985-992.

[152] Pombo, A., Jackson, D.A., Hollinshead, M., Wang, Z., Roeder, R.G., and Cook, P.R. (1999) Regional specialization in human nuclei: visualization of discrete sites of transcription by RNA polymerase III. EMBO J. 18: 2241-2253.

[153] Georg Hildenbrand, Alexander Rapp, Udo Spoeri, Christian Wagner, Christoph Cremer, and Michael Hausmann. (2005) Nano-sizing of specific gene domains in intact human cell nuclei by Spatially Modulated Illumination (SMI) light microscopy. Biophys. J. 88: 4312-4318.

[154] Udo J. Birk, David Baddeley, and Christoph Cremer. (2008) Nanosizing

by spatially Modulated Illumination (SMI) Microscopy and Applications to the Nucleus, Methods in Molecular Biology, 464, The Nucleus: Volume 2: Chromatin, Transcription, Envelope, Proteins, Dynamics, and Imaging, Humana Press, R. Hancock (ed.), ISBN 978-1-60327-460-9, Chapter 21 p. 389.

[155] Sonya Martin, Antonio Virgilio Failla, Udo Spoeri, Christoph Cremer and Ana Pombo. (2004) Measuring the Size of Biological Nanostructures with Spatially Modulated Illumination Microscopy. Mol. Biol. Cell, 15: 2449-2455.

[156] Jürgen Reymann, David Baddeley, Manuel Gunkel, Paul Lemmer, Werner Stadter, Thibaud Jegou, Karsten Rippe, Christoph Cremer and Udo Birk. (2008) High-precision structural analysis of subnuclear complexes in fixed and live cells via spatially modulated illumination (SMI) microscopy. Chromosome Research, 16: 367-382.

[157] Alberts, B. et al. (1998) Essential Cell Biology: An Introduction to the Molecular Biology of the Cell. Garland, New York.

[158] Felsenfeld, G. & Groudine, M. (2003) Controlling the double helix. Nature 421: 448-453.

[159] Kratky, O. & Porod, G. (1949) Rontgenuntersuchung geloster Fadenmolekule. Rec. Trav. Chim. 68: 1105.

[160] David J. Tremethick. (2007) Higher-order structures of chromatin: the elusive 30 nm fiber. Cell 128: 651-654.

[161] Wolffe, A. P. (1995) Chromatin: Structure and Function, 2nd edition. Academic Press, New York.

[162] D. Baddeley, Y. Weiland, C. Batram, U. Birk and C. Cremer. (2009) Model based precision structural measurements on barely resolved objects. Journal of Microscopy. doi: 10.1111/j.1365-2818.2009.03304.x.

[163] A. V. Failla, U. Spöri, B. Albrecht, A. Kroll, C. Cremer. (2002b) Nanosizing of fluorescent objects by spatially modulated illumination microscopy. Appl. Optics 41(34): 7275-7283

[164] Mongelard, F., Vourc'h, C., Robert-Nicoud, M., Usson, Y. (1999) Quantitative assessment of the alteration of chromatin during the course of FISH procedures. Fluorescent in situ hybridization. Cytometry 36 (2), 96-101.

[165] Hotelmans, R.W., Prins, F.A., Corneless-ten Velde, I., van der Meer, J., van de Velde, C.J., van Dierendonck, J.H. (2001) Effects of acetone, methanol, or paraformaldehyde on cellular structure, visualized by reflection contrast microscopy and transmission and scanning electron microscopy. Appl. Immunohistochem. Mol. Morphol. 9 (4), 346-351.

[166] Kozubek, S., Lukásová, E., Amrichová, J., Kozubek, M., Lisková, A., Slotová, J. (2000) Influence of cell fixation on chromatin topography. Anal. Biochem. 282 (1): 29-38.

[167] P. Lemmer, M. Gunkel, D. Baddeley, R. Kaufmann, A. Urich, Y. Weiland, J. Reymann, P. Müller, M. Hausmann, C. Cremer. (2008) SPDM: light microscopy with single-molecule resolution at the nanoscale. Appl Phys B DOI 10.1007/s00340-008-3152-x.